2021-12-16

Photonic quantum technologies: non-destructive photon detection and quantum simulation in solid-state systems

Goswami, Sumit

UNIVERSITY OF CALGARY

Photonic quantum technologies: non-destructive photon detection and quantum simulation in solid-state systems

by

Sumit Goswami

A THESIS
SUBMITTED TO THE FACULTY OF GRADUATE STUDIES
IN PARTIAL FULFILLMENT OF THE REQUIREMENTS FOR THE
DEGREE OF DOCTOR OF PHILOSOPHY

GRADUATE PROGRAM IN PHYSICS AND ASTRONOMY

CALGARY, ALBERTA
DECEMBER, 2021

Abstract

Quantum technologies are progressing rapidly with the potential for a wide range of applications. Many different physical systems are being investigated to build quantum technologies. Photonics plays a crucial part here. Quantum networks will almost certainly rely on photons due to their high speed and very small interaction with the environment. Photonic quantum computing technology is very promising too and making long strides recently. Moreover, light-matter interaction is an essential part of most systems. Due to their ultrasmall dimensions, many quantum systems are manipulated using light. Among these solid-state systems are particularly interesting due to their potential for robust practical uses in the long term.

In this thesis, we propose two solid-state quantum devices employing photonic technologies in two very different areas - non-destructive photon number detection and quantum simulation. Non-destructive photon number detection finds application in both quantum networks and computing. Building on previous works to make non-destructive detectors using cross-phase modulation, we aimed for single-photon non-destructive detection using a nano-photonic cavity doped with rare-earth ions. The cavity however introduced complex phase shapes. Despite this challenge, a non-destructive detection scheme with high success probability and low loss was successfully proposed. The quantum many-body simulation proposal used recently discovered Rydberg excitons in semiconductors. Shining focused laser lights on a microscopic crystal, exciton patterns in any arbitrary shape can be created. The Rydberg interactions between these excitons would give rise to ordered phases and can have interesting applications like solving the maximum independent set problem. A very high fidelity exciton detection scheme was explored too.

List of papers

- Guo, Yu, and Sumit Goswami. " Discordlike correlation of bipartite coherence." Physical Review A 95, no. 6 (2017): 062340.

- Goswami, Sumit, Khabat Heshami, and Christoph Simon. " Theory of cavity-enhanced nondestructive detection of photonic qubits in a solid-state atomic ensemble." Physical Review A 98, no. 4 (2018): 043842.

- Taylor, Jacob, Sumit Goswami, Valentin Walther, Michael Spanner, Christoph Simon, and Khabat Heshami. " Simulation of many-body dynamics using Rydberg excitons." arXiv preprint arXiv:2107.02273 (2021) - Submitted for publication in Quantum Science and Technology. (The first two authors has contributed equally to this work)

Acknowledgements

I am deeply grateful to everyone who helped me in my dream of pursuing research in physics. I want to start by expressing my gratitude to all those who made this thesis a reality. First of all, I am grateful beyond words for the constant support, direction and encouragement that I received from my supervisor Dr. Christoph Simon. His simple explanations of complex topics, attention to every detail and active cooperation at every step of the PhD is something I cherished all through.

I would like to recognise the contribution of my close collaborator Dr. Khabat Heshami who worked with me closely on different projects and always provided valuable advice. I want to thank my other collaborators Jacob Taylor, Valentin Walther and Michael Spanner. It was a pleasure to work with all of you.

I would like to acknowledge financial support from a Dean's International Doctoral Recruitment Scholarship of the University of Calgary, an Alberta Innovates Technology Futures (AITF) Graduate Student Scholarship (GSS), an Izaak Walton Killam Doctoral Scholarship and an Eyes High International Doctoral Scholarship along with the regular University of Calgary PhD student funding.

I express my heartfelt thanks to all my teachers from school to university. They not only taught me but also generated my own inquisitiveness to learn. I would not have reached here without their teaching and guidance. Moreover, I would like to thank all my friends who spent countless hours with me discussing science and who stayed by my side in rain or shine.

Finally, this thesis would never be possible without the constant support and inspiration of my whole family, especially my grandfather Shri Narendra Kumar Mukherjee and my mother Smt. Lina Goswami. I would not be able to come this far without you lifting me up all through my life.

To my grandfather and my mother

Table of Contents

List of Figures and Illustrations

List of Tables

Abbreviation

Abbreviation:	Definition:
Qubit	Quantum bit
QND	Quantum nondemolition
AFC	Atomic frequency comb
EIT	Electromagnetically induced transparency
BS	Beam splitter
BSM	Bell state measurement
DLCZ	Duan, Lukin, Cirac and Zoller protocol
PPKTP	Periodically Poled Potassium Titanyl Phosphate
SPDC	Spontaneous Parametric Down-Conversion
WCP	Weak coherent pulse
QKD	Quantum key distribution
BB84	Charles Bennett and Gilles Brassards' 1984 QKD protocol
LEO	Low earth orbit
GEO	Geostationary earth orbit
APT	Acquiring pointing and tracking
QM	Quantum memories
REI	Rare-earth ions
DFT	Discrete Fourier transform
BCS	Bardeen-Cooper-Schrieffer

BEC	Bose-Einstein condensate
MIS	Maximum independent set

Chapter 1

Introduction

Photonic technologies have become ubiquitous in quantum information processing. Photonics has become important in both quantum networks and quantum computing. Photonics is essential in quantum networks as all quantum network architectures proposed and implemented to date - be it through optical fibres, free space communication or satellite transmission - used optical transmission [1]. Photons have the advantages of very high speed and low interaction with their environment. However, low interaction is a challenge too as it is very difficult to make two photons interact. There has been rapid progress in photonic quantum computing too. Several approaches were proposed and attempts were made to build a photonic quantum computer [2, 3, 4, 5, 6]. Recently, one of the most advanced quantum computers to date employing more than hundred qubits was built using photonics technology [7]. Several efforts are currently underway to build large quantum simulators and analogue quantum computers where optical technologies play an integral part [8, 9].

Solid state quantum technologies are essential to quantum information processing too. Solid state systems are very attractive due to their long-term potential for robust and practical usage, as well as potentially easier mass-manufacturing based on nanofabrication techniques. However, the thermal vibrations in solid state systems, called phonons, generally causes issues like dephasing. To counter this challenge, solid state systems need to be cooled

to cryogenic temperatures. Even with this challenge many useful quantum devices have already been built from solid-state systems. In context of quantum networks, solid state nitrogen-vacancy centre qubits have been used to create several initial prototypes of quantum networks [10, 11]. Ensemble based solid state single photon level quantum memory was implemented using the atomic frequency comb (AFC) proposal in rare-earth ion doped crystal [12]. Superconducting Josephson-junction qubits are one of the leading contenders to build a large-scale quantum computer [13, 14, 15].

In this thesis, we proposed two different schemes which make use of both the above two promising technologies - photonic and solid-state systems. The two proposals are concerning non-destructive photon detection [16] and designing a quantum simulator [17]. Non-destructive photon detection - also called quantum non demolition (QND) detection - proposal is based on sending a single photon signal and another intense probe pulse inside a nanophotonic cavity containing rare-earth ions embedded in a solid-state crystal. The quantum simulator proposal uses focused laser pulses, which are shined at specific spots on a semiconductor crystal to create excitons. The behaviour of these excitons is measured using laser pulses and single photon detectors. In both these proposals, photonics and solid-state technologies are intricately intertwined.

The thesis is structured as follows. This thesis is based on the two above mentioned papers. After Introduction in chapter 1, the next two chapters provide background information for the first paper concerning non-destructive detection or QND detection. Chapter 2 introduces QND detection and chapter 3 provides a review of quantum networks where one of the principal applications of QND detectors lies. Chapter 4 is the non-destructive detection paper. Chapter 5 and 6 provide introductory material for the second paper regarding quantum simulation. Chapter 5 introduces Rydberg excitons in semiconductors on which the quantum simulator proposal is based. Chapter 6 gives a brief overview of quantum simulation. Chapter 7 includes the quantum simulation paper. Chapter 8 concludes the thesis with Conclusion and Outlook.

Chapter 2

Quantum nondemolition measurement

Quantum nondemolition (QND) measurement (or non-destructive detection) was discovered when quantum measurement theory for a single quantum system was explored. In the early days of quantum mechanics, quantum systems were measured only as ensembles. The capability to measure single quantum systems were not there until the development of lasers and quantum electronics around 1960s. In an ensemble, any quantity can be measured with high resolution, owing to repeated measurements. Hence, the theory of quantum measurements developed only later as the technology arrived for measurement of single quantum systems, although there were some initial interests and studies before too.

2.1 Theory

2.1.1 QND Observable

As quantum measurement theory was getting developed, the main challenge was understood to be the measurement back action due to uncertainty principle [18, 19, 20]. We will illustrate this with an example. If one wants to monitor the position of a free mass by successive measurements that wouldn't be possible due to the uncertainty principle. As one measures the position x of a free particle with small uncertainty, a large uncertainty was introduced

in the conjugate variable momentum p, due to the uncertainty principle (i.e. $\Delta x \Delta p \geq \hbar/2$). As position depends on momentum, the uncertainty in momentum then feeds back into position. This is called the measurement back-action. So, if x is measured sometime later the uncertainty in measurement of x would increase. However, the situation is not the same if one measures the momentum p of a free particle. x does get contaminated (with large uncertainty) but the value of momentum p of a free particle (Hamiltonian $H = \frac{p^2}{2m}$) doesn't depend on the value of x. Instead p is an integral of motion which remains constant over time. Hence, measurement of p is called a back-action evasion measurement. Momentum, p, can be monitored over time by measuring it again and again. If there is an external perturbation to p between two measurements, it can be detected. Hence, momentum (p) is called an QND observable for a free particle.

The general criterion for any observable $A(t)$ to be a QND observable is,

$$[A(t), A(t')] = 0 \tag{2.1}$$

as the system is evolving freely in the Heisenberg picture [18]. The commutator among them being zero, the set of eigenvectors are the same for $A(t)$ and $A(t')$. The wavefunction $|\psi\rangle$ does not change in Heisenberg picture. So, if QND measurements are carried out repeatedly the wavefunction collapses only the first time. After the collapse the state is an eigenstate of the QND observable, say $A(t)$. Hence, in the next QND measurement there is no collapse of the wavefunction, because by the QND observable condition the state before measurement - i.e. the eigenstate of $A(t)$ - is already an eigenstate of $A(t')$. Quantum mechanics is deterministic without the collapse of wavefunction. Hence, after the first measurement future QND measurement results are deterministically determined. Here it needs to be noted that although $A(t)$ and $A(t')$ have the same set of eigenvectors, the eigenvalues corresponding to those eigenvectors can very well change. Hence, successive QND measurements can very well produce different results although they don't collapse the wavefunction.

The above description is in Heisenberg picture where operators (or observables) evolve in time while wavefunction remains stationary. In Schrödinger picture, the operators are stationary and wavefunction evolves. Hence, to find the condition for a observable being a QND observable in Schrödinger picture one has to track the evolution of the wavefunction (more specifically eigenstates of the observable) instead. The condition, in its physical interpretation, would be identical to that of Eq. 2.1, as it is expected.

QND can be of two kinds - continuous and stroboscopic. In continuous QND, Eq. 2.1 is satisfied for all times (t, t'). In the stroboscopic case Eq. 2.1 is only satisfied at particular time (t, t') values. So, for a continuous QND observable the measurement can be done over long time however for stroboscopic QND observable it has to be done quickly.

In the case of a free particle momentum is conserved and is a continuous QND observable. This is shown in Fig. 2.1 (a). The particle was initially in a wave function with the broad spread in momentum (in I). A QND measurement of the momentum was carried out (in II) and the wave function collapsed. However, as momentum is a continuous QND observable for a free particle, eigenstates of momentum did not change under free evolution (in III) or in another QND measurement (in IV).

On the other hand, the momentum of a harmonic oscillator is a stroboscopic QND observable. (see Fig. 2.1 (b)). For a harmonic oscillator, position and momentum are given by

$$x(t) = x(0)cos(\omega t) + \frac{p(0)}{m\omega}sin(\omega t), \tag{2.2}$$

$$p(t) = p(0)cos(\omega t) - m\omega x(0)sin(\omega t). \tag{2.3}$$

Using these relations one can deduce,

$$[x(t), x(t+\tau)] = \frac{i\hbar}{m\omega}sin(\omega\tau), \tag{2.4}$$

$$[p(t), p(t+\tau)] = i\hbar m\omega sin(\omega\tau), \tag{2.5}$$

which is trivial to see for the case $t = 0$. Clearly, these commutators (Eq. 2.4 and Eq. 2.5) are not zero at all times. They become zero at intervals of $\frac{n\pi}{\omega}$. Hence, one can carry out a QND measurement of momentum $p(t)$ of the oscillator at $t = 0$ with high precision (as shown in I and II). Momentum, $p(t)$ then becomes highly uncertain (in II) again under free evolution before coming to the previous precise state again (in IV) when another QND measurement of the momentum would give exactly the expected result. This enables monitoring of $p(t)$ periodically.

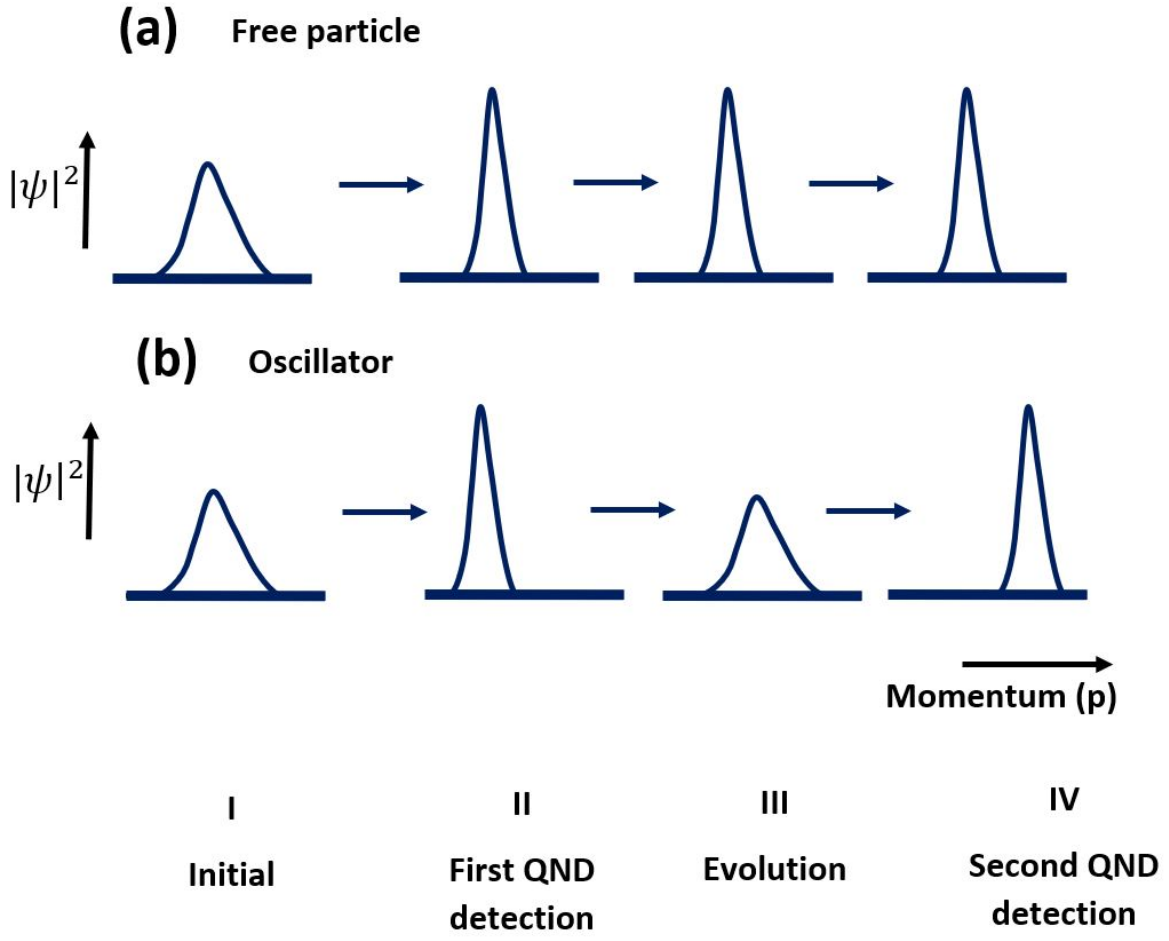

Figure 2.1: Continuous and stroboscopic QND observables - Momentum of a free particle and an oscillator at different times (I to IV) are shown when two successive QND measurements were carried out. (A) Momentum of a free particle is an integral of motion. Hence it is a QND observable at all times, that is a continuous QND observable. (B) However, momentum of an oscillator becomes QND observable only at specific times like in II and IV here. Hence, it is a stroboscopic QND observable.

Even for continuous QND measurements it does not mean that $A(t)$ is constant in time, i.e. an integral of motion. This is because the eigenvalues corresponding to those eigenvectors can change, as discussed above. In the previous example, momentum of a free mass is an integral of motion and so too would be the energy of the mass. However, this not always true.

2.1.2 Theory of QND measurements

QND measurement is not guaranteed by finding of a QND observable only. To measure the observable a measuring system or meters needs to interact with the system. If not done correctly, this can introduce perturbation to the QND observable too [19].

In quantum measurement, collapse of the wavefunction happens due to interaction with a classical measurement apparatus. To perform a QND measurement one must not make the system interact directly with the classical measurement apparatus as that generally means the system is permanently demolished, e.g. when a photon is detected in photodetector. Hence, QND measurements must be indirect. In an indirect measurement a quantum measuring system (represented as meter hereafter) needs to work like an ancilla. The meter is meant to interact with the system and get entangled. Later when the meter is measured by the classical measuring apparatus the meter-system entangled state collapses which results in the measurement of the system.

Below we consider the conditions on the meter and the interactions, as well as the system, for a complete QND measurement. The necessary and sufficient conditions for a QND measurement are given by Braginsky et. al. [19] as,

$$[q, U]|\psi\rangle = 0 \tag{2.6}$$

Here, q is the system observable to be measured, U the operator for complete evolution of system and meter combined (including system-meter interaction) and $|\psi\rangle$ is the initial state

of the quantum meter. The above condition is generally replaced by the simpler sufficient (not necessary) condition of

$$[q, U] = 0 \tag{2.7}$$

This is quite a general condition for QND measurements containing both continuous and stroboscopic QND observables. This can be understood as follows. If one considers an eigenvector of q as $|q_i\rangle$ with eigenvalues q_i (i.e., $q|q_i\rangle = q_i|q_i\rangle$), and an arbitrary state of the meter as $|\psi_m\rangle$ then

$$[q, U]|q_i\rangle \otimes |\psi_m\rangle = 0, \tag{2.8}$$

implying

$$q(U|q_i\rangle \otimes |\psi_m\rangle) = q_i(U|q_i\rangle \otimes |\psi_m\rangle). \tag{2.9}$$

Hence, $U|q_i\rangle \otimes |\psi_m\rangle$ is an eigenvector of q. Again, $U|q_i\rangle \otimes |\psi_m\rangle$ is the evolved joint state of the system and meter when the initial state was $|q\rangle \otimes |\psi_m\rangle$. So, this again confirms the interpretation of QND measurement as a measurement where the eigenstate of the measurement operator (on the system, i.e. q here) remains an eigenstate under time evolution.

However, analyzing the joint evolution of the system and meter (i.e. U) makes Eq. 2.7 a complicated criterion to evaluate. A much simpler sufficient condition (but not necessary) arises when q is an integral of motion of the coupled system and meter,

$$i\hbar\frac{\partial q}{\partial t} + [q, H] = 0 \tag{2.10}$$

where H is the total Hamiltonian of the system and meter together.

A further simplification arises if we consider the QND observable q to be an integral of motion of the objects under study itself. We saw above that this is not necessary even for q to be just the QND observable of the system, as in the case of stroboscopic QND observables.

However in many instances q is actually an integral of motion of the system. In that case,

$$i\hbar\frac{\partial q}{\partial t} + [q, H_0] = 0 \tag{2.11}$$

Considering the total Hamiltonian as $H = H_0 + H_M + H_I$ where H_M is the meter Hamiltonian and H_I is the interaction Hamiltonian. Coupled with Eq. 2.10. and the fact [q,H_m] = 0 (as the object and meter are different systems) we find,

$$[q, H_I] = 0 \tag{2.12}$$

This condition for QND measurement is rather easy to verify and used in most practical situations.

2.1.3 History of QND measurements

QND measurements have early roots, almost going as far back as the founders of quantum mechanics itself. In the early 1930s, the essential idea of a possible arbitrary high-resolution measurement of an observable was toyed with first by Landau [21] and then von Neumann [22]. They understood that the velocity of a free particle can be such an observable. Von Neumann even gave a proposal for measuring velocity of a free mass by the Doppler Effect. However, for a more detailed analysis of QND measurement we had to wait for two more decades when David Bohm deduced the relation $[q, H_I] = 0$ [23]. This was an excessive requirement though - i.e., a sufficient condition, but not a necessary one - as discussed earlier.

Later with the technological developments in single particle measurement, the interest in quantum measurements grew and many developments happened in quantum measurement theory [24, 25] . The comprehensive development of QND measurement theory happened in 1970s by Braginsky, Vorontsov, Khalili, Unruh, Thorne and others [26, 27, 28]. Braginsky et. al. showed that the energy of an electromagnetic resonator (i.e. photons in an optical

cavity) can be measured non-destructively by measuring the ponderomotive force on the resonator walls [20]. Later, Thorne et. al. showed a QND measurement scheme for the quadrature of an oscillator [28]. Invention of QND measurement got its principal impetus from the search for gravitational waves [18, 20]. It was conceived that a large hanging mass would be affected by a passing gravitational wave and if one can measure some observables related to the mass's motion with very high precision the effect of gravitational waves can be detected [18]. QND measurements using squeezed states of light to achieve higher precision is still relevant in gravitational wave detection using lasers in LIGO [29].

Although QND measurement theory started in context of gravitational waves, it is of much more general nature as we have seen above. Hence, soon after their discovery QND measurements found application in many areas of science [20]. QND detection has especially attracted attention in the field of quantum optics [30] and many applications have been found including photon number QND measurements, which is described next.

2.2 Photon number QND measurement

A photon number quantum non demolition measurement scheme was proposed in 1985 using the optical Kerr effect [31]. The Kerr effect was first discovered in 1885 by John Kerr. It is a nonlinear optics effect where the refractive index of a medium changes depending on the intensity of the light propagating through it. The refractive index of the medium undergoing Kerr effect is given by $n = n_0 + n_2 I$, where n_0 is the original refractive index, n is the new refractive index and I is the intensity of the light propagating through the medium. However, Kerr non-linearity (i.e. value of n_2) is generally very small in most materials. Hence, it was only studied extensively using lasers (which have high electric field intensity) after the laser was discovered in the 1960s.

2.2.1 Photon number QND measurement proposal

The proposed QND measurement scheme of 1985 [31] is shown in Fig. 2.2. A signal pulse passes through a non-linear medium altering its refractive index which gives a probe pulse passing through the same medium a phase shift. The signal and probe pulses are at different frequencies ω_p and ω_s. They both can be made to pass through the same nonlinear medium by using dichroic mirrors $M1$ and $M2$ which are completely reflective for the probe while being completely transmissible for the signal. The refractive index of the nonlinear medium is changed based on the intensity of the signal pulse by the optical Kerr effect. The refractive index of a medium is dependent on the frequency of the incident light and so is the change in the refractive index (or permittivity). Hence, the Kerr effect of a medium is different at different frequencies of light. As the probe is at a very different frequency compared to the signal it can be made to have a negligible Kerr effect on the medium. The phase of the probe pulse is altered due to the signal pulse intensity. This phase can be measured by the interferometer by making the probe pulse interfere with itself using a homodyne detection setup. One really measures the sine component of the phase shift which is identical to the phase shift for small phase shifts.

The energy of the probe wave is given by,

$$H_p = \int_V \frac{1}{2}\epsilon E_p^2 dV \tag{2.13}$$

where the permittivity ϵ can be written as $\epsilon = \epsilon_1 + \Delta\epsilon$ where $\Delta\epsilon = \chi^{(3)} E_s^2$ is due to the refractive index change caused by the signal pulse. This results in an interaction Hamiltonian,

$$H_I = \int_V \frac{1}{2}\chi^{(3)} E_s^2 E_p^2 dV \tag{2.14}$$

Quantizing the electric fields in Eq. 2.13 and Eq. 2.14 gives rise to the following quantities

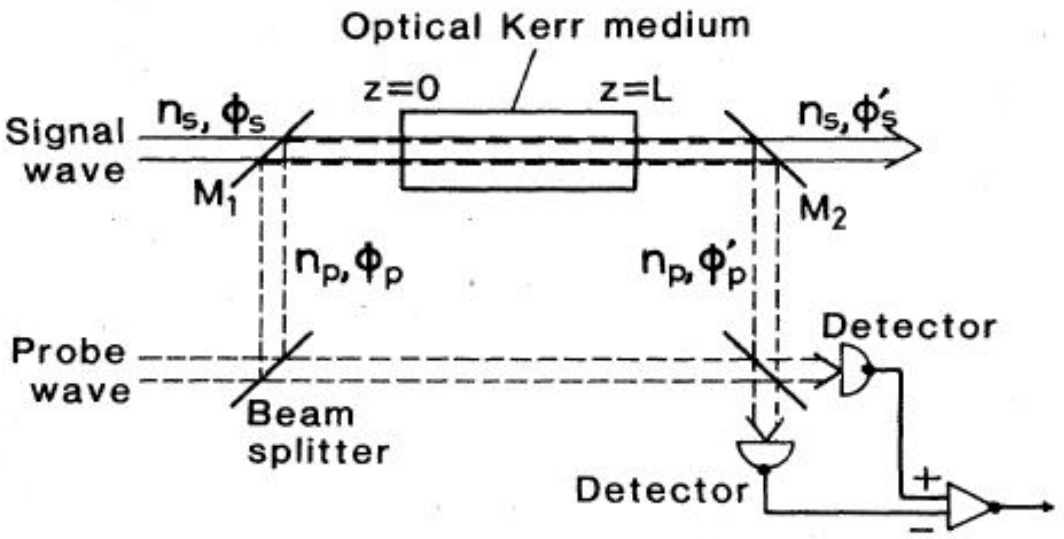

Figure 2.2: Photon number QND measurement proposal using cross phase modulation. Phase of the probe wave is altered as the refractive index of the optical Kerr medium is changed due to signal wave intensity. The change in phase of the probe wave is measured by the interferometer to ascertain the photon number in the signal wave. Reprinted with permission from [31].

important for QND measurements,

$$H_s = \hbar\omega_s(a_s^\dagger a_s + 1/2) \tag{2.15}$$

$$H_p = \hbar\omega_p(a_p^\dagger a_p + 1/2) \tag{2.16}$$

$$H_I = \frac{\hbar^2}{2V\epsilon^2}\omega_p\omega_s\chi^{(3)}a_p^\dagger a_p a_s^\dagger a_s \tag{2.17}$$

$$A_s = n_s = a_s^\dagger a_s \tag{2.18}$$

$$A_p = \frac{1}{2i}\left(\frac{1}{\sqrt{n_p+1}}a_p - a_p^\dagger\frac{1}{\sqrt{n_p+1}}\right) \tag{2.19}$$

These equations contain the creation and any annihilation operators as $a^\dagger$ and a, the number operator as $n = a^\dagger a$ and the volume for mode quantization as V.

H_I contains $A_s = a_s^\dagger a_s$ and hence $[H_I, A_s] = 0$ making A_s a continuous QND observable. The resultant phase shift depends on the spatial and temporal overlap between signal and probe waves. In [31], the signal wave is assumed to be present all the time while the probe pulse is present. However, the complete signal may not be sensed by the probe pulse using this method. Hence, in many of the experimental demonstration of a weak signal pulse providing a large detectable effect on a probe pulse, quantum memories are involved where either the signal or the probe pulse is stored. The interaction between signal and probe then happens by light-matter interaction with the non-stored pulse interacting with the quantum memory.

2.2.2 Experiments

In one such experiment by Chen et. al., a signal pulse at the level of a single photon is used to create an all-optical switch for a large probe pulse [32]. The signal is stored in an ultracold atomic ensemble inside a cavity using a control pulse as shown in the Fig. 2.3. The light storage is carried out by using the electromagnetically induced transparency (EIT) mechanism. There are several atomic states involved. The signal and control beams are incident transverse to the cavity and hence they don't need to be in resonance to the cavity mode, which is resonant with the $|s\rangle$ to $|e\rangle$ transition. The atoms are initially in $|g\rangle$ state and the signal is stored by transferring an excitation to $|s\rangle$ state using the control light field through the intermediate state $|d\rangle$. Once the signal is stored it is detuned from the resonance frequency of the optical cavity which makes the probe pulse reflect from the cavity instead of being transmitted. This created a single photon level signal mediated switch. In absence of the stored signal, the large probe pulse is transmitted through the cavity while in presence of the signal it is reflected.

The transmission of the probe pulse with different photon numbers are shown in Fig. 2.4. As the photon number in signal pulse is increased (0, 0.4, 1.4 and 2.9 respectively from top to bottom) the intensity of the transmitted probe pulse through the cavity decreases rapidly

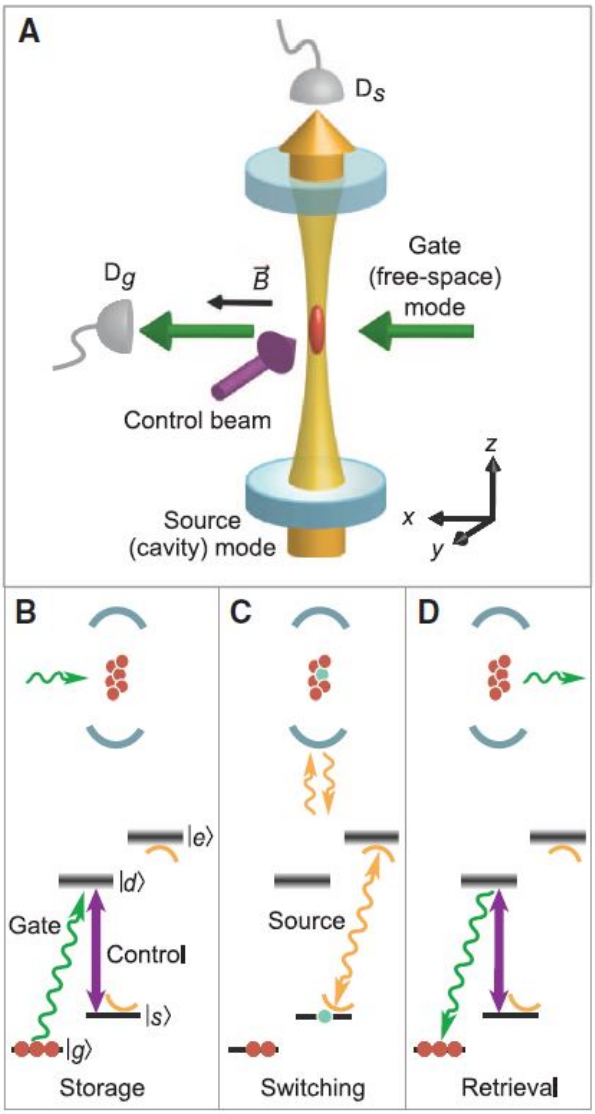

Figure 2.3: All optical switch by storing a single-photon level signal in an atomic ensemble. (A) Experimental setup - the signal (or gate, in green) and control (in purple) pulses are incident transverse to the cavity while the probe (or source, in yellow) pulse is incident along the cavity mode. The atomic ensemble (in red) is cooled and trapped inside the cavity. (B) Initially the gate mode is stored in the atomic ensemble using stopped light techniques with the control field. (C) The presence of the stored gate mode detunes the cavity mode and hence the source mode gets reflected - creating an all optical switch. (D) The signal or gate mode can be retrieved using the control field later. Reprinted with permission from [32].

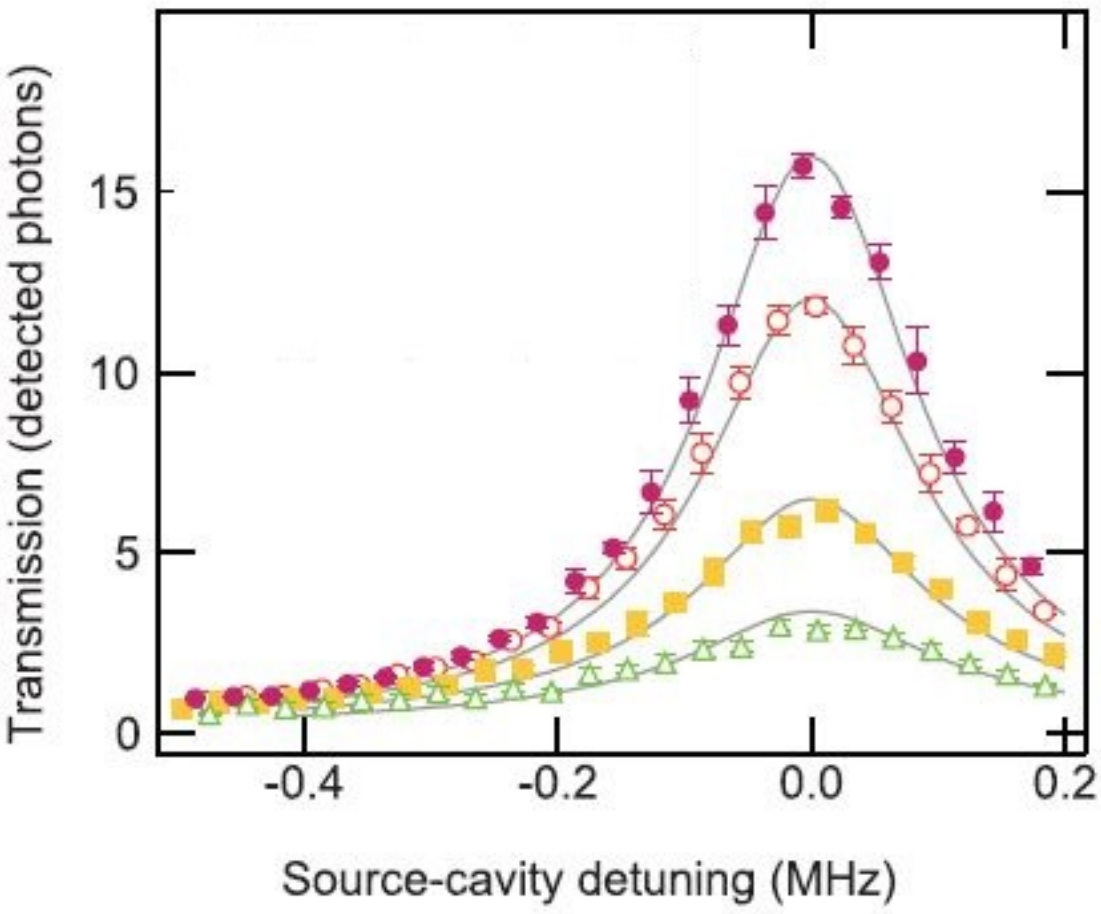

Figure 2.4: Transmission of the probe (or source) pulse is plotted for different signal (or gate) pulse photon numbers - 0, 0.4, 1.4 and 2.9. For larger stored signal photon numbers, the probe mode transmission successively decreases as probe gets reflected instead of being transmitted. Reprinted with permission from [32].

showing that the probe pulse has become detuned from the cavity resonance.

A photon number QND measurement would not measure the photonic qubit state. If the photonic qubit is encoded as polarization, time bin or frequency qubit, it doesn't necessarily need to be measured while measuring photon number as those variables are in a completely different degree of freedom. However, the experiment must be carefully designed for that. For example, in [31] a time-bin photonic qubit will not remain undisturbed as the phase of the probe pulse depends on the spatiotemporal overlap between the signal and probe pulse. In [33] an experiment was designed which can perform a photon number QND measurement of the signal while keeping its time bin qubit state intact. This was done by storing the large probe pulse in an ensemble of rare-earth ion doped crystal after which the signal passes over the ensemble and imparts a phase shift on the stored probe pulse through AC stark effect. The probe pulse was later retrieved from the memory and its phase was measured by interfering it with a local oscillator derived from the same laser like that of Fig. 2.2. The phase imparted on the probe pulse only depends on the signal photon number and not what time bin qubit state the signal existed in. Hence, the time bin qubit remains intact.

2.2.3 AC Stark effect

The AC stark-effect (also called Autler-Townes effect and dynamic stark effect) through which the signal pulse interacts with the quantum memory in [33] is discussed below. For a two-level atom, the AC stark effect is straight forward mathematically. It can be understood perfectly well by just considering a semi- classical calculation - i.e., considering a classical light wave interacting with atoms. The Hamiltonian has two parts - H_0, the intrinsic Hamiltonian for the atom and H_I, the atom-photon interaction Hamiltonian.

$$H = H_0 + H_I = \hbar\omega_a|e\rangle\langle e| + \frac{\hbar\Omega}{2}\left(|e\rangle\langle g|e^{i\omega_p t} + |g\rangle\langle e|e^{-i\omega_p t}\right) \tag{2.20}$$

where ω_a and ω_p are the atomic transition and light frequencies respectively. Ω denotes

the Rabi frequency, while $|e\rangle, |g\rangle$ represent atomic excited and ground States. In the rotating frame approximation H reduces to,

$$H_r = \hbar\Delta|e\rangle\langle e| + \frac{\hbar\Omega}{2}\Big(|e\rangle\langle g| + |g\rangle\langle e|\Big) = \frac{\hbar}{2}\begin{pmatrix} 0 & \Omega \\ \Omega & 2\Delta \end{pmatrix} \tag{2.21}$$

where, $\Delta = \omega_a$–ω_p

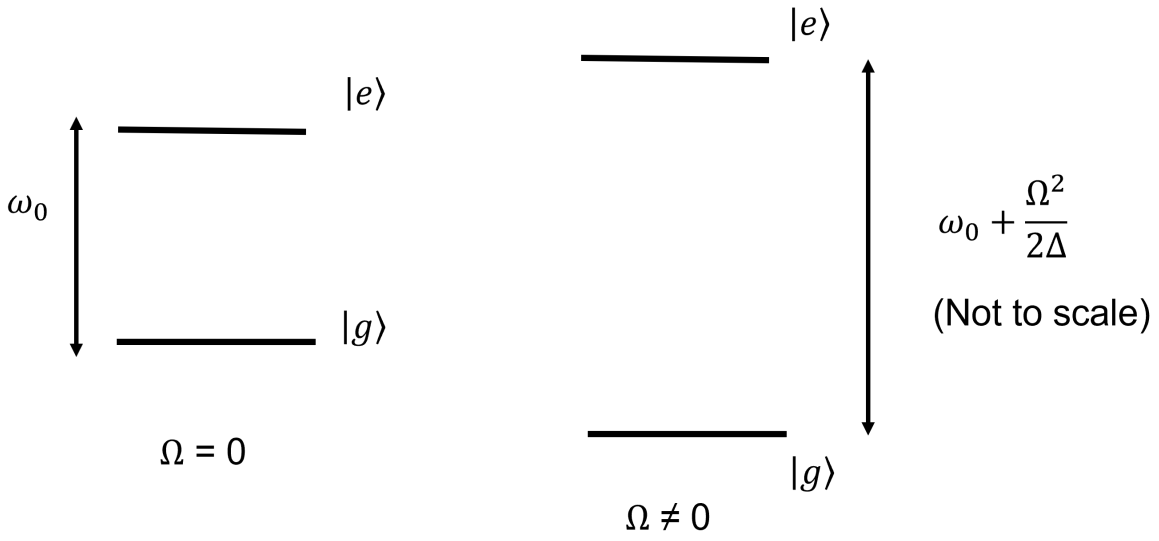

Figure 2.5: AC stark effect - change in energy separation between atomic ground ($|g\rangle$) and excited ($|e\rangle$) states due to the AC stark effect. In absence of any light (and so AC stark effect) the separation is the natural frequency of the atom ω_0. However, AC stark effect changes the separation by $\frac{\omega^2}{2\Delta}$ which will give an extra detectable phase of $\frac{\omega^2 T}{2\Delta}$ in time T.

On diagonalization the energy eigenvalues of H_r can be found to be -

$$E_\pm = \frac{\hbar\Delta}{2} \pm \hbar\frac{\sqrt{\Omega^2 + \Delta^2}}{2} \tag{2.22}$$

In the limit of $\Delta >> \Omega$, the right hand term $\hbar\frac{\sqrt{\Omega^2+\Delta^2}}{2} = \frac{\hbar\Delta}{2}\Big(1 + \frac{\Omega^2}{\Delta^2}\Big)^{1/2} \approx \frac{\hbar\Delta}{2} + \frac{\hbar\Omega^2}{4\Delta}$ Using this, we find

$$E_\pm = \hbar\Delta + \frac{\hbar\Omega^2}{4\Delta}, -\frac{\hbar\Omega^2}{4\Delta} \tag{2.23}$$

The shift of the energy levels from the bare atom levels are shown in Fig. 2.5. This shows that the energy levels are separated by an extra amount of $\frac{\Omega^2}{2\Delta}$. If the light pulse is of duration T the extra phase acquired by the atom is $\frac{\Omega^2}{2\Delta}T$. This extra phase can be detected which is exactly what is done in [33] where the stored probe pulse was retrieved and the extra phase was measured.

2.2.4 Application

QND detection can be applied in many different areas of quantum optics [30]. QND measurement has application in various other areas including quantum information processing [34, 35, 36]. One significant application of photon number QND detection would be in constructing a satellite-based downlink global quantum network architecture [37]. It would be crucial to know if the photonic qubit has arrived at the ground station (surviving atmospheric and diffraction loss) from the satellite, without measuring its qubit state. This is discussed in the next chapter where quantum network is described in detail. QND measurement can be used in fibre-based quantum repeater schemes too. The diverse application of the QND measurement were described in our QND measurement paper [16] too, which describes a cavity enhanced photon number QND measurement scheme using a rare-earth ion ensemble.

QND measurement in itself can be valuable to photonic quantum computation [38]. Moreover, photon number QND measurement is an indirect measurement scheme which essentially entangles the system with an ancilla. This entangling operation can be tweaked to give rise to a two-qubit gate for linear optics quantum computation [39]

Chapter 3

Quantum Networks

3.1 Introduction

Quantum networks are emerging as a key future communication technology alongside opening doors to possibly new levels of fundamental physics research [1]. A global quantum network enabling quantum communication between any two points on Earth would transform many technologies, many of them possibly yet unexplored. Foremost among these technologies are quantum cryptography, distributed quantum computing and entanglement-based quantum sensing [40, 41, 42, 43, 44]. Quantum cryptography is a secure communication technology where the security of the cryptographic protocol is guaranteed by the laws of nature itself. It is the most near-term application of quantum communication in which significant progress has already been achieved [40]. Creating a quantum internet, running distributed quantum computing, is the long-term goal of quantum networks. In distributed quantum computing multiple far-away quantum computers will be connected to achieve computation in a much larger Hilbert space [41]. In the short term though myriad of other applications should present themselves in a budding quantum network. Many entanglement-based sensing protocols are examples of such proposals. Using entanglement distributed in a quantum network, atomic clocks can be a better global timekeeper boosting the precision of our nav-

igation technologies [44]. Similarly, entanglement distribution can improve the precision of large baseline telescope [43]. Fundamental physics research is another exciting area that will open with a growing quantum network. Along with fundamental test of quantum mechanics like Bell inequality violation at large distances [45, 10], quantum networks may shed some light on theories of quantum gravity [46] and other unexplored areas because quantum effects at such large distances would be explored for the first time.

The aim of quantum network is to send quantum information from one place to another. Quantum network is almost sure to be implemented by photons as they are the fastest and interacts less with the environment. The principal issue in building a quantum network is photon loss. Although photons interact less with the environment, single photons are still lost fairly quickly. Due to quantum no-cloning theorem [47, 48] photonic qubits can not be copied either. To circumvent the photon loss problem there are several approaches to building quantum networks [1]. Entangled photon pairs can be sent directly through optical fibres or in free space through air [49]. However, these are constrained to short distances due to the absorption loss faced in fibre and in air. Absorption loss scales exponentially with distance and qubit transmission rate drops quickly after a certain distance - for fibres around 500 km [50], while only around 150 km for air transmission [51, 40]. To reach further distances, quantum repeater protocol was designed through which photons can be sent over thousands of kilometres through optical fibres by using quantum memory to cleverly store photons reducing loss [52, 53, 54, 1]. However, even repeaters can not reliably distribute quantum information beyond 1000 to 2000 km, although there exists some proposals for larger distances [55]. A different approach employing quantum satellites is being taken over the last decade to reach long distances which has been quite successful and is progressing rapidly [45, 56, 57, 56, 58, 59]. Satellite transmission faces diffraction loss which increases only quadratically with distance. Multiple proposals combining satellites and quantum memories or repeater protocols have been put forward to reach truly global distances of 10,000 to 20,000 km [1]. The two different approaches to quantum networks - quantum repeaters and

satellite transmission - are explained in detail next. Finally the proposed memory-satellite protocols for global distances are discussed along with the importance of QND detection there.

3.2 Quantum Repeater

The goal of quantum network is to send quantum information to far away places. However, as discussed before due to photon loss in direct transmission and the quantum-no cloning theorem [47, 48] this can not be done as easily as classical information transfer. Quantum repeaters are designed to solve the photon loss problem by cleverly distributing entangled states over long distance using quantum memories. Then quantum information can be transferred between distant places by teleportation using these entangled states generated by a quantum repeater.

We showed the design of a quantum repeater in Fig. 3.1. Fig. 3.1(a) shows the basic scheme of teleportation on which the whole design of quantum repeaters relies on. The state of qubit 1 is teleported to distant qubit 3 by teleportation using already existing entanglement between far away qubit 2 and 3. The process to generate this entanglement will be discussed later. The teleportation operation (shown by green dashed ellipse) depends on the system used. It consists of an entangling gate followed by measurement. This is a Bell-state measurement for photonic qubits, while for atomic qubits it is a two-qubit entangling gate followed by measurement. Afterwards, the measurement result needs to be transferred by classical channel and a single qubit gate conditioned on the measurement results needs to be performed on qubit 3 for it to acquire the state of qubit 1. These additional steps are not shown in the Fig. 3.1(a) to keep it simple.

In Fig. 3.1(b) we show that entanglement distribution by teleportation forms the basis of a quantum repeater. In a quantum repeater, entanglement is distributed over long distance by simply teleporting the state of one qubit of an entangled pair, as we can see the state of

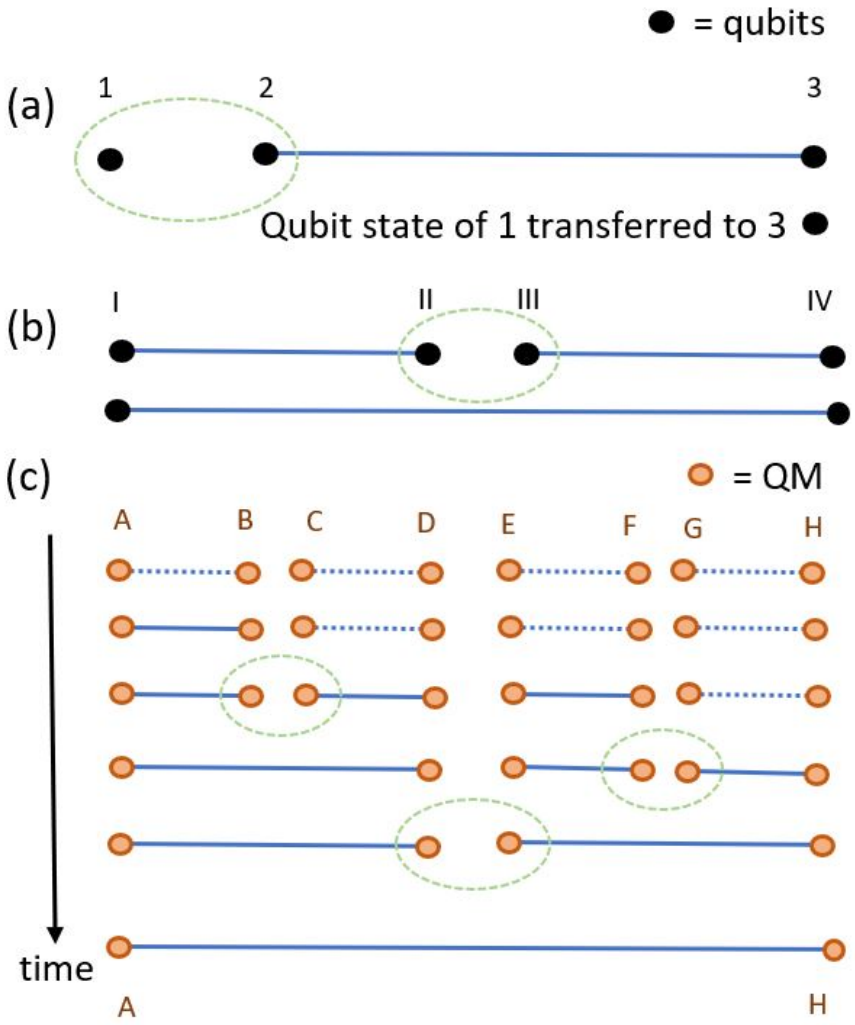

Figure 3.1: (a) Teleportation – Initially distant qubits 2 and 3 are entangled (shown by solid blue line), while qubit 1 is separate with its own quantum state but physically close qubit 2. In the next step, the qubit state of 1 is teleported to the distant qubit 3 by doing a joint operation on qubits 1 and 2. This operation (shown by green dashed circle) consists of an entangling gate followed by measurement. For photonics qubits this is can be Bell-state measurement, while for atomic qubits it is a two-qubit entangling gate followed by measurement. Further classical communication of the measurement results and single qubits gates on qubit 3 based on the measureement results is needed to complete the teleportation process. This is not shown in the figure for simplicity, mentioned in detail in text. (b) Teleporting an entangled qubit (say II here) to a distant location (say, at the place of IV) forms the basis of quantum repeater. This enables entangled distribution over longer distances. (c) A schematic diagram showing working principle of quantum repeater. Initially, eight quantum memories (A-H) are not connected to each other. Eventually, entanglement between A and H was established though successive tries of entanglement generation, storing and eventually performing the entanglement swapping operation (See text for details).

II is teleported to IV here.

However, this is not all. One must have reasonably entangled qubits I-II and III-IV already. This entanglement generation process is described in details in Section 3.2.1. One way to achieve this - without using any further devices, specifically quantum memories - is that entanglement can be distributed by directly transmitting entangled photons through optical fiber over the smaller links. However, the optical fibers still have loss, even at small distance. This means that the probability that photons would be transmitted simultaneously in both links (I-II and III-IV) successfully is equivalent to the probability to directly transmit a photon over the whole distance (i.e. I to IV), as the probabilities of transmission over I-IV is nothing but the probabilities of transmission in I-II and II-IV links multiplied. So, we end up with the same problem we were aiming to solve.

To solve this issue, quantum memories are used, and they play a pivotal role in quantum repeater. In the above example using quantum memories would mean storing all the photonic qubits (I,II,III,IV) in quantum memories. This way when entanglement is created in one link (say I-II) but entanglement creation fails in the other link (III-IV), we can store the entangled qubits in I-II link in quantum memories while we wait for the other link to succeed. When both links succeed, we perform teleportation (called entanglement swapping in context of quantum repeaters) to create entanglement between I and IV.

This basic working principle of a quantum repeater is described in detail in Fig. 3.1(c). Initially, eight quantum memories (A-H) are not connected to each other. Quantum memories B-C, D-E and F-G are physically close to each other. The dashed blue lines show the effort to entangle two distant memories (say, A-B or C-D) using photons. This effort sometimes succeeds and sometimes fails. When it succeeds the created entangled state is stored in the quantum memories, while we attempt the failed ones again. After a try, we may see that only A-B succeeds while others do not. Entanglement in memories A-B is stored while we try others. The second try is a lucky one where two entangled states are created (C-D an E-F). Now both sets of memories A-B and C-D are entangled and hence (as shown in

(b)) we can entangle A-D by performing entanglement swapping. Repeating the same procedure, in the next step when G-H is successfully entangled, E-H can be entangled. Finally, with memories A-D and E-H entangled already, A-H is entangled, completing entanglement distribution from A to H. In principle, the entanglement swapping operation can also fail and then you need to start from the beginning for that part of the repeater. We do not show it here for simplicity. The scheme shown above is an exaggeration in other ways too. Generally to entangle two qubits many attempts are needed and most attempts will return no entanglement generation at all. All these failed attempts are not shown either for obvious reasons.

The quantum memories described above are an essential part of the quantum repeater. They need to store certain qubits (e.g. A in Fig. 1(c)) from the time entanglement in created the first time there (e.g. in A-B link), until entanglement distribution in the whole link is finished. Hence, memories must have long storage time. The storage time is fundamentally bounded from below by the light travel time in the links. Except the storage time, the memories also need to be high efficiency and have multimode capacity for a reasonable entanglement distribution rate [1, 52]. As many memories are involved in multiple nodes, low efficiency would make the rates drop dramatically. The rates of the repeater protocols, especially at large distances, is not very high without multiplexing. Multiplexing is using multiple photons of a particular mode (e.g., of frequency mode or temporal mode or spatial mode) together in a repeater to increase rate. It is very advantageous as the entanglement generation rate is proportional to the multiplexing rate. Thus, rates can be improved by orders of magnitude even with moderate multiplexing. However, these strict requirements on the quantum memories are one of the most significant barriers towards successful implementation of a quantum repeater.

Another essential requirement for quantum repeater is generation of heralded entanglement [52]. Heralded means that it is known when entanglement is successfully created in an elementary link (say in A-B link). The entanglement generation attempt may fail many

times, that is the photons may get lost in the optical fiber. However, when it succeeds, we can get to know about it in two ways. One would be using non-destructive detection or QND detection on photons where the photon is detected without disturbing its quantum state. This is however a difficult task as described earlier. Another easier path is followed by most quantum repeater schemes where the quantum memories are entangled with single photon(s) and by measuring the single photon(s) in the middle of the link by Bell-state measurements the two quantum memories are entangled. This technique is discussed in detail for the quantum repeaters scheme described below.

3.2.1 DLCZ scheme

The fundamental structure of quantum repeater described above was proposed by Briegel et. al. [53]. One of the early proposals to implement such a quantum repeater was given in 2001 by Duan, Lukin, Cirac and Zoller [54] - widely known as the DLCZ protocol. The DLCZ protocol portrays possible implementation techniques for entanglement generation and entanglement swapping needed in a quantum repeater which was taken as granted earlier in Fig. 3.1. The basic ideas of DLCZ protocol are depicted in Fig. 3.2. The proposal is based on ensemble quantum memories, particularly on atomic ensembles where each atom is considered a three-level system with two ground states $|g_1\rangle$ and $|g_2\rangle$ and an excited state $|e\rangle$. The essential part of the proposal are the 'write' and 'read' pulses shown in Fig 3.2(a). The 'write' pulse is used to write a qubit state into the quantum memory while the 'read' pulse is used to read it out. The 'write' pulse is a laser pulse which is detuned from $|g_1\rangle$ - $|e\rangle$ transition. The 'write' laser pulse intensity is set such that it occasionally produces a photon by Raman scattering and simultaneously stores an atomic excitation in $|g_2\rangle$ state. Because of the low probability of producing a photon the probability of creating a two photon state is very low. Using the 'write' pulse from two such atomic ensembles an entangled state of the atomic ensembles can be created as shown in Fig. 3.2(b). When one photon is detected in the detectors then the detected photon may come from either A or B atomic ensemble

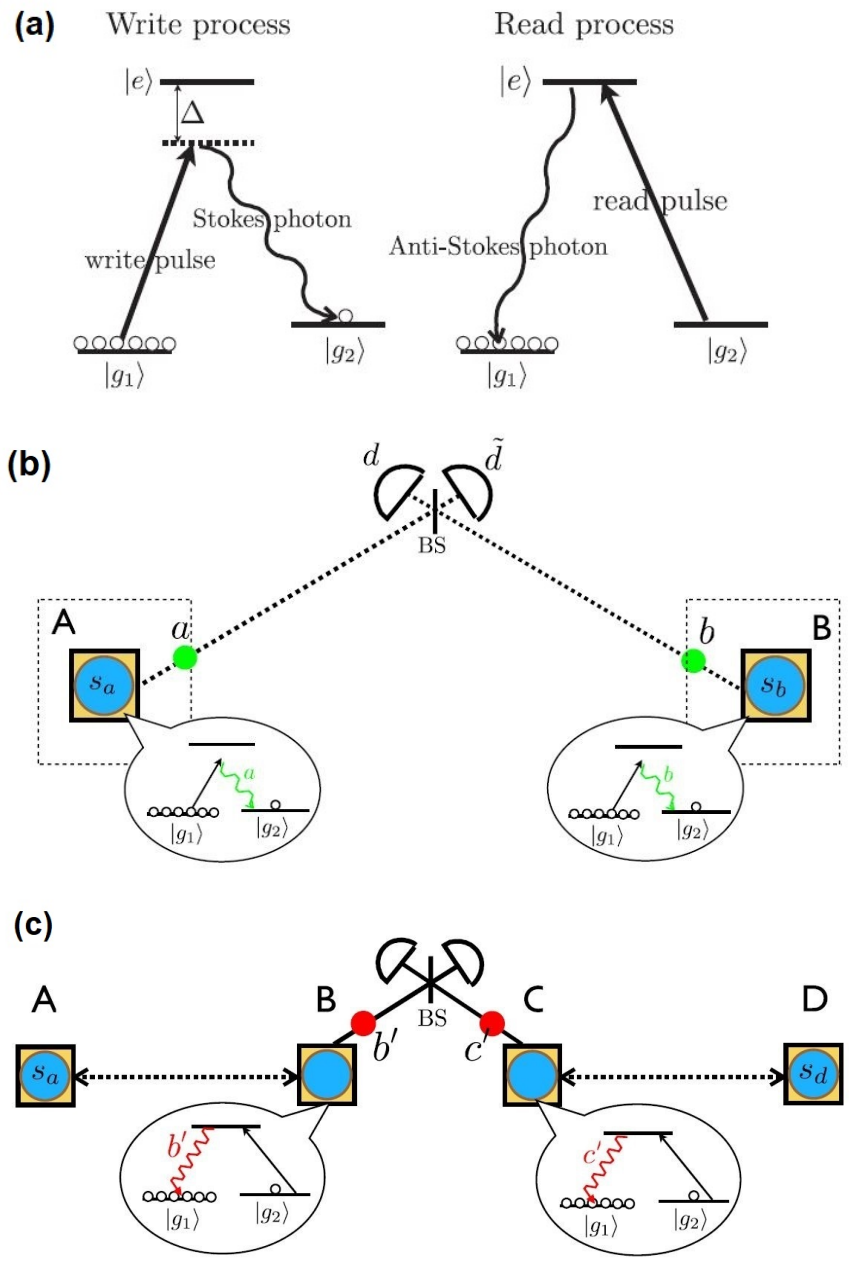

Figure 3.2: (a) A schematic diagram showing the working of 'write' and 'read' pulses in DLCZ scheme. 'Write' pulse is used to encode or write a qubit state in the atomic ensemble while the 'read' pulse is used to decode or read out the qubit state. (b) Entanglement generation using 'write' pulse. Two atomic ensembles are entangled by detecting a single photon in the photo-detectors (d,$\tilde{d}$) at the middle (BS - Beam splitter). (c) Entanglement swapping using read pulses. Two atomic ensemble are entangled and measured to perform the teleportation operation described in Fig. 3.1. See text for further details. Reprinted with permission from [52].

creating an entangled state -

$$\frac{|01\rangle + |10\rangle}{\sqrt{2}}$$

where $|0\rangle$ represents the absence of an excitation in the atomic ensemble while $|1\rangle$ represents a single collective excitation - i.e., $|0\rangle = |g_1 g_1 ... g_1\rangle$ and $|1\rangle = (|g_2 g_1 ... g_1\rangle + |g_1 g_2 ... g_1\rangle + |g_1 g_1 ... g_2\rangle)/\sqrt{N}$ - for each ensemble.

This state is created because there is no way to tell which path the photon came from. This will accomplish entanglement generation. For entanglement swapping procedure the 'read' pulse is needed. 'Read' pulse is resonant on the $|g_2\rangle$ - $|e\rangle$ transition which reads out the atomic excitation and efficiently turns it into a photon along a particular direction due to a collective interference effect [52]. Entanglement swapping using the 'read' pulse is shown in Fig. 3.2(c). The retrieved photons from two adjacent memories B and C can be used to do a Bell state measurement (BSM) and perform the teleportation operation. 'Read' pulse can also be used for retrieving stored photons for final use of entanglement.

DLCZ was an early repeater protocol and hence had several limitations [54] . The 'write' laser pulse intensity must be kept low enough to prohibit two-photon generation. However, this means the single-photon generation rate is also low. Multiplexing is not considered in this protocol. Other limitations include finding atoms which can store telecom frequency photons. Telecom photons at 1550 nm wavelength are used in classical communication because this is the wavelength for which the optical fibre loss is minimized. This is because photon generated during qubit storage themselves travels through the fiber. Limited success probability of entanglement swapping using Bell state measurement in another issue [60].

To solve these and other problems many novel repeater schemes were designed over the years [61, 62, 63, 64]. For example, one of these is using an entangled pair source and multimode memories [63]. This scheme transmits and stores separate photons from an entangled pair solving the telecom frequency storage issue while multimode storage is taken care of using multiple time bin qubits stored in the multimode memories.

We discussed ensemble quantum memories and repeater schemes above. There are many quantum repeater proposals using single systems (i.e. atoms, ions, nitrogen vacancy centres, quantum dots etc.) in which significant progress has been made [65, 10, 11]. The principal scheme is generally similar. Difference lies in the storage medium where a single system is used instead of an ensemble.

Research on different quantum repeater protocols and physical systems is still ongoing. Significant progress has been made in many respects over the years. Full scale quantum repeaters are still confined to small distances (below 100 km) [10, 66, 67, 11] and have not beaten direct transmission yet mainly due to the strict requirements on the quantum memories [1, 52]. Moreover, due to the many complexities in its design quantum repeaters cannot stretch much further than 1000-1500 km, although some proposals for longer distance exist [55].

To reach large distances an alternative pathway of transmission from orbiting satellites has become attractive and manifestly successful over the last decade. We explore the advantages and challenges of transmitting quantum information from orbiting satellites next.

3.3 Satellites

The rise of quantum communication satellites has been a spectacular event over the last decade. Satellites achieved entanglement distribution over 1200 km [45], which is impossible currently with any fibre-based architecture. This has been possible as satellite loss is principally due to diffraction which varies quadratically with distance compared to the exponential absorption loss like in optical fibre or air transmission. Diffraction loss occurs due to beam divergence. So along with distance, diffraction loss also depends on the ground and satellite telescope diameters. Large ground telescopes (diameter in meters) are common. However, satellite telescopes are restricted to smaller sizes (in tens of cm) as large telescopes are heavy and expensive. Incorrect beam pointing is another big source of error. A low earth orbit

(LEO) satellite goes around the earth almost every 90 minutes. To point a light beam at or detect a beam from such a satellite (say, with a 30 cm diameter telescope at 500 km elevation) satellite tracking error below 30 cm / 500km $\sim$ microradians is needed. Hence, developing a sophisticated satellite tracking technology is one of the most important parts of a Quantum satellite mission [68].

3.3.1 Atmospheric transmission

Atmospheric transmission loss is another significant loss factor which consists of absorption in atmosphere and atmospheric turbulence. Absorption loss depends on wavelength of light and angle of incidence through the atmosphere [68]. Light to or from satellites can not be incident at a very large angle with respect to Earth as grazing incidence increases absorption loss dramatically because absorption loss varies exponentially with distance.

Atmospheric turbulence causes significant issues too. Turbulence generates random fluctuations in the refractive index of the air which results in beam spreading, beam wondering and even beam fragmentation, effectively increasing the beam size causing losses. Turbulence is most pronounced close to the surface of the earth and practically ends at 20 km, after which the atmosphere itself is too thin to be considered. Turbulence does not affect downlink transmission significantly as the beam does not have any propagation length after going through the turbulent atmosphere. However, in uplink transmission after the turbulence, the beam must propagate for hundreds of km resulting in very large beam size at the satellite.

Adaptive optics systems can help compensate for the turbulence effect by first surveying the atmosphere by detecting a reference light and then introducing beam tilt and wavefront corrections to the outgoing uplink beam using segmented mirror telescopes. Atmospheric turbulence effects change in the time scales of 10-100 ms. When laser pulses shorter than that duration are used atmosphere's refractive index variation remains frozen which can be surveyed and compensated.

Compensation does not generally work very well as it is quite difficult to survey beforehand the exact part of the atmosphere through which the uplink beam would propagate. If a downward laser from the satellite is used as reference light source it would pass through a different part of the atmosphere than the uplink beam as the satellite would move in the meantime. Hence such an offset downward reference laser would only cause negligible improvement. A much better results can be obtained using Laser Guide Stars (LGS) which are artificial stars created by shining powerful laser beam at sodium level of the atmosphere at around 90 km elevation [69]. The light from this artificial star transmitted to the turbulent atmosphere is detected on earth to compensate turbulence effects. LGS provides much better results as compared to an offset downward laser because LGS can be created in the direction of the uplink transmission without any offset.

Even then the light would not pass from the exact same area of the atmosphere as light would pass through two opposite cones for the downwards propagating light from LGS and uplink transmission towards a satellite. This is called the cone effect. Due to the cone effect and other reasons losses for turbulence cannot be completely compensated using AO systems [69]. As it is evident from the above discussion AO system is also quite complicated requiring segmented mirrors, LGS etc. This implies that the uplink turbulence loss remains a thorny issue for quantum communication.

3.3.2 Satellite transmission protocols

Many different quantum transmission protocols are possible using quantum satellites. Photonic qubits can be sent from satellite to ground (downlink), ground to satellite (uplink) or entangled photons can be sent to two points on Earth from a source in the satellite via downlink transmission. Downlink qubit transmission can also be achieved using retroreflectors on board satellites which works as polarization modulators. Weak laser pulses are sent to the satellite and the retroreflector on the satellite, working as polarization modulator, chooses the polarization of the reflected downlink photonic qubit [70].

There have been many feasibility studies for quantum satellites to ascertain parameters like total loss or background noise in downlink or uplink transmission. Studies are considered to include the basic factors [71] as well as advanced studies to consider all effects precisely [68]. Initial experiments were also conducted using optical sources or retroreflectors present in existing satellites. These experiments checked different parameters like conclusively proving that a polarization qubit would not decohere due to turbulence in atmospheric transmission [72, 70].

In 2017, in culmination to all the previous work, the Micius satellite was launched by China which achieved several milestones including entanglement distribution over 1200 km [45], quantum teleportation to the satellite over 1400 km [57] and several successful Quantum Key distribution demonstrations [73, 58, 59, 56]. The different protocols performed by Micius satellite are shown in Fig. 3.3. Micius satellite was equipped with two telescopes (with diameters 30 cm and 18 cm), PPKTP (Periodically Poled Potassium Titanyl Phosphate) based SPDC (Spontaneous Parametric Down-Conversion) entangled photon source, a weak coherent pulse (WCP) source to carry out BB84 quantum key distribution (QKD) schemes and single photon detectors. It also had more lasers, alignment optics and detectors to be used for satellite tracking [Acquiring pointing and tracking (APT) system] and polarization correction. Using the entangled pair source entanglement was distributed between two ground stations separated by 1203 km on earth [45]. They perform the Bell inequality violation test on this entangled pair which increased the Bell test violation distance by almost an order of magnitude. There has been an entanglement based QKD scheme with this entangled pair too [56]. Micius performed QKD in the downlink using WCP source through the BB84 protocol separately [58].There has also been an uplink transmission experiment where a photonic qubit has been teleported from ground to the satellite [57]. The teleported photonic qubit is detected using the single photon detector onboard the satellite. The unknown qubit which is teleported originated from another entangled source by heralding, generated using the same pump laser as used for the other entangled pair. This was needed for a complete

overlap in the beam splitter before the measurement.

Several trusted node QKD experiments were performed using Micius where the satellite is considered as a trusted node or relay [59, 74]. In one such experiment, a Quantum encrypted video call was conducted between Austria and China [59]. More recently, in another experiment trusted node QKD has been performed over 4600 km between two cities in China, with trusted nodes in both ground and satellite [74]. Plans were already floated to launch a whole fleet of quantum satellites to perform Global trusted node QKD [75]. Trusted node QKD using satellite nodes is currently viewed as more secure than ground nodes because satellite nodes are perceived to be less hackable, at least for now. This may very well change with advances in space technologies.

However, LEO satellites cannot establish entanglement beyond $\sim$ 2000-3000 km due to the curvature of earth. This is needed for truly secure QKD and other applications like distributed quantum computing in large distances. To reach far away distances one needs either higher orbit satellites or a memory-satellite combined schemes. Satellites in geostationary (GEO) orbit (at 36,000 km elevation) or even lower medium earth orbits (orbits between LEO and GEO) can establish entanglement between two places in earth, apart from each other by around 10,000 km. However, the rates will be low as a photon has to travel a long distance coming from the higher orbits [37]. Some early experiments were performed using retroreflectors in higher Earth orbits to reflect back photons sent from earth to model the high orbit transmission [37].

3.4 Memory-Satellite protocols and QND detection

Even geostationary satellites cannot send photons much further beyond 10000 km though. Even before the earth's curvature gets into the way the grazing incidence of photons through the atmosphere causes high enough loss [37]. Hence, for truly Global distances of 10,000 to 20,000 km one would need other protocols combining quantum memory and satellites [37].

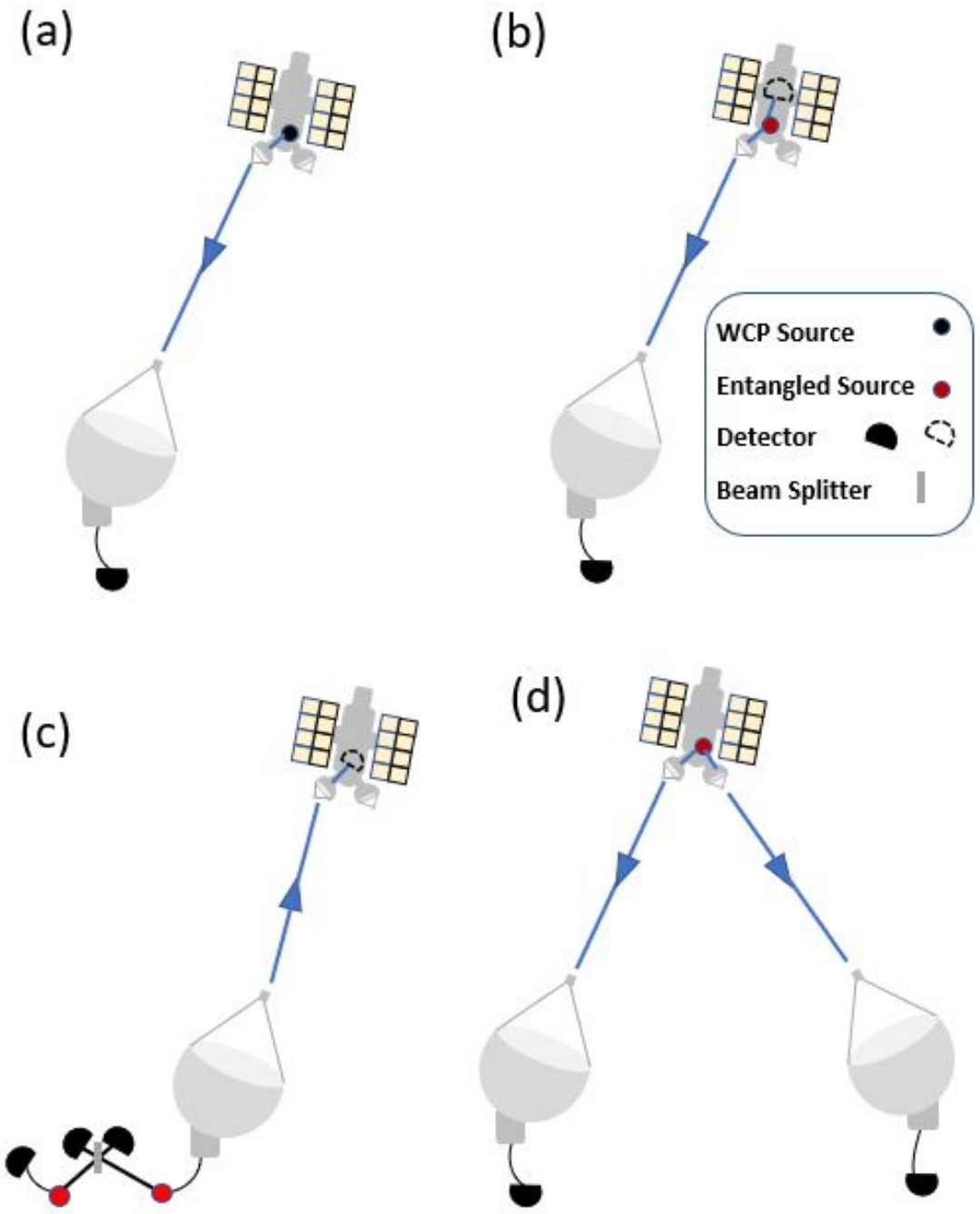

Figure 3.3: Different experiments performed with Micius satellite [73, 45, 57, 58]. (a) Downlink QKD - Using a weak coherent pulse (WCP) source (black circle) photons are sent downlink to ground station to perform decoy-state QKD [58]. (b) Entanglement based QKD - An entangled pair source (red circle) aboard Micius is used to perform QKD [73]. (c) Uplink teleportation - Entangled photon pair source (red circle) in ground station is used to teleport a qubit to satellite. The unknown qubit, to be teleported, also comes from another entangled pair for technical reasons. See text for details [57]. (d) Entanglement distribution in downlink- Entangled photon pairs are distributed between two ground stations, separated by a record 1203 km on earth, by downlink transmission [45].

Such protocols would also be useful for smaller distances to increase the rate.

The first such protocol was given in [37]. It is depicted in Fig. 3.4(a). Quantum non demolition (QND) detectors are necessary for this protocol along with Quantum memories (QM). Both QND detectors and memories are kept in ground for the sake of easy operation and maintenance while satellites containing source will send entangled pairs to the ground stations. The successfully transmitted entangled pairs would be detected by QND detectors and stored in memories. There would be entanglement swapping between the quantum memories later, as shown in Fig. 3.4(a) using Bell state measurement (BSM). In [37] an equatorial satellite constellation was proposed. However, this method will work for a general constellation of satellites to distribute entanglement between any two points on earth. QND and QM were kept in the ground stations in [37], although they can alternatively be in a satellite too as proposed in [76]. Although seemingly difficult this may be possible, especially in light of recent successful atomic and optical physics experiments in space [77, 78]. QND and QM placed in satellite would evade the extra downlink and atmospheric loss and dependence on weather conditions on multiple links simultaneously for successful entanglement transfer over a long distance.

Multiple other architectures are possible using memories and satellites. One such proposal, as described in Fig. 3.4(b), consists of a putting a very long-term memory in satellite which also contains an entangled source [1]. One photon of the entangled pair is transmitted downlink while the other is stored in the memory. The satellite then moves from one place to another physically and when it reaches the destination the stored photon is retrieved and sent downlink. This protocol would require a very long storage time memory with storage time at least in minutes, preferably in order of an hour as the satellite needs to physically move over a large distance for this to be useful. In this context, rare-earth ion based solid state system has been investigated with coherence times as large as 6 hours [79], although a functioning quantum memory with such long coherence time has not been constructed yet. Moreover, the memory must have high multimode capacity through spatial, temporal

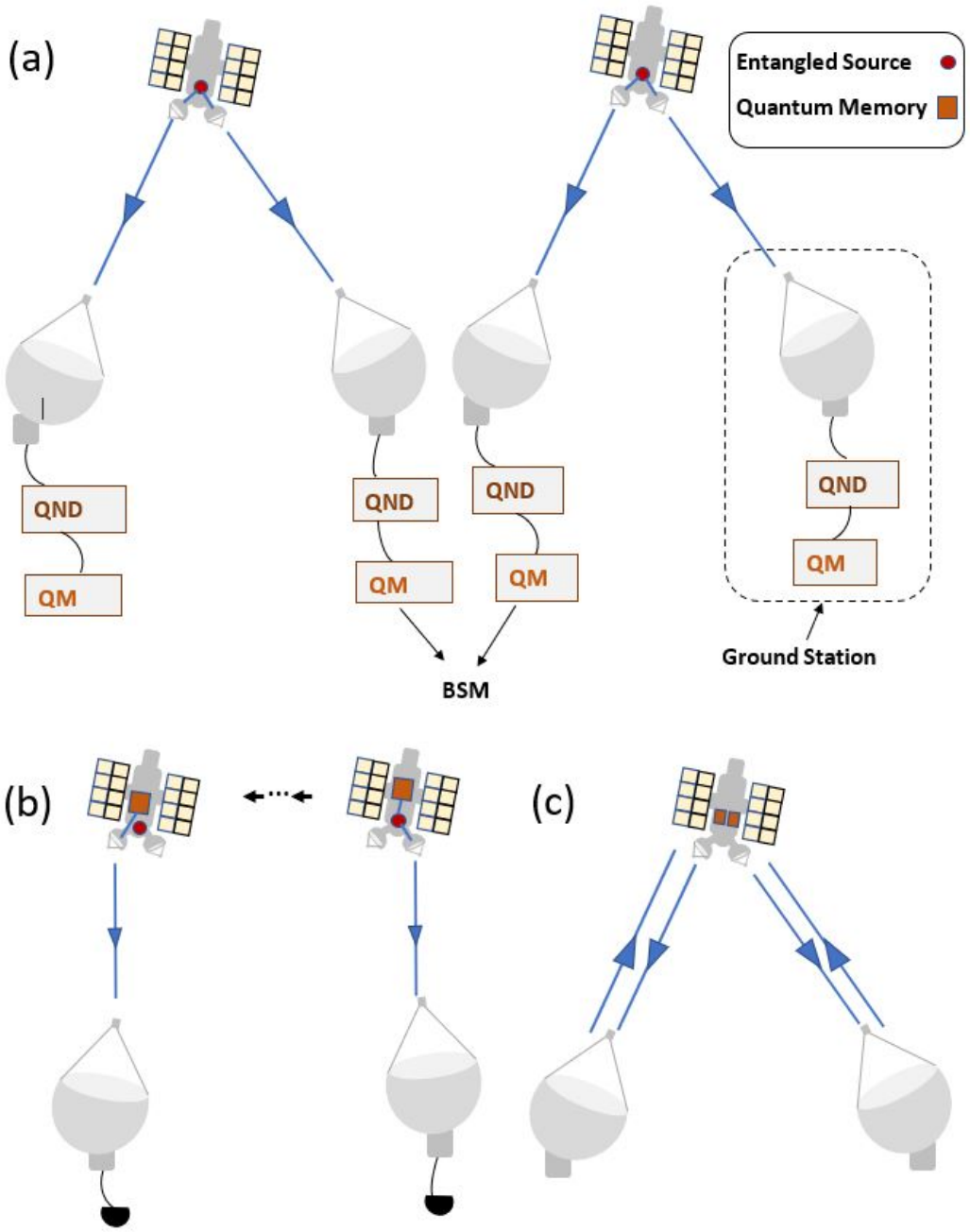

Figure 3.4: Some of the many memory-satellite combined approaches to distribute entanglement. (a) A repeater protocol over LEO satellites to distribute entanglement over global distances using quantum memories (QM) and quantum non-demolition (QND) detectors in ground stations [37]. (b) Entanglement is distributed using a very long-term memory. One Photon of an entangled pair is stored in the memory (red Square) which is later retrieved and transmitted downlink once the satellite has physically moved to a far-away destination [1]. (c) Memories on board satellites can facilitate entanglement distribution for both uplink and downlink transmission [76].

or frequency multiplexing for effective transmission rate as there is a large time delay due to physical movement of the satellite ($\sim$ 1000s). Considering this time delay in transmission, sending a single qubit in a single journey would be equivalent to transmission at the rate of only $10^{(-3)}$ qubits/second which is very low. Hence, multiplexing is necessary.

Another protocol is described in 3.4(c), where memories are kept in the satellites which can enable both uplink and downlink transmission and use single photon transmission instead of entangled sources in both the downlink and uplink. Source and detectors can be in both ground stations and the satellite. Source and detectors are not shown in Fig. 3.4 (c) for simplicity. When memories present in the ground link too this scheme can generate entangled photons without using Quantum non-demolition (QND) detectors. A Bell state measurement needs to be carried out of the two photons transmitted in the uplink from two ground stations. This can be achieved with or without Quantum memories in the satellites, although memories would help. However, as described earlier uplink transmission has higher loss due to turbulence. Adaptive optics systems can be helpful in reducing turbulence although those are complicated and their influence limited. Hence the scope for entangled distribution using uplink transmission is limited and would provide much lower rates than downlink even when it becomes possible. Hence downlink transmission would be preferable. However, downlink transmission would require quantum non demolition measurements detectors to successfully store and use entanglement. Such a QND measurement proposal to know the presence of a single photon, without destruction of its qubit state, is presented in the next chapter (based on our paper [16]) .

Chapter 4

Theory of cavity-enhanced nondestructive detection of photonic qubits in a solid-state atomic ensemble

Preface

This is the first paper of the thesis proposing a non-destructive photon number detection (or QND detection) using a solid state system. Non-destructive photon number detection has applications in a range of areas - from quantum network architectures to quantum computation schemes and beyond. Here we present a proposal for non-destructive detection of a single photon using an ensemble of rare-earth ions inside a nano-photonic cavity.

This work was done in collaboration with my co-authors. I have carried out the numerical modelling and associated calculations. I have written most of the paper, with input from my co-authors.

Theory of cavity-enhanced non-destructive detection of photonic qubits in a solid-state atomic ensemble

PHYSICAL REVIEW A 98, 043842 (2018)

Sumit Goswami[1], Khabat Heshami[2,3], Christoph Simon[1]

[1]*Department of Physics and Astronomy and Institute for Quantum Science and Technology, University of Calgary, Calgary, Alberta, Canada T2N 1N4*

[2]*National Research Council of Canada, 100 Sussex Drive, Ottawa, Ontario, Canada K1A 0R6*

[3]*Department of Physics, University of Ottawa, 598 King Edward, Ottawa, Ontario, Canada K1N 6N5*

Abstract

Non-destructive detection of photonic qubits will enable important applications in photonic quantum information processing and quantum communications. Here, we present an approach based on a solid-state cavity containing an ensemble of rare-earth ions. First a probe pulse containing many photons is stored in the ensemble. Then a single signal photon, which represents a time-bin qubit, imprints a phase on the ensemble that is due to the AC Stark effect. This phase does not depend on the exact timing of the signal photon, which makes the detection insensitive to the time-bin qubit state. Then the probe pulse is retrieved and its phase is detected via homodyne detection. We show that the cavity leads to a dependence of the imprinted phase on the *probe* photon number, which leads to a spreading of the probe phase, in contrast to the simple shift that occurs in the absence of a cavity. However, we show that this scenario still allows non-destructive detection of the signal. We discuss potential implementations of the scheme, showing that high success probability and low loss should be simultaneously achievable.

4.1 Introduction

The ability to non-destructively detect photonic qubits - without absorbing the photon and without revealing its qubit state - would enable important applications in photonic quantum information processing and quantum networks. For example, photon number resolving quantum non-demolition detectors and feed forward would allow implementing deterministic two-qubit gates in linear optical quantum computation [39], and non-destructive detection of time-bin qubits unlocks the path to novel quantum network architectures [80, 1]. One promising avenue towards this goal is quantum non-linear optics [81]. Significant advances have been made through strong nonlinear interactions in atom-cavity systems [82], nonlinearities mediated by Rydberg atoms [83] and AC Stark shift [84, 85, 86, 87].

Recent progress in cavity-enhanced light-matter interfaces involving rare-earth ions (REI) succeeded in solid-state implementation of quantum memories and controlled light-matter interaction in single or ensembles of REIs doped into a crystal [88, 89, 90, 91, 92]. This promises a path towards robust and scalable implementations of photonic quantum information processing. Driven by progress in coupling REI to nano-photonic cavities, a proposal for non-destructive photon detection based on a single REI coupled to a photonic cavity has been developed [93]. However, at the current state of technology it is still challenging to achieve situations where a single ion is coupled to a cavity in a reproducible and scalable way. For practical reasons, it is therefore also of interest to consider employing REI *ensembles* in photonic cavities for non-destructive detection of photonic qubits.

One form of nonlinear interactions based on atomic ensembles is to use a single photon to impart a detectable cross-phase shift on a multi-photon coherent probe field [94, 95]. The simultaneous presence of signal and probe fields in different configurations in an atomic system enables cross-phase modulation based on the AC Stark shift [84, 96]. This effect is sensitive to the spatio-temporal overlap of probe and signal fields. Storing the probe field in the atomic ensemble eliminates any sensitivity to the timing of the signal [97], which can be exploited for non-destructive detection of photonic time-bin qubits without revealing

any information about the time-bin state of the signal, as proposed in Ref. [33]. Single-shot and non-destructive detection of single photons based on AC stark shift was shown to be impossible for a single pass through atomic ensembles, as off-resonant absorption loss becomes prohibitive for cross-phase shifts larger than the intrinsic phase uncertainty of the probe field [33]. This limitation can be circumvented with multiple passes through the medium [33] or by enhancing the cross-phase shift with a cavity. The multi-pass approach is difficult to realize in practice because it requires very low-loss switches. On the other hand, as we will see below, the cavity introduces complications that were not analyzed in Ref. [33], motivating the present study.

In this paper, we analyze a scheme to construct a single photon QND detector in a solid-state REI ensemble inside a cavity. A probe field is initially stored in the atomic ensemble. Then a single-photon signal that is resonant with the cavity and off-resonant with respect to the atomic transition interacts with the atomic ensemble; see Fig. 4.1. The single photon signal is considered to carry quantum information encoded in its timing [98]. Due to the AC Stark shift [99], a phase is imparted on the state of the atomic ensemble that contains a stored probe field. The phase shift on the atomic state leads to a phase shift on the retrieved probe field. Given that the cross phase shift is cumulative and the probe field is stored during the interaction, the phase shift on the retrieved probe field will not reveal the time-bin qubit state of the signal. In the absence of a cavity [33], an initial coherent state of the probe field $|\alpha\rangle$ is retrieved as $|\alpha e^{i\phi}\rangle$, where the signal pulse induces a phase shift ϕ on the probe state. For multiple passes this phase shift is simply multiplied by the number of passes. In contrast, in the current scheme, we find that the cavity resonance becomes sensitive to the number of atoms in the ground state, which depends on the photon number distribution of the stored probe field. This leads to a dependence of the cross-phase shift (due to the single-photon signal) on the photon number distribution of the probe field.

This paper is organized as follows. After discussing the storage of the probe field in section II, we analyze the cross-phase shift in detail in section III. In section IV, we show our

results for a practical discrimination between a single photon and vacuum through quadrature detection. In section V, we describe an implementation based on rare-earth ion ensembles in nano-photonic cavities. In section VI, we conclude that the implementation of non-destructive photonic qubit detection should be within reach for the present approach.

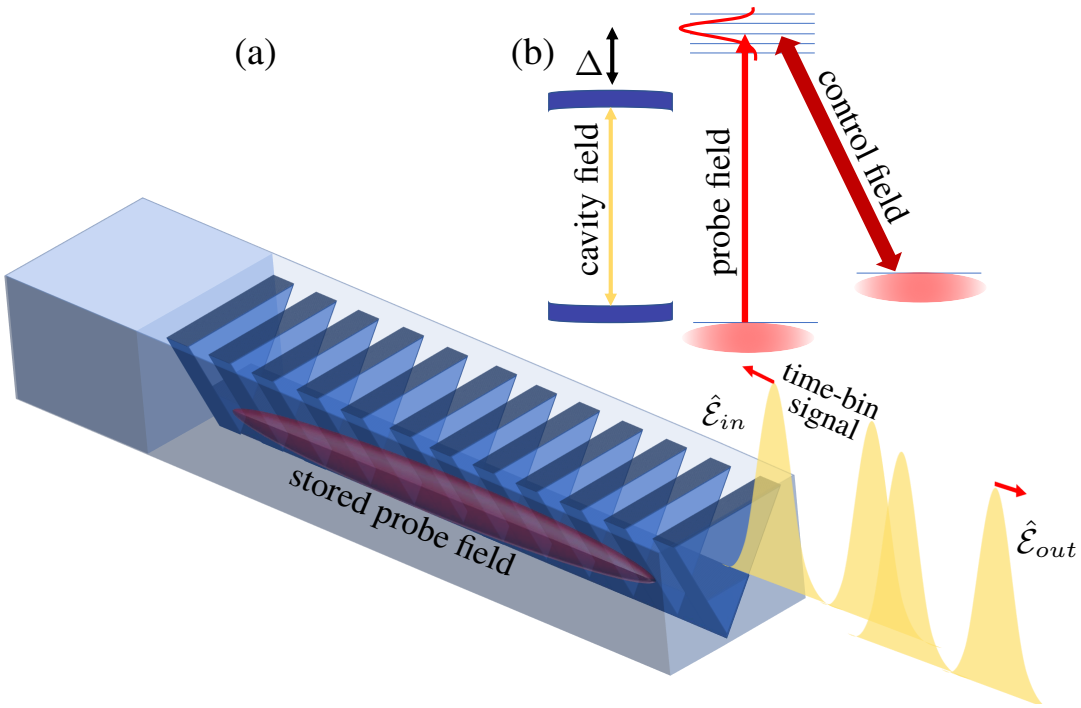

Figure 4.1: (Color online) Scheme for non-destructive detection of a photonic time-bin qubit. (a) Input and output single-photon time-bin signal fields interacting with a nanophotonic crystal cavity coupled to an atomic ensemble that contains a stored probe field. (b) Atomic level configuration for storage of the probe field in the atomic ensemble. The cavity is in resonance with the probe for the storage process, but is detuned from the probe and brought into resonance with the signal for the non-destructive detection.

4.2 Probe storage

The proposal has two almost independent parts. First, it needs to be ensured that the probe pulse, in a many photon coherent state, can be efficiently stored and retrieved from the ensemble. Next comes the consideration that the signal, without being absorbed, can give

enough phase shifts to the atomic ensemble storing the probe that the retrieved probe state can be distinguished from the initial probe state.

In section 4.3 we focus on the the phase shift due to the signal on the probe. However, to have that effect we need to store and retrieve the probe pulse efficiently. Light storage in quantum memories has been demonstrated in single photon level in variety of systems [100, 101, 102, 103, 104]. Specifically, single photon storage has been demonstrated conclusively in rare-earth ions doped crystals using Atomic Frequency Comb (AFC) quantum memory protocol with the added advantage of multimode storage [101, 102]. With our probe pulse, we are aiming to store a relatively intense coherent pulse which is in principle simpler than storing a single photon. The only significant difficulty regarding storing an intense pulse is that the number of photons stored should be much lower than the total number of atoms participating in the storage. Otherwise a significant portion of the atoms will reach the excited state during storage which will violate the assumptions of the standard linear quantum memory storage protocols [105]. In Section 4.5 we provided numerical estimates for parameters of our proposal where we ensured such a parameter regime.

One of the fundamental constraints for probe storage is governed by the phase shift requirement of our protocol. As we are using an optical cavity, the cavity transverse area must be small to enhance the signal electric field considerably for a large phase shift. Due to this exact same reason of higher lateral confinement to increase the phase shift, waveguides were used in [33].

Storage efficiency of quantum memories increases with increasing optical depth [105] and optical depth is proportional to both density and length of the medium (here, rare earth ions doped inside cavity) light is stored. In case of probe storage without a cavity, as in the waveguide case of [33], storage pulse can be incident along the same direction (e.g. along the waveguide in [33]) as the signal. But in presence of a cavity the probe cannot be stored directly along the cavity if the signal and probe are detuned. This is because to maintain low signal loss we must detune the cavity from the atoms so that spontaneous emission is

not enhanced. Hence, if the probe needs to be on resonance with the atoms for storage (as in the AFC protocol), it is not in resonance with the cavity anymore. As an alternative one can try to store the probe from the side of the cavity. However in that case, as we need a small transverse area cavity for large phase shift, the transverse length of the cavity is very small resulting in extremely small optical depth. To overcome this problem, the probe pulse must be stored along the cavity where there is enough optical depth and the cavity also enhances the storage efficiency significantly. In the AFC protocol the probe needs to be on resonance with the atoms. Hence to do probe storage along the cavity we need to have the cavity on resonance with the probe (and so with the atoms too) while the probe is stored. However, when the signal arrives, we need the cavity to be on resonance with the signal and detuned from the atoms to keep signal loss minimal. To solve this problem, we can dynamically control the cavity resonance frequency so that it is in resonance with the probe for probe storage and retrieval, but in resonance with the signal for non-destructive detection. This is feasible with current technology of piezoelectric motion controllers as we only need to detune the cavity a few picometers within a time span of around microsecond storage times of AFC memory. Requirements for the piezo-electric motion controller are discussed in more detail later, once we estimate the system parameters needed for implementation in section 4.5. About the storage itself, AFC quantum memory protocol has been demonstrated to implement a high efficiency (56 %) quantum storage in rare-earth ion doped crystal inside a cavity [106]. So, with the addition of the dynamical detuning, AFC protocol is one definite way to store the probe efficiently.

Another approach will be to keep the cavity permanently detuned from the atoms. But the probe needs to be on resonance to the cavity to be stored efficiently. Hence, we can implement an off-resonant Raman storage protocol. Although a Raman memory has not been demonstrated in the rare-earth ion doped crystal yet, it has been demonstrated widely in atomic gases [107, 108]. With the recent advancement in fabricating high finesse nano-photonic cavities [109, 110, 104, 88, 89] and stoichiometric crystals [111, 112] implementation

of a Raman memory storage in rare-earth ions seems well within reach.

Concerning the storage state, the probe pulse can either be stored in the excited state or in a second ground state. However, it is preferable to store the probe in a second ground state for multiple reasons. First of all, the memory lifetime will then be limited by spin coherence time of the second ground state instead of the much shorter optical coherence time of the excited state. This will provide more time for the signal to pass and also for the dynamical detuning of the cavity. As the photon number in the probe pulse is a fraction of the total number of atoms, the second ground state contain much less number of atoms compared to the original ground state. So, if the signal photon imparts the phase shift on the second ground state where the probe pulse is stored the loss will be less. Another significant issue will be to store the probe pulse in the excited state will be the probability of stimulated emission while the signal is passing from excited state atoms in which the probe is stored. This may affect the signal fidelity. Hence, storing the probe in a second ground state will definitely be preferred if possible in a particular system. However, it may not be feasible for all systems. It depends on how many ground states are there in the particular system (rare earth ion). If only two ground states are used it may not be feasible for all protocols as the other ground state may be used for optical pumping to prepare a quantum memory. This is what constrained us in our example in Section 4.5 where we used an AFC quantum memory in Nd:YVO. Hence we considered storing in the excited state for this particular example.

4.3 Cross-phase shift in the cavity

4.3.1 Theoretical model for cavity-enhanced QND

In our proposal, once the probe is stored in the atomic ensemble inside the cavity a signal detuned from the atoms passes through the cavity inducing a phase shift on the atomic ensemble through the AC stark effect. A theoretical model is constructed for the phase shift that a signal photon induces on the atoms following [33]. However, our proposal deviates

from [33] in that the phase shift now occurs inside a cavity. As we will see later, cavity modifies the phase shift depending on the number of stored probe photons which we modeled by calculating the cavity field and its interaction with the atoms. Following [33] we start the theory by formulating the total Hamiltonian that governs our proposed system of signal and atomic ensemble.

$$\hat{H}_{tot} = \hat{H}_0 + \hat{H}_{int}, \tag{4.1}$$

$$\hat{H}_0 = \hbar\omega_s a^\dagger a + \sum_\delta \hbar(\omega_{ge} + \delta)N(\delta)\hat{\sigma}_{ee} \tag{4.2}$$

$$\hat{H}_{int} = -\hbar g \left[\hat{\mathcal{E}} e^{i\Delta t} \sum_\delta N(\delta)\hat{\sigma}_{eg}(t;\delta) + H.C.\right], \tag{4.3}$$

where the cavity field $\hat{\mathcal{E}} = \hat{a}e^{i\omega_s t}$.

The Hamiltonians are written in terms of collective atomic operators defined as follows

$$\hat{\sigma}_{\nu\nu}(t;\delta) = \frac{1}{N(\delta)} \sum_{i=1}^{N(\delta)} \hat{\sigma}^i_{\nu\nu}(t;\delta); \nu = \{g, e\}, \tag{4.4}$$

and

$$\hat{\sigma}_{eg}(t;\delta) = \frac{1}{N(\delta)} \sum_{i=1}^{N(\delta)} \hat{\sigma}^i_{eg}(t;\delta) e^{-i\omega_p(t - z_i/c)}. \tag{4.5}$$

where, individual atomic operators for the j^{th} atom at position z_j are given by $\hat{\sigma}^j_{\nu\nu'} = |\nu\rangle^j\langle\nu'|$, with $\nu, \nu' = \{g, e\}$. $N(\delta)$ is the number of atoms in frequency mode δ where the detuning of this particular mode from the central frequency is given by δ. The atomic ensemble has a central frequency given by ω_{eg} while the cavity, on resonance with the signal, is detuned by an amount Δ from the atoms and has a frequency ω_s.

For relatively large detuning Δ, we find an effective interaction Hamiltonian to describe the dynamics of the atomic polarization due to off-resonant interaction with the cavity field $\hat{\mathcal{E}}$. We start by finding the dynamics of the collective atomic operator in the Heisenberg picture

$$\dot{\hat{\sigma}}_{eg}(t;\delta) = \frac{i}{\hbar}\left[\hat{H}_{int}, \hat{\sigma}_{eg}(t;\delta)\right] \tag{4.6}$$

$$= -ig\hat{\mathcal{E}}^{\dagger}e^{-i\Delta t}\left(\hat{\sigma}_{gg}(t;\delta) - \hat{\sigma}_{ee}(t;\delta)\right). \tag{4.7}$$

This leads to

$$\hat{\sigma}_{eg}(t;\delta) = -ig\int_0^t dt' e^{-i\Delta t'}\hat{\mathcal{E}}_s^{\dagger}(t')\left(\hat{\sigma}_{gg}(t';\delta) - \hat{\sigma}_{ee}(t';\delta)\right). \tag{4.8}$$

If the signal passes for a time interval τ_s signal bandwidth is given by $1/\tau_s$. Under the approximation of large detuning ($\Delta >> 1/\tau_s$) compared to signal bandwidth, for any signal field shape this integral can be evaluated approximately by first integrating over the fast varying part $e^{-i\Delta t'}$ then multiplying it by the final value of the rest of the slow varying part.

$$\hat{\sigma}_{eg}(t;\delta) = \frac{g}{\Delta}e^{-i\Delta t}\hat{\mathcal{E}}_s^{\dagger}(t)\left(\hat{\sigma}_{gg}(t;\delta) - \hat{\sigma}_{ee}(t;\delta)\right). \tag{4.9}$$

An effective Hamiltonian of the following form can be deduced from Eq. (4.3) using Eq. (4.9).

$$\hat{H}_{int}^{eff} = -\frac{\hbar g^2}{\Delta}\sum_{\delta} N(\delta)\left(\hat{\mathcal{E}}\hat{\mathcal{E}}^{\dagger} + \hat{\mathcal{E}}^{\dagger}\hat{\mathcal{E}}\right)\left(\hat{\sigma}_{gg}(t;\delta) - \hat{\sigma}_{ee}(t;\delta)\right). \tag{4.10}$$

Using the Heisenberg relation we can find the dynamics of the atomic polarization using the free evolution and the above effective interaction Hamiltonians;

$$\dot{\hat{\sigma}}_{eg}(z,t;\delta) = i\delta\hat{\sigma}_{eg}(z,t;\delta) + \frac{2ig^2}{\Delta}\left(\hat{\mathcal{E}}_s(z,t)\hat{\mathcal{E}}_s^{\dagger}(z,t) + H.c.\right)\hat{\sigma}_{eg}(z,t;\delta). \tag{4.11}$$

This can be used to calculate the phase shift on atoms due to the signal field.

$$\hat{\sigma}_{eg}(t = T_2;\delta) = e^{i\delta t}e^{i\hat{\Phi}}\hat{\sigma}_{eg}(t = T_1;\delta), \tag{4.12}$$

where,

$$\hat{\Phi} = \int_{T_1}^{T_2} dt' \frac{2g^2}{\Delta}\left(\hat{\mathcal{E}}\hat{\mathcal{E}}^{\dagger} + \hat{\mathcal{E}}^{\dagger}\hat{\mathcal{E}}\right) \tag{4.13}$$

Up to this point, we simply found the phase shift a signal will induce while passing off-resonant to an atomic ensemble in a cavity. The above consideration is fairly general in that it does not assume anything about the system. This treatment will be valid for atomic ensembles in a cold gas or a solid state system for a propagating signal or a cavity field. The difference between the propagating [33] (waveguide or free space) and the cavity case lies in the electric field operator $\hat{\mathcal{E}}$ that we need to put in Eq. (4.13) in order to find the phase shift. In our proposal, inside a cavity the electric field gets changed from the free space case due to the atom-cavity interaction which will play a pivotal role in our analysis. Here, we derive the cavity field $\hat{\mathcal{E}}$ based on its dynamics and the cavity input-output relation [113], where we introduce the input signal field $\hat{\mathcal{E}}_{in}$. The rate of change in cavity field $\hat{\mathcal{E}}$ is given by

$$\dot{\hat{\mathcal{E}}}(t) = -\kappa\hat{\mathcal{E}}(t) + \sqrt{2\kappa}\hat{\mathcal{E}}_{in}(t) + \frac{2ig^2}{\Delta}(\hat{\sigma}_{gg} - \hat{\sigma}_{ee})\hat{\mathcal{E}}(t). \tag{4.14}$$

A probe pulse, which is stored into the atomic memory, is in a many-photon coherent state with an average photon number N_p. We assume that the probe pulse is stored into a different ground state i.e. $\hat{\sigma}_{ee} = 0$. Hence, there are N_g number of atoms in the ground state $(\hat{\sigma}_{gg} - \hat{\sigma}_{ee}) = N_g$, resulting in

$$\dot{\hat{\mathcal{E}}}(t) = -\kappa\hat{\mathcal{E}}(t) + \sqrt{2\kappa}\hat{\mathcal{E}}_{in}(t) + \frac{2ig^2}{\Delta}N_g\hat{\mathcal{E}}(t). \tag{4.15}$$

Operating in the 'bad cavity' regime, where kappa is the cavity decay rate is faster than the effective single-photon coupling and the duration of the signal field, the cavity field dynamics in Eq. 4.15 is essentially given by the steady-state solution ($\dot{\hat{\mathcal{E}}}(t) = 0$) that leads to

$$\hat{\mathcal{E}}(t) = \frac{\sqrt{2\kappa}}{\kappa - \frac{2iN_g g^2}{\Delta}}\hat{\mathcal{E}}_{in}(t). \tag{4.16}$$

This enables us to find the phase shift per signal photon in the next step. Here, we consider a situation with a fixed number of atoms (N_g) in the ground state. The rather

complicated scenario of our proposal where the many photon probe pulse (in a coherent state) is stored into the atoms before the signal arrives is not considered yet. As we want to consider the phase shift due to a single input signal photon we have the normalization condition $\int_{T_1}^{T_2} dt' \left(\hat{\mathcal{E}_{in}}\hat{\mathcal{E}_{in}}^{\dagger} + \hat{\mathcal{E}_{in}}^{\dagger}\hat{\mathcal{E}_{in}}\right) = I$. Phase shift per signal photon to an atomic medium with exactly N_g atoms in the ground state can now be calculated by replacing $\hat{\mathcal{E}}$ in Eq. (4.13) using Eq. (4.16),

$$\Phi = \frac{4g^2/\kappa\Delta}{1 + (2N_g g^2/\kappa\Delta)^2}. \tag{4.17}$$

The term in the numerator, $4g^2/\kappa\Delta$, is the familiar dynamical stark shift enhanced by the cavity with decay rate κ. However, the phase Φ also has a term in denominator in this case, $(1+(2N_g g^2/\kappa\Delta)^2)$, which depends on the number of atoms in the ground state N_g. This term originated from the atom-cavity interaction. Note that in our protocol where a coherent probe pulse is stored in the atoms before the signal passes above them, N_g is not a constant. So, the phase Φ depends on N_g and hence number of photons stored, which is not a constant. Coherent states by definition are in superposition of different photon number states as $\sum c_n|n\rangle$. If we use a coherent state with average photon number $\langle n\rangle = N_p$, $c_n = \exp(\text{-}N_p/2)\frac{N_p^{n/2}}{\sqrt{n!}}$ while $|n\rangle$ denotes a n- photon Fock state. After the probe is absorbed in the atomic memory it will correspond to an atomic state of $\sum c_n|N-n\rangle|n\rangle$ (a spin-coherent state), where the first and second state correspond to number of atoms in the ground state $|g\rangle$ and spin-ground state $|s\rangle$. N denotes the total number of atoms participating in the atomic ensemble memory. Hence we can define this photon number specific phase shift based on the probe photon number

$$\phi_n = \frac{4g^2/\kappa\Delta}{1 + (2(N-n)g^2/\kappa\Delta)^2}. \tag{4.18}$$

The term in the denominator of the phase varies with the square of probe photon number. This phase shift dependence on the number of stored probe photons occurs due to the presence of the atoms in the cavity which effectively shifts the cavity resonance. Hence, the signal photon experiences a detuning from the cavity and only part of the signal can

enter the cavity leading to less phase shift of the atoms. This is reminiscent of the single atom conditional phase shift in a cavity [114]. Although, here we are dealing with many photon probe state and hence many atoms are contributing to shifting the cavity resonance according to the probe's photon number distribution. Note that although only parts of the signal enter the cavity this does not affect the signal efficiency or fidelity as we are using an one sided cavity. We discussed this issue in more detail in section 4.3.5.

The phase shift dependence on the number of stored probe photons can be compensated partially by making the cavity detuned from the input pulse. This will cancel the detuning that was coming as an off-set. For this we should detune the cavity by an amount $\frac{2ig^2}{\Delta}\langle\sigma_{gg}\rangle$ ($\langle\sigma_{ee}\rangle = 0$ as all the excited state atoms are transferred to the spin ground state). However even if this is incorporated, some residual dependence will still be present as a coherent probe pulse will have finite probabilities for different photon number states (Fock states) resulting in different amounts of phase shift based on the number of stored probe photons. Therefore, all these different phase contributions given by different Fock state components of a stored probe pulse cannot be all compensated simultaneously by detuning the signal. This residual phase shift dependence on the number of stored probe photons, due to the finite spread of the stored probe pulse in photon number states, will be important for our analysis. So, we attempt to understand this by analyzing what happens to the probe (or the atomic state generated by absorption of the probe) once the signal field has given it the phase shifts.

For our coherent probe pulse with average photon number $\langle n\rangle = N_p$ and a total of N atoms participating in the atomic ensemble memory, we have $\langle\sigma_{gg}\rangle = N - N_p$. This implies a necessary detuning of the signal from the cavity by an amount $\frac{2ig^2}{\Delta}(N - N_p)$. If the new input electric field is $\hat{\mathcal{E}}_{in1} = \hat{\mathcal{E}}_{in}e^{\frac{2ig^2t}{\Delta}(N-N_p)}$ and the corresponding new electric field in the cavity is given by $\hat{\mathcal{E}}_c$, where $\hat{\mathcal{E}}_c = \hat{\mathcal{E}}e^{\frac{2ig^2t}{\Delta}(N-N_p)}$, we will have

$$\dot{\hat{\mathcal{E}}}_c(t) = -\kappa\hat{\mathcal{E}}_c(t) + \sqrt{2\kappa}\hat{\mathcal{E}}_{in1}(t) + \frac{2ig^2}{\Delta}(\hat{\sigma}_{gg} - (N - N_p))\hat{\mathcal{E}}_c(t), \tag{4.19}$$

and hence a modified phase shift of

$$\phi_n = \frac{4g^2/\kappa\Delta}{1 + (2(N - n - (N - N_p))g^2/\kappa\Delta)^2} = \frac{4g^2/\kappa\Delta}{1 + (2(n - N_p)g^2/\kappa\Delta)^2}, \tag{4.20}$$

for a component of the probe pulse with n photons (i.e. in $|n\rangle$ state).

For the free space case in [33], ϕ_n was independent of $n \; \forall \; n$, say $\phi_n = \phi$. A coherent state given by $|\alpha\rangle = e^{-|\alpha|^2/2} \sum \frac{\alpha^n}{\sqrt{n}} |n\rangle$ will transform to $e^{-|\alpha|^2/2} \sum \frac{\alpha^n}{\sqrt{n}} e^{in\phi} |n\rangle = |\alpha e^{i\phi}\rangle$ under such a phase shift for all its number state components. So, it will just become a phase-shifted coherent state.

In the cavity case, instead ϕ_n depends on n. If the term in the denominator of ϕ_n - $(2(n - N_p)g^2/\kappa\Delta)^2$ is large (close to 1 or larger) then the coherent state does not have an exact phase shift anymore. Instead the coherent state gets a scattered phase shift as depicted in Fig. 4.2.

4.3.2 Husimi Q representation

The scattered nature of the phase shift is shown in Fig. 4.2, where a quasi-probability distribution of intial and final probe states are plotted in optical phase space using Husimi Q representation [115].

In Husimi Q-representation, the quasi-probability distribution (or Q-function) of an optical state with density matrix $\hat{\rho}$ at a point α in phase space (corresponding to the center of coherent state $|\alpha\rangle$) is given by

$$Q(\alpha) = \frac{1}{\pi} \langle \alpha | \hat{\rho} | \alpha \rangle \tag{4.21}$$

At a point in phase space, Q-function essentially calculates the overlap between the optical state and the coherent state centered on that point and hence is always positive. As we use pure states in our calculation for both the initial and final probe state, we will write

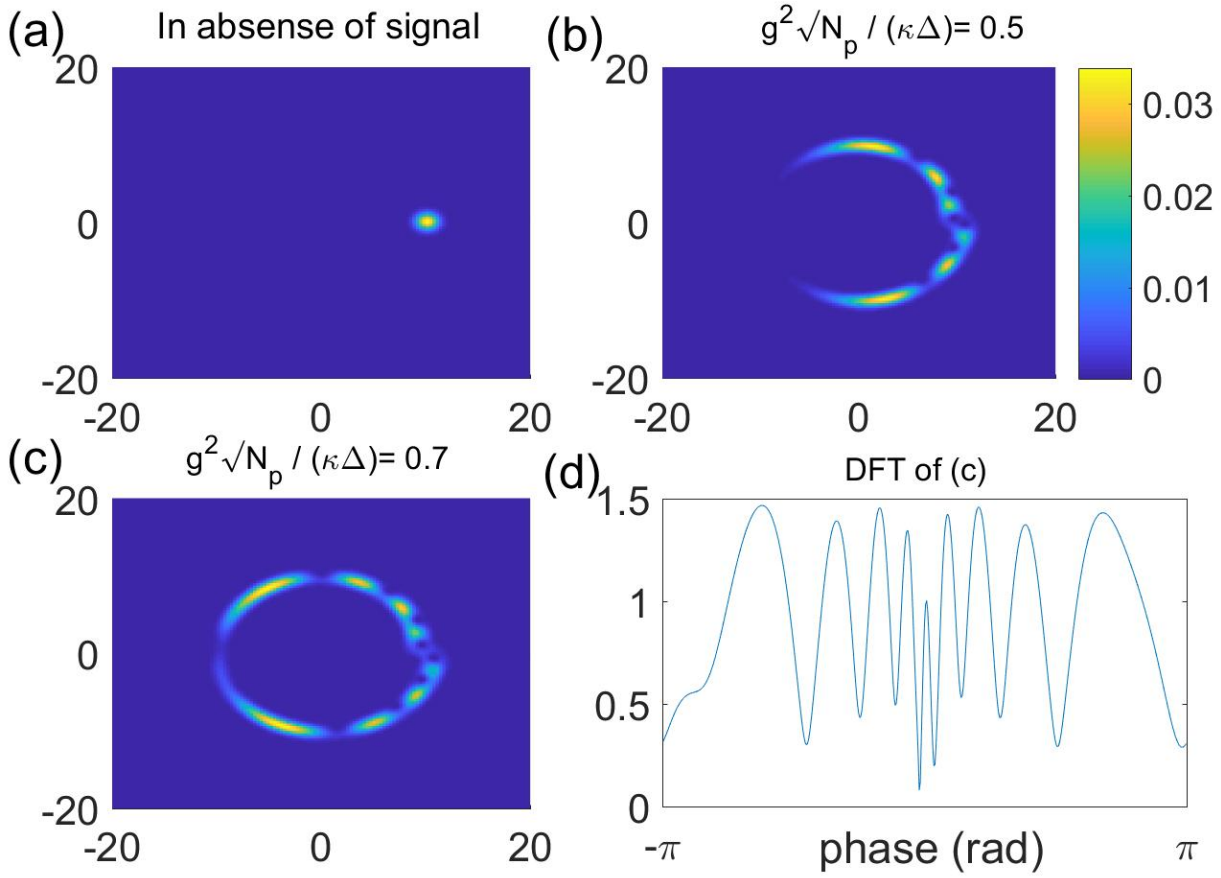

Figure 4.2: (color online) (a)-(c) Color plot of the Husimi Q function in the phase space for the probe states with and without signal photon. The color map is shown beside (b). For all the plots the initial probe pulse is in a coherent state with average photon number N_p = 100, and we assumed perfect storage and retrieval for simplicity. (a) Initial probe state. (b) Final probe state with parameters $g^2/\kappa\Delta = 0.5/\sqrt{N_p}$, showing that the state is slowly dispersing in phase. (c) Final probe state with parameters $g^2/\kappa\Delta = 0.7/\sqrt{N_p}$. Here the probe is completely dispersed in phase with very little probability left to be found in the location of the initial probe state. (d) A discrete Fourier transform(DFT) was done on probe state coefficients of (c). We plotted abs(DFT(c_n)) to show the distribution over phase. The Fourier transform shows the exact same pattern in different phases that we already saw in the Q function.

the density matrix $\hat{\rho} = |\psi\rangle\langle\psi|$ where $|\psi\rangle$ is the pure state.

In Fig. 4.2(a)-(c), Q-function is plotted for different states in the optical phase space, so the X and Y axes denotes the two conjugate optical quadratures. Fig. 4.2(a) shows the Q-function of initial probe state is peaked at x =10, y =0 for a coherent state with average photon number $N_p = 100$ and zero phase, i.e. $\alpha = 10$. In Fig. 4.2(b) Q-function for the final probe, for parameter values $g^2/\kappa\Delta = 0.5/\sqrt{N_p}$, is plotted. Here, the probe state is somewhat scattered with contribution from positive and negative phases while maintaining the same photon number. This shows through a few oscillations of the Q-function at the same radius from center. However, it is still not completely dispersed in phase as for these parameters the noise term $((2(n-N_p)g^2/\kappa\Delta)^2)$ in the denominator of ϕ_n in Eq. (4.20) is still not large enough. For $g^2/\kappa\Delta = 0.7/\sqrt{N_p}$ in Fig. 4.2(c) the probe is completely dispersed in phase and there is negligible overlap with the initial probe state. Hence, we can in principle distinguish the initial and final probe state almost perfectly implying a successful QND measurement. This will be investigated in more details below. In (d) a discrete Fourier transform (DFT) of the probe state is carried out, i.e. of the number state($|n\rangle$) co-efficients $c_n e^{in\phi_n}$ with c_n being initial coherent state co-efficients and ϕ_n given in Eq. (4.20). As the photon number is maintained the fourier transform should indicate the variation of the probe state in quadrature phase. The same oscillatory structure in phase, exactly as in (c), are observed in (d).

4.3.3 Inner product

For successful non-destructive detection of the signal in our scheme, one needs to distinguish between the initial and final probe state practically with high probability. However, before considering practical protocols feasible for implementation, it needs to be ensured that these two states has negligible overlap. The overlap between the two states can be quantified by an inner product distance measure. This gives the minimum theoretical error probability in distinguishing the two states. Hence, the two states cannot be distinguished with a smaller

error probability than |inner product|^2 using any protocol. This is a theoretical minimum.

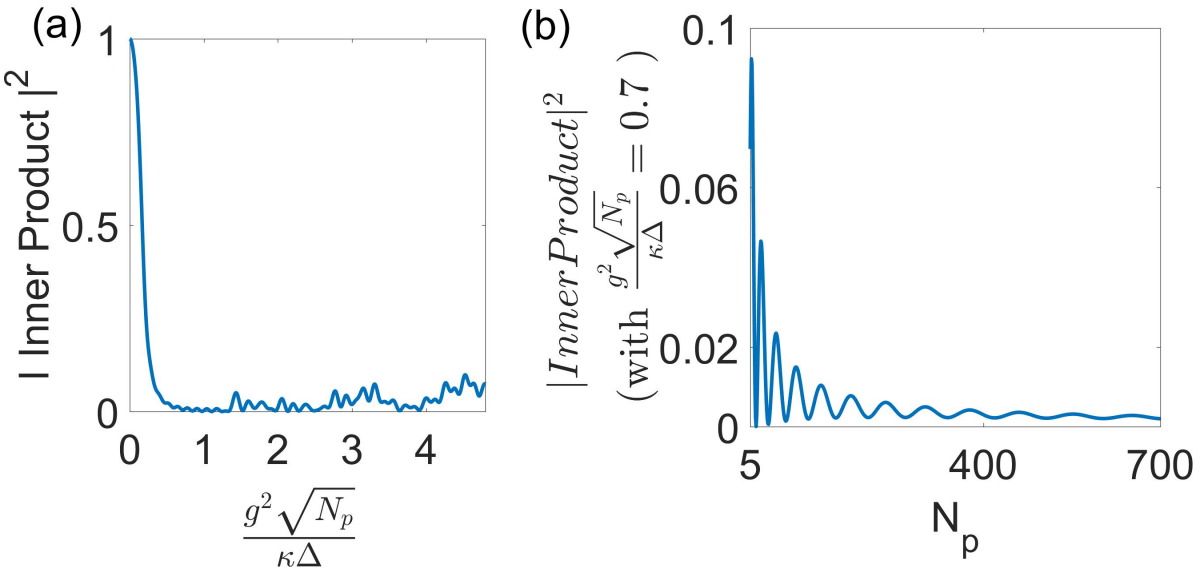

Figure 4.3: Overlap between initial and final probe states, quantified as the square of the magnitude of inner product between these two states, (a) as a function of $g^2/\kappa\Delta$ for N_p = 300 and (b) as a function of N_p for $g^2/\kappa\Delta = 0.7/\sqrt{N_p}$. Subfigure (a) shows that in a certain parameter regime from $g^2/\kappa\Delta \sim 0.7/\sqrt{N_p}$ to $g^2/\kappa\Delta \sim 1.4/\sqrt{N_p}$ the overlap almost vanishes. Hence initial and final state can in principle be distinguished almost perfectly in this range. In (b) we see that the overlap decays almost as $1/\sqrt{N_p}$ (disregarding the oscillations) as explained in text. The characteristic oscillations of the system, introduced by the phase shift dependence on the number of stored probe photons as seen in Fig. 4.2, are visible in the overlap as well.

The value of the |inner product|^2 changes as we change the value of $g^2\sqrt{N_p}/\kappa\Delta$. This is shown in Fig. 4.3 (a). The graph is plotted for values $N_p = 300$. We see that around the parameter regime from $g^2/\kappa\Delta \sim 0.7/\sqrt{N_p}$ to $g^2/\kappa\Delta \sim 1.4/\sqrt{N_p}$ there is almost no overlap between the two states. Hence here the two states can in principle be distinguished perfectly. The graph shows a lot of fluctuations as $g^2/\kappa\Delta$ comes also in the denominator of our phase term as noise. Hence, to make our protocol robust against small experimental parameter fluctuations we should choose our $g^2/\kappa\Delta$ value so that it has minimal fluctuations, like places close to $g^2/\kappa\Delta = 0.7/\sqrt{N_p}$.

This value is used in Fig. 4.3 (b) to show |inner product|^2 variation with N_p. We can easily see that the overlap between initial and final probe states goes proportional to $1/\sqrt{N_p}$.

The initial probe, being a coherent state will always have a spread of radius 1 in phase space. However the final probe state being spread all over the circle with photon number N_p (considering it almost uniformly for simplicity), almost like a band of width 1, will correspond to a total length of $2\pi\sqrt{N_p}$. Therefore, the effective overlap between the two will decreases as $1/\sqrt{N_p}$. However, this is a very crude argument. There are oscillations in |inner product|^2 with N_p (induced by the characteristic oscillations seen in Fig. 4.2), but the overall trend scales as $1/\sqrt{N_p}$.

4.3.4 Quadrature detection for practical discrimination

The initial and final probe state can be operationally discriminated through Homodyne detection. For that purpose the X quadrature is calculated for both of the states. In terms of photonic annihilation and creation operators $\hat{a}$ and $\hat{a}^\dagger$ as the X quadrature operator can be written as $\hat{X} = \hat{a} + \hat{a}^\dagger$. If eigenstates of $\hat{X}$ are represented as $|x\rangle$ then we know from the study of simple harmonic oscillators

$$|x\rangle = \sum_n \frac{H_n(x)}{(2^n n!)^{1/2}} \frac{e^{-x^2/2}}{\pi^{1/4}} |n\rangle \tag{4.22}$$

where $H_n(x)$ is a n^{th}-order Hermite polynomial evaluated at point x. To calculate the quadrature measurement probability density at a quadrature value of x for our probe in a particular quantum state $|\psi\rangle$ we calculated the value of $|\langle\psi|x\rangle|^2$.

For $g^2/\kappa\Delta = 0.7/\sqrt{N_p}$ and $N_p = 10$ the X quadrature detection probabilities are shown in Fig 4.4. Now, let us make a cut off (say, 1.64 in the above case) so that a the initial probe state has its X quadrature value higher than 1.64 with a high probability (99.9% in the above case). Now, whenever we get a X quadrature measurement of our probe below that we decide in favor of the final probe state and say that a single photon passed through in those cases. In this way, we will only be able to detect a signal with a certain success probability (e.g. 72% for N_p =10 as shown in Fig 4.4). However the probability that we make a false positive decision about the presence of signal while it is not there is very low,

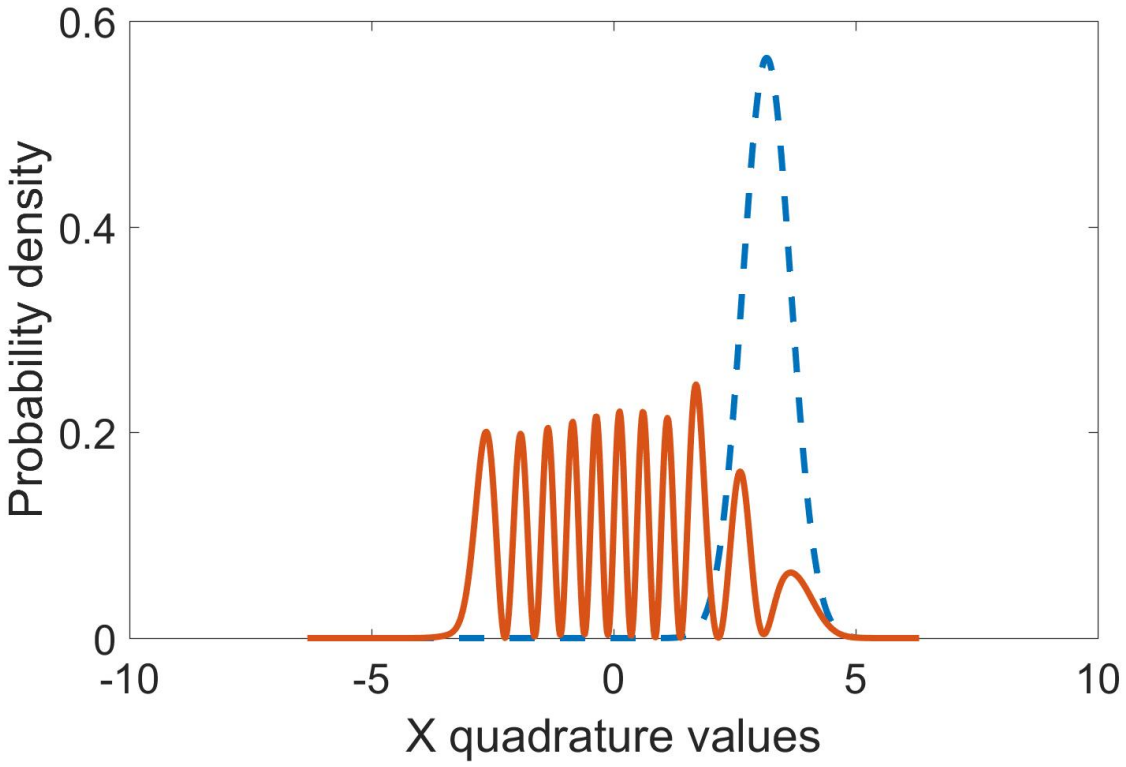

Figure 4.4: X Quadrature measurement probability density of probe states with (red solid line) and without (blue dashed line) a signal photon present for probe photon number $N_p = 10$ and $g^2/\kappa\Delta = 0.7/\sqrt{N_p}$.

only 0.1%.

If we allow 1% or 10% error rate in detecting false positives (which will correspond to initial probe state probabilities above the cut-off to be 99% and 90% respectively) we will get success probabilities of detections of 81% and 85% respectively.

The success rates corresponding to different probe photon numbers are presented in Table 4.1 for false positive detection (i.e. deciding there was a photon when there was none) probabilities of 0.1 % and 1 %.

Probe photon Number (N_p)	Success rate of detection for 0.1% error rate	Success rate of detection for 1% error rate
10	72.29%	81.46%
30	76.27%	83.62%
50	80.80%	86.31%

Table 4.1: The success rate of our single photon QND proposal is shown for different values of probe photon number (N_p) and for $g^2/\kappa\Delta = 0.7/\sqrt{N_p}$. The success rates are mentioned for two different false positive detection probabilities of 0.1 % and 1 %.

One thing to be noted here is that the |inner product|^2 between the probe states with and without a signal photon for N_p =10 was 0.0964. So, any type of measurement on the system with vanishing error rate can only give you a maximum of 90.36% success rate. For the small error rate of 0.1% we got 72.29% success rate for $N_p = 10$. For vanishing error rates, we couldn't get very close to the theoretical maximum as the X quadrature measurement was not providing the perfect discrimination, at least for small N_p.

The different values between the theoretical discrimination by inner product and in a practical approach like quadrature measurement originates from the fact that in a practical approach we always measure probability distribution (e.g. $|\langle\psi|x\rangle|^2$ for quadrature) and not the probability amplitude (i.e. $\langle\psi|x\rangle$). Hence, even if two states have vanishing inner product they can not be distinguished by quadrature detection completely as long as they overlap in quadrature values. However, this may not be an insurmountable difficulty. Other clever measurements schemes (e.g. invoking interference) may be constructed such that the states do not overlap in the corresponding observable. In such an ideal measurement scheme

crafted for two particular states the practically achievable discrimination should approach the theoretical minimum predicted by inner product.

On a more practical consideration, the values in Table 4.1 shows that success rate for the quadrature detection increases with increasing N. This is expected as the overlap, i.e. |inner product|^2, between the initial and final probe states decrease with increasing N as shown in Fig. 4.3(b) (except for the small characteristic oscillations). This is due to the fact that the final probe state gets spread over a larger radius in the phase space while the spread in the initial probe state remains constant in the phase space, as discussed in Section 4.3.3. So, for a much larger N we would be able to nearly perfectly distinguish the probe states in presence and absence of a signal photon even using the practical method of quadrature detection.

Motivated by the application of non-destructive detection of single-photon qubits in implementation of quantum networks [80], we focused on distinguishing a single-photon signal from vaccuum. However, for other potential applications in quantum nonlinear optics the physical parmaters of our scheme can be optimized to successfully discriminate between other Fock states of the signal field.

4.3.5 Signal Fidelity for Time-Bin Qubit Detection

In this section, we analyze the signal fidelity of the output signal from the cavity once the signal has imparted the necessary phase shift. As we discussed after Eq. (4.18), due to the phase shift dependence on the number of stored probe photons some parts of the signal gets detuned from cavity and does not impart phase shift to the atoms for all $|n\rangle$, where n is a particular Fock state component of the probe pulse. This remains even after phase compensation, performed by detuning the input signal, due to the residual phase shift. The detuned portion of the signal gets reflected and do not contribute to the phase shift. However, this does not reduce signal fidelity or efficiency as we use a single-sided cavity with a fast decay rate compared to signal bandwidth. As a single-sided cavity is used the input signal

reflected from front and the back mirror interferes and due to the fast cavity decay rate there is almost no time lag to form the output signal. We show this mathematically in the following. Using the input-output relation [113] for a one sided cavity, $\hat{\mathcal{E}}_{out}(t) = \sqrt{2\kappa}\hat{\mathcal{E}}_c(t) - \hat{\mathcal{E}}_{in}(t)$, we find from Eq. (4.19)

$$\hat{\mathcal{E}}_{out}(t) = \frac{\kappa + \frac{2i(N_p-n)g^2}{\Delta}}{\kappa - \frac{2i(N_p-n)g^2}{\Delta}}\hat{\mathcal{E}}_{in}(t). \tag{4.23}$$

So, the output signal field differs from the input field by only a global phase(θ) of magnitude $2\times\arg(\kappa + \frac{2i(N_p-n)g^2}{\Delta})$ or $\theta = 2\tan^{-1}(\frac{2(N_p-n)g^2}{\kappa\Delta})$. This implies $|\hat{\mathcal{E}}_{out}(t)|^2 = |\hat{\mathcal{E}}_{in}(t)|^2$ for all values of n.

If the signal photon is in a time-bin qubit then we need to maintain coherence between the early and late time bins. Note, although the $\mathcal{E}_{out}$ gets different phases for different values of n, this does not affect time-bin qubit state as both the early and late time bins pass over the same atomic ensemble at a small time difference. If the time lag between early and late qubit is T, the coherence needs to be maintained within this time interval implying $(N_p - n)$ needs to remain constant in that time interval. Here, n denotes a specific photon number state which is absorbed in the atoms and the corresponding atomic excitation are transferred to another ground state. Hence, n correspond to excitations in a second ground state, which may decay with time. If the rate of decay of the second ground state is γ_s then with time expectation value of n turns into $ne^{-\gamma_s T}$. If $\gamma_s T << 1$, then the change in n goes as $\Delta n = n(1 - e^{-\gamma_s T}) \approx n\gamma_s T$. Now, for small changes in n we can represent the change in magnitude of θ_n as $\Delta\theta_n$ where,

$$\Delta\theta_n = \frac{\frac{2g^2}{\kappa\Delta}}{1 + (\frac{2(N_p-n)g^2}{\kappa\Delta})^2}\Delta n = \frac{\frac{2g^2}{\kappa\Delta}}{1 + (\frac{2(N_p-n)g^2}{\kappa\Delta})^2} n\gamma_s T. \tag{4.24}$$

We include the the initial and final probe state discrimination condition of $\frac{g^2}{\kappa\Delta} \approx \frac{1}{\sqrt{N_p}}$ obtained from inner product analysis. The maximum value of $\Delta\theta_n$ is around $n = N_p$ or $(\Delta\theta)_{max} \approx 2\sqrt{N_p}\gamma_s T$ for $\gamma_s T << 1$. For $\Delta\theta = \pi$ the phase between two time bins flip and as the phases will be different for different values of n this will severely limit the signal

fidelity. Hence we will need to have $(\Delta\theta)_{max} << \pi$ for high fidelity signal output. Later in Section 4.5, we estimate $N_p = 6000$. So for a signal bandwidth of 1 MHz (i.e $T = 1$ μs) and a moderate spin ground state dephasing rate $\gamma_s = 0.34kHz$ at 5K temperature in Nd [116], we have $(\Delta\theta)_{max} \approx 0.0527 \approx \pi/60$.

Given the probe state and hence the stored atomic excitations are in a coherence state with coefficients of photon number state $|n\rangle$ given by $c_n = \exp(\text{-}N_p/2)\frac{N_p^{n/2}}{\sqrt{n!}}$, we have signal fidelity for time-bin qubit as $\sqrt{\sum_n |c_n|^2|\frac{1+e^{i\theta_n}}{2}|^2}$. For the above mentioned parameters, where we store the probe pulse in a second spin ground state with a long lifetime signal fidelity is 0.9999. Instead if the probe is stored in the excited state using a different protocol, e.g. atomic frequency comb quamtum memory protocol [101], we will have the decoherence rate as $\gamma_h = 100KHz$ for our doping as mentioned in Section 4.5. In that case, with a 1 MHz bandwidth signal the fidelity drops to 0.6915 but using a 10 MHz bandwidth signal we will acquire a fidelity of 0.9216.

4.4 Signal loss

In order to analyze off-resonant absorption loss for a cavity-enhanced signal we use the total Hamiltonian in Eq. (4.1). This results in

$$\dot{\hat{\sigma}}_{eg}(t;\delta) = (-\gamma + i\delta)\hat{\sigma}_{eg}(t;\delta) - ig\hat{\mathcal{E}}^{\dagger}e^{-i\Delta t}(\hat{\sigma}_{gg}(t;\delta) - \hat{\sigma}_{ee}(t;\delta)) \tag{4.25}$$

The dynamics of the cavity field and the cavity input-output relation is given by

$$\dot{\hat{\mathcal{E}}}(t) = -\kappa\hat{\mathcal{E}} + \sqrt{2\kappa}\hat{\mathcal{E}}_{in}(t) + ige^{-i\Delta t}\sum_{\delta} N(\delta)\hat{\sigma}_{ge}(t;\delta) \tag{4.26}$$

$$\hat{\mathcal{E}}_{out}(t) = \sqrt{2\kappa}\hat{\mathcal{E}}(t) - \hat{\mathcal{E}}_{in}(t). \tag{4.27}$$

Given that the single excitation wavefunctions are governed by the same equations, we can find the steady state solution to these equations by taking the Fourier transform of Eqs. (4.25)

and (4.26). Taking the Fourier transform of Eq. (4.25) gives,

$$\tilde{\sigma}_{eg}(\omega;\delta) = \frac{-ig}{i(\omega-\delta)+\gamma}\tilde{\mathcal{E}}^*(\omega-\Delta). \tag{4.28}$$

Using this result, and assuming that $\Delta \gg \delta \ \forall\delta$ i.e. Δ is larger than the inhomogeneous linewidth of the atoms considered, we can simplify the resulting expression for the cavity field to

$$\tilde{\mathcal{E}}(\omega) = \frac{\sqrt{2\kappa}}{i\omega+\kappa+\frac{ig^2N}{\omega-\Delta+i\gamma}}\tilde{\mathcal{E}}_{in}(\omega). \tag{4.29}$$

Using this result and the cavity input-output relation we can find the cavity output field. For the case where the signal bandwidth is smaller than the signal-atom detuning Δ, we can assume that the loss will be uniform and therefore analyze the cavity output field at $\omega = 0$. This is given by,

$$\tilde{\mathcal{E}}_{out}(\omega=0) = \left(\frac{2\kappa}{\kappa-\frac{ig^2N}{\Delta-i\gamma}}-1\right)\tilde{\mathcal{E}}_{in}(0). \tag{4.30}$$

In order to estimate the loss, we find the output intensity with respect to the input field intensity.

$$|\tilde{\mathcal{E}}_{out}(0)|^2 = \alpha|\tilde{\mathcal{E}}_{in}(0)|^2 \tag{4.31}$$
$$\alpha = \left(1-\frac{4\gamma g^2N}{\kappa\Delta^2}+(\frac{2\gamma g^2N}{\kappa\Delta^2})^2+(\frac{2g^2N}{\kappa\Delta})^2+\mathcal{O}(1/\kappa^3)\right).$$

Given that we assume κ to be the fastest rate in the system the main contribution to loss is given by

$$\zeta = \frac{4\gamma g^2N}{\kappa\Delta^2}. \tag{4.32}$$

However, the atoms are also within the cavity. If they are not completely off-resonant, spontaneous emission is enhanced by the Purcell factor $\frac{3Q}{4\pi^2}\frac{(\lambda_0/n)^3}{V}\frac{(\kappa/2)^2}{(\kappa/2)^2+\Delta^2}$. Considering this possible enhancement effect on spontaneous emission, the formula for the signal loss in cavity, i.e. Eq. (4.32), becomes - $\frac{4\gamma_r g^2N}{\kappa\Delta^2}\frac{3Q}{4\pi^2}\frac{(\lambda_0/n)^3}{V}\frac{(\kappa/2)^2}{(\kappa/2)^2+\Delta^2}$. Note that now homogenous linewidth, γ

is replaced by radiative linewidth γ_r. This is because cavity enhances the radiative linewidth γ_r to $\gamma_r \frac{3Q}{4\pi^2} \frac{(\lambda_0/n)^3}{V} \frac{(\kappa/2)^2}{(\kappa/2)^2+\Delta^2}$ and in case of a large enhancement that becomes the major contributing factor in the homogenous linewidth and hence in the resulting dephasing.

In the phase shift analysis we saw that $\frac{g^2}{\kappa\Delta} \sim \frac{1}{\sqrt{\eta_r N}}$ entails faithful discrimination of the probe pulse, where η_r is the probe retrieval efficiency and N is the number of atoms excited by the probe. Based on the definition of spontaneous emission rate in a solid where dipoles are oriented in one direction $\gamma_r = \frac{\mu_{eg}^2 k_s^3}{\pi\epsilon_0\hbar}$ and single photon coupling $g = \mu_{eg}\sqrt{\frac{\omega_s}{2\hbar\epsilon_0 V}}$, we find that $\frac{g^2}{\kappa\Delta} = \frac{1}{4\pi}\frac{\lambda_0^2}{n^2 A}\frac{F\gamma_r}{\Delta}$. Here F is the finesse of the cavity and it is related to the cavity quality factor as $\mathrm{Q} = F\frac{2L}{\lambda_0/n}$. Combining these formulas we find the cavity enhanced loss

$$\frac{4\gamma_r g^2 N}{\kappa\Delta^2}\frac{3Q}{4\pi^2}\frac{(\lambda_0/n)^3}{V}\frac{(\kappa/2)^2}{(\kappa/2)^2+\Delta^2} = \frac{6}{\pi\eta_r}\frac{(\kappa/2)^2}{(\kappa/2)^2+\Delta^2}. \tag{4.33}$$

Considering ideal retrieval $\eta_r \sim 1$, we find the expression for loss to be - $\frac{2}{\eta_r}\frac{(\kappa/2)^2}{(\kappa/2)^2+\Delta^2}$. Hence the only way to have low loss is having a high value of Δ compared to $\kappa/2$. For $\Delta = 3(\kappa/2)$ we have around 20% loss, while $\Delta = 3\kappa$ amounts to only 5.4% loss. Until now we have considered the ideal case with $\eta_r = 1$, but for practical purposes that may not be achievable. However an $\eta_r = 0.4$ may well be achievable as that amounts to a total memory efficiency of 16% only (considering storage and retrieval efficiency to be identical). That will not make a huge change in the corresponding values of Δ for similar loss probabilities. Δ values will only need to be multiplied by a factor of approximately $\sqrt{(}1/0.4) \sim 1.6$, i.e. $\Delta = 2.4\kappa$ and $\Delta = 4.8\kappa$ for 20% and 5.4% loss rates respectively when $\eta_r = 0.4$.

4.5 Implementation

Implementation of the proposal in rare earth ion-doped crystals has three stages - storing the probe, imparting a significant phase shift by single photon level signal and finally measuring the retrieved probe to know the presence of the signal. We already discussed about the probe storage in Section 4.2. There, we mentioned the necessity of dynamically detuning the cavity

to facilitate storage. We will return to this in more detail later in this section. Almost all of this section is dedicated to the next stage which is estimating the imparted phase shift to the probe. This is because much of the requirements for a proposed system are decided based on this stage. In the final stage, the probe pulse needs to be measured to distinguish between the probe states with and without the signal. In Section 4.3.4 we suggested to perform a quadrature detection for this purpose by means of homodyne detection, which is a standard optical measurement scheme.

4.5.1 Proposed parameter regime

The principal requirements for implementation of our proposed scheme are dictated by the ability to impart a large enough phase shift. Hence, we shall first return to the phase shift requirements for our proposal. The inner product analysis in Section 4.3.3 of our theoretical model shows $g^2/\kappa\Delta \approx 1/\sqrt{\eta_r N_p}$ needs to be satisfied to distinguish between the probe states with and without a signal photon. This can be re-arranged to write it in terms of the factor $f = \frac{g^2}{\kappa\Delta}\sqrt{\eta_r N_p} \approx 1$. By considering single photon coupling $g = \mu_{eg}\sqrt{\frac{\omega_s}{2\hbar\epsilon_0 V}}$ and radiative transition rate $\gamma_r = \frac{\mu_{eg}^2 k_s^3}{3\pi\epsilon_0\hbar}$ this condition is equivalent to $f = \frac{1}{4\pi}\frac{\lambda_0^2}{n^2 A}\frac{F\gamma_r}{\Delta}\sqrt{\eta_r N_p} \approx 1$, where n is the refractive index inside cavity and F is the finesse. Considering N atoms inside the cavity mode-volume V, we have $N_p \propto N \propto V$. Hence, we conclude that $f \propto \frac{\gamma_r}{\Delta}F\sqrt{\frac{L}{A}}$; note that it depends linearly on the finesse, but only on the square root of the length.

This analysis shows that the implementation of the proposal in rare earth ion doped ensemble demands a high finesse, small transverse area and preferably long cavity. Nanophotonic rare-earth ion coupled cavities are being fabricated in photonic crystal cavities etched inside rare-earth ion doped crystals [109, 110, 89, 90], in silicon photonic crystal cavity evanescently coupled to rare-earth ions [91] or in fiber tip microcavities containg rare-earth ion doped nanocrystals [92].

The rare-earth ion, which will be doped in such a cavity to interact with the photon, will require a large dipole moment for higher atom-photon coupling (higher g and so γ_r) to

increase the phase shift. For our estimates we have chosen neodymium (Nd^3+ in Nd:YVO) as it is one of the rare earth elements with a higher dipole and high optical coherence time [117, 118]. Optical coherence time is important as we are going to use AFC quantum memory protocol for probe storage in the excited state. We shall be using the Z_1 to Y_1 levels in Nd^{3+}:$^4I_{9/2} \rightarrow {}^4F_{3/2}$ transition at 879 nm (see Fig. 1 of [117]). This levels in Nd:YVO are particularly useful as each of these Z_1 and Y_1 levels (Krammers doublet) split into two levels creating a four level system with favorable selection rules under an applied magnetic field along the YVO crystal axis [117]. The selection rules are such that light polarized along the crystal axis (or perpendicular to it) interacts only with each set of sub-levels and there is no cross-talk between them (or vice-versa). This effectively creates convenient Λ systems inside the four level system. In [117] it is experimentally shown that the branching ratio between the direct and cross-transitions is 95%-5%, which is quite close to a perfect selection rule. In our proposal both the probe and signal will be polarized along the crystal axis and interact with only one sub-level, as both light and the cavity will be far detuned from the other sub-level. The two sub levels will be far detuned by a large applied magnetic field. Although, both signal and probe only interact with one sub-level we will still use the Λ system for optical pumping to prepare the AFC quantum memory for probe storage.

The only experimentally free parameter in the phase shift formula (and hence in f) is Δ which can be decreased to increase the phase shift. However, Δ is constrained by signal loss. As shown in Section 4.4, signal photon loss on resonance with a cavity with high quality factor is given by $\frac{2}{\eta_r}\frac{(\kappa/2)^2}{(\kappa/2)^2+\Delta^2}$ where the cavity enhanced spontaneous emission dominates the decoherence process. Hence, a large detuning compared to cavity linewidth (around $\Delta > 3\kappa$) is necessary for low loss.

We are now using the AFC storage protocol in Nd:YVO photonic crystal cavities [88] as an example to provide an estimate for implementation of the scheme. The main condition for successful implementation is to reach the phase shift condition $g^2/\kappa\Delta \sim 1/\sqrt{\eta_r N_p}$ while simultaneously having $\Delta \geq 3\kappa$ to keep the loss low. Here, we propose one set of parameters

to reach the desired regime - $g = 2\pi\times$ 8 MHz, $\kappa = 2\pi\times$ 30 MHz, $\Delta = 2\pi\times$ 100 MHz, $\eta_r = 0.5$ and $N_p = 6000$. This yields $f = \frac{g^2}{\kappa\Delta}\sqrt{\eta_r N_p} = 1.16$ which is around 1 and hence sufficient for a successful QND detection of a single photon. The corresponding value for loss is $\frac{2}{\eta_r}\frac{(\kappa/2)^2}{(\kappa/2)^2+\Delta^2} = 0.073$ or 7.3%. For $N_p = 6000$ the probability to distinguish between the probe states with and without a signal photon present by an X quadrature measurement is very high. The probe state that interacted with signal is scattered all over a circle in phase space with a radius of around 77 ($\sim \sqrt{6000}$), while the probe state without the signal is a coherent state, which is highly localized. Based on this, we estimate the probability of overlap between the X quadrature distributions of the two states to be less than 4%. Hence, we can distinguish between the two states with very low error rates with a success probability of over 96%. Incorporating the effect of the 7.3% loss this would produce around 89% success probability in total.

Nanophotonic cavities built in Nd:YVO have already achieved experimental quality factors around 20,000 [110] which corresponds to a cavity linewidth $\kappa = 2\pi\times 17$ GHz. Achieving $\kappa = 2\pi\times 30$ MHz will probably require a combination of increasing the finesse and the length of the cavity. This may be realistic given the steady and fast recent progress in building high quality factor photonic crystal cavities [90, 91, 92]. For the Nd:YVO system Ref. [110] suggests that it may be possible to improve the finesse by an order of magnitude or more by changes in the fabrication process such as decreasing the sidewall angle for the nanocavities and post-fabrication annealing. Increasing the length of the cavity should also be possible, but will require longer milling times (for ion-beam based fabrication). Having sufficiently many ions in the cavity to be able to store $N_p = 6000$ photons as suggested above probably requires an increase in the cavity length by at least an order of magnitude, taking into account the fact that the AFC memory protocol requires spectral tailoring, which reduces the available number of atoms. Another attractive way to increase the number of atoms would be to use recently developed stoichiometric rare-earth crystals [111, 112] where ultranarrow inhomogenous linewidth has been observed. However, currently these crystals

are made only from weak dipole elements like Eu^{3+} which is not good for our proposal. A nanocavity etched in a stoichiometric crystal, made of an rare-earth element with a strong dipole element, would definitely be useful as many more atoms can be accommodated inside the cavity.

The other approach towards ensemble QND measurements can be increasing atom-cavity coupling or g value [90]. One way towards this is by decreasing cavity mode volume through incorporation of dielectric discontinuities [119] into cavity design. However, the number of available atoms for phase shift also decrease with decreasing cavity mode volume as reflected in $f \propto F\sqrt{\frac{L}{A}}$. So, for the purpose of ensemble QND only decreasing the cavity transverse area will help while decreasing cavity length to decrease mode volume will adversely affect the ensemble QND detection. Another strategy to increase the coupling factor may be to change the AC stark shift interaction to higher dipole 4f $\leftrightarrow$ 5d transition while storing the probe using the 4f $\leftrightarrow$ 4f transition which has desireable optical and spin coherence properties. However, this will need a doubly resonant cavity [90].

Recently, there has also been development of other attractive nanocavity systems with rare-earth ions incorporated into them [91, 92]. In [91] a Si-photonic crystal cavity was manufactured through which light is evanescently coupled to a single Er^{3+} ion, present inside a lightly doped Er:YSO crystal. This is an attractive system with cavity quality factor of 51,000 for the Er^{3+} transition at 1.5 μm wavelength. This led to the coupling of individual Er^{3+} ions to the cavity. Similar system can probably be constructed for higher dipole moment rare earth ions like Nd^{3+} but the rare earth ions are evanescently coupled here which decreases the cavity coupling g and Purcell factor compared to what will have been possible if they were present inside the cavity. The evanescent coupling also decreases the number of atoms that can be coupled to the cavity.

Another system containing a Eu^{3+} doped nanocrystal inside a free-space cavity between a fiber tip and a mirror is introduced recently [92]. This also have attractive cavity parameters of finesse 17,000, $\kappa = 1.3$ GHz and a corresponding cavity quality factor of around 400,000.

The much higher finesse and quality factor of the cavity paves the way for implementing our proposal. However, this design uses a nanocrystal of dimensions 40-60 nm. Hence, not a lot ions can be accommodated inside the crystal, at least inside a reasonable frequency range of 100 MHz-2 GHz which may impose some limitations. A short frequency range is required so that the detuning (Δ) doesn't need to be too large.

4.5.2 Dynamical switching of the cavity

After the probe storage we need to detune the cavity by $\Delta \sim 100$ MHz for it to be on resonance with the signal and later detune it back to retrieve the probe. The cavity is initially in resonance with the atoms at $\nu \sim 340$ THz frequency. If the original cavity length is L and the change in length needed to detune the cavity by an amount Δ (in frequncy) is ΔL then $\frac{\Delta L}{L} = \frac{\Delta}{\nu} \sim 3 \times 10^{-7}$. Considering the above strain and the Young's modulus of the YVO crystal = 133 GPa [120], we can calculate the necessary stress to be 44 kPa. Here, we are taking a commercial piezo detector as an example, P-882.1 in [121]. This has a 6 mm^2 surface area. Hence, 44 kPa stress will correspond to a applied force of 0.26 N. Piezo can in general deliver far higher magnitude maximum forces, denoted as block forces than this [122, 121]. In this specific case of [121], the piezo actuator has a block force of 190 N corresponding to a maximum displacement of 8 μm . Hence the force necessary in our case is only about 0.14 % of the maximum force. For applying such a small force resolution becomes important. Piezos also generally have sub-nanometer resolution in precise positioning [121]. For the maximum displacement of 8 μm block force is 190 N [121] and for sub-nanometer resolution the minimum force produced will be at most 0.023 N. We need a force of 0.26 N hence this gives us at most a 10.8 % error or about 11 MHz error in positioning the 30 MHz cavity. This can affect our phase shift to some amount. This commercial piezo actuator [121] has microsecond response times which is around the AFC storage times. Also there has been a lot of ongoing research on sub-microsecond piezo [123].

The other issue with the strain given by piezo is that this deforms the crystal structure

which causes a small stark shift between Nd levels. To the best of our knowledge, there is no experimental data in the literature on the strain (or equivalently stress) induced stark shift of Nd:YVO. However, experiments have been performed on other crystals like Nd:$YAlO_3$ [124]. In Nd:$YAlO_3$ the magnitude of stress induced shift in Z_1 to Y_1 transition in Nd^{3+}:$^4I_{9/2} \rightarrow {}^4F_{3/2}$ levels is found to be around 32.05 Hz/Pa (using Eq. (2b) in [124]). This will imply 1.41 MHz of stress induced shift to our desired transition. This is small compared to our required detuning of 100 MHz. For an approximately linear rise of the piezo actuator over 50 ns time this will give a phase shift to the probe of magnitude about $2\pi\times0.035$ rad. But, this shift will not affect our proposal adversely as this phase shift will be present independent of the presence of the signal. However, an unpredictable error in the piezo displacement will affect the proposal. This is because the probe will be unpredictably phase shifted and hence on making a quadrature measurement there will be some probability for false positive result. So, for a 5% error in piezo displacement this will result in a phase shift of $2\pi\times0.035$. Our proposal has a similar quantity like phase shift $g^2/\kappa\Delta \sim 1/\sqrt{6000} = 0.012$, and hence naively, there should be about 30% error. But, the probe will not be scattered over the phase space due to this phase shift as it occurs due to the Stark shift in the atoms and has nothing to do with the presence of the cavity. Hence, the probability of false positive detection will be very low even for a phase shift comparable to the $2\pi\times$ 0.012 rad value as due to the cavity in presence of a signal final probe state quadrature gets scattered all over the phase space, i.e. in a 2π rad angle. So, this strain induced stark shift will only decrease the success probability by a very small amount. If we consider that the final probe states spreads uniformly this will correspond to roughly $0.012/1 \approx 1\%$ less success probability.

Another attractive approach toward achieving the dynamical detuning is to detune the atoms, instead of the cavity, by Zeeman effect using an external magnetic field. A magnetic field is already present to enforce the selection rules. The magnitude of this magnetic field needs to be increased to give an extra 100 MHz detuning between the atoms quickly. Similar to the piezo strain induced shift, in the Zeeman shift process the dynamical fluctuations

while detuning the atoms will affect the phase shift.

4.5.3 Combining Cavity and Multipass Approach

Another avenue towards implementation can be combining the cavity approach with the multipass approach described in [33]. In the multipass approach instead of using a cavity the signal is simply passed multiple times through the crystal (in a waveguide) using an optical switch. However, multipass arrangement alone can not achieve single photon QND as it will require a lot of passes (> 200) [33] which is currently not feasible as the optical switches, essential for the multipass arrangement, cause far too much switching loss for so many passes. However, if we combine the multipass arrangement with the cavity then we may be able to restrict ourselves with much fewer passes. The principle advantage of this scheme is that loss can be decreased significantly without having a large detuning, which will improve the phase shift considerably.

In the multipass arrangement as the photon passes over the atoms multiple(say m) times both the phase shift and loss gets multiplied by m [33]. i.e. phase $= m\frac{g^2}{\kappa\Delta} \sim \frac{1}{\sqrt{\eta_r N}}$ and loss $= m\frac{4\gamma_r g^2 N}{\kappa\Delta^2}\frac{3Q}{4\pi^2}\frac{(\lambda_0/n)^3}{V}\frac{(\kappa/2)^2}{(\kappa/2)^2+\Delta^2}$ But, loss is proportional to $(\frac{g^2}{\kappa\Delta})^2$.Considering $m\frac{g^2}{\kappa\Delta} \sim \frac{1}{\sqrt{\eta_r N}}$ we eventually end up with loss decreased by a factor of m, i.e. $\frac{6}{m\pi\eta_r}\frac{(\kappa/2)^2}{(\kappa/2)^2+\Delta^2}$. Now even with $\frac{(\kappa/2)^2}{(\kappa/2)^2+\Delta^2} \sim 1$ we can achieve low loss simply by having a moderate value of m. For $\eta_r \sim 1$ and $m = 10$ we will have 20% loss, while having last factor as close to 1 as possible. Hence, we can have low loss with as small a detuning as the AC stark shift approximation allows us to. Also the phase shift is multiplied by m. So, now it will be much easier to achieve the new phase shift condition $m\frac{g^2}{\kappa\Delta} \sim \frac{1}{\sqrt{\eta_r N}}$ for much more moderate values of g, κ and N, especially with a small value of Δ allowed. This will also mean that now both the signal and the atoms are in resonance with the cavity. So, there will also be no need for dynamically detuning the cavity using piezo or other techniques. However, there are also going to be extra losses from the optical switches used in the multipass and espcially due to the mode matching of the cavity with the optical fiber. The main hurdle for this scheme is that cavity mode-matching

is quite bad for most optical systems right now. In the nano-cavities of [88], the optimal coupling transmission achieved right now is 27%. The multipass-cavity combination will only be useful if this value can be improved significantly (to 95% or higher).

4.6 Conclusion

In summary, we performed a detailed theoretical analysis for a cavity-enhanced non-destructive photonic qubit detector using an atomic ensemble and determined the necessary parameters for implementation of the scheme in an ensemble of rare-earth ions doped in a crystal. A single-pass configuration such as in the proof-of-principle experiment of Ref. [33] is unable to reach single-photon level sensitivity due to a tradeoff between phase shift and loss. This can be overcome by using a cavity. We showed that the presence of the cavity also introduces a significant complication because the phase shift acquires a dependence on the probe photon number, in addition to the desired dependence on the signal photon number. We analyzed this effect in detail to determine the final probe state, using the Husimi Q-representation in phase space and calculating the quadrature distributions, which allowed us to determine the success probability and error rate of the scheme as a function of various parameter values. We modeled the cavity-enhanced loss and estimated system parameters for Nd:YVO nanocavities as an example system toward implementation. For a successful implementation of the scheme a small transverse area, high finesse and relatively long cavity are needed. Although these values have not been achieved in current systems yet, we think that they are within reach, given the recent rapid progress in coupling rare-earth ions to optical cavities. We thus hope that the present work will prepare the ground for the experimental realization of non-destructive photonic qubit detection in the not too distant future.

4.7 Acknowledgments

The authors acknowledge useful discussions with W.Tittel, C.Thiel, P.Barclay, T.Zhong, A.Faraon, N.Sinclair, N.Lauk, R.Ahlefeldt and S.Wein. SG acknowledges support through a Dean's International Doctoral Recruitment Scholarship of the University of Calgary, an Alberta Innovates Technology Futures (AITF) Graduate Student Scholarship (GSS) and an Izaak Walton Killam Doctoral Scholarship. CS acknowledges support from the Natural Sciences and Engineering Research Council of Canada (NSERC).

Chapter 5

Rydberg Excitons

5.1 Introduction

Rydberg systems are systems which behave like the hydrogen atom excited to a large principal quantum number n. The most famous of the Rydberg systems are Rydberg atoms [125, 126] which are atoms excited to a high n ($n \sim 100$) state. Rydberg atoms are hydrogen-like as their core (i.e., the tightly held inner electrons and the nucleus together) effectively behaves as a single positive charge. Due to the very high n values Rydberg atoms have large extensions ($\sim 1\mu m$ for $n = 100$) which gives rise to large interaction effects between atoms excited to Rydberg states. The interaction between Rydberg states is so enormous that the excitation of one Rydberg state prohibits the excitation of another in its vicinity, called Rydberg blockade effect [125]. The large interaction strength is also switchable as the ground state has 12 orders of magnitude smaller interaction strength than Rydberg states [127]. The high n states also have very long lifetimes [126]. These properties of Rydberg atoms have garnered a lot of attention and made them a very attractive system for applications in quantum information processing [127]. Rydberg atoms have also been successfully coupled to Bose-Einstein condensates [128].

More recently, Rydberg states were observed in excitons occurring in semiconductor sys-

tems. Excitons are electron-hole pairs occurring in semiconductor and hence they are hydrogen like objects seen in condensed matter system (even for low n states). Rydberg excitons were observed in several semiconductor system like Cu_2O [129] or monolayer WS_2,WSe_2, MoS_2 etc. [130, 131, 132]. We focus on the Cu_2O system and explore the properties of Rydberg exciton.

5.2 Discovery

Exciton energies are below the conduction band at the band gap between the valence band and conduction bands. Depending on the bands used there are four different exciton series in Cu_2O - blue, violet, yellow and green [133]. The yellow P exciton series was discovered first [129]. The band gap is around 2.17 eV for yellow P excitons. The energy of the excitons with principal quantum number n is given by –

$$E_n = E_g - R_y/(n - \delta_l)^2, \tag{5.1}$$

with band gap energy $E_g = 2.17$ eV, Rydberg energy $R_y = 92$ meV and quantum defect δ_l (e.g. $\delta_P = 0.23$) depending on the azimuthal quantum number l. The quantum defect is introduced to account for the deviation from hydrogen like behaviour. It is also seen in Rydberg atoms where it occurs due to penetration of high angular momentum (large l) states into the nucleus. The important difference between Rydberg atoms and excitons lies in the Rydberg energy R_y which is multiple orders of magnitude smaller for Rydberg excitons. This makes detecting high n states separately from the ionization continuum extremely difficult.

Excitons themselves were first observed in Cu_2O in the 1950s. Still the initial efforts only succeeded to see excitons up to around $n = 10$ due to the small Rydberg energy [134, 135]. Rydberg states in Cu_2O excitons were observed finally in 2014 [129] using high-resolution spectroscopy with a narrow linewidth laser ($\sim$ 5 neV). P excitons were excited directly using yellow optical light in a natural Cu_2O crystal, kept at cryogenic temperature of 1.2 K.

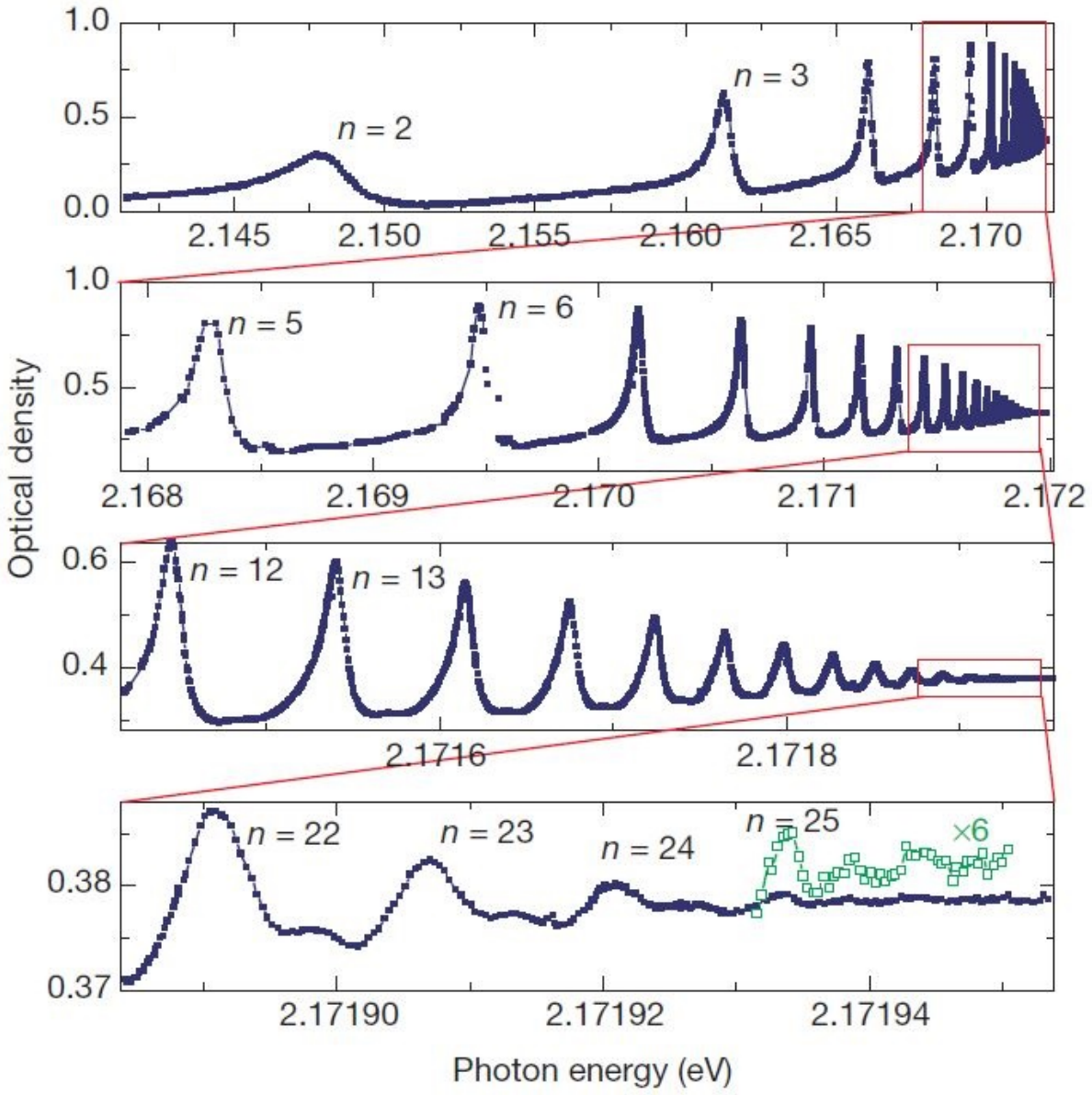

Figure 5.1: Absorption spectrum of different excited states of Cu_2O. Insets show the higher n (principal quantum number) states successively. States upto $n = 25$ are seen. High n states behave as Rydberg states. Reprinted with permission from [129].

The excitonic absorption spectrum at the different excitation energies is shown in Fig. 5.2. Zooming into the successive insets in Fig. 5.1 one can see that excitation up to $n = 24$-25 are observed. The linewidth of the absorption lines also gets successively narrower with higher n, as expected. Here, nP excitons are shown which can be directly excited using a single optical laser. Other exciton series like nS series can also be excited, although only using two lasers due to the exciton selection rules [136].

Excitons at $n = 25$ already have giant extensions. Similar to Rydberg atoms [126] the average radius of Rydberg excitons can be given by

$$\langle r_n \rangle = \frac{1}{2} a_B (3n^2 - l(l+1)) \tag{5.2}$$

where a_B is the Bohr radius, n and l are principal and azimuthal quantum numbers respectively. For $l = 1$, i.e. P excitons $a_B = 1.11$ nm [137]. Considering the above values and $n = 25$ the average exciton radius of $\langle r_n \rangle = 1.04\ \mu m$ is calculated. Hence, the extension (diameter) of P excitons at $n = 25$ is already larger than 2 μm, an extension only achieved for $n \sim$ hundred for Rydberg atoms. Due to this large extension even at small n values (compared to atoms) Cu_2O excitons are expected to behave like a Rydberg system.

The most characteristic fingerprint of a Rydberg system is the Rydberg blockade effect whereby one excitation to a Rydberg state prevents any other within a certain radius around it, called blockade radius R_b. Blockade is seen in multiple different ways in [129], as explained through Fig. 5.2. In Fig. 5.2 (a) Rydberg states are excited using one laser. As the laser power is increased absorption decreases most prominently for higher n states which is exactly what should be expected due to Rydberg blockade effect. The Rydberg interaction increases exponentially with higher n ($\sim n^{11}$) and hence only higher n states are the ones which show the blockade effect and are called Rydberg states. Due to blockade, there is suppression of excitation for high laser power and hence the fraction of the total light that is absorbed decreases. In Fig. 5.2(b) two lasers (pump and probe) are used. One laser (pump) is tuned

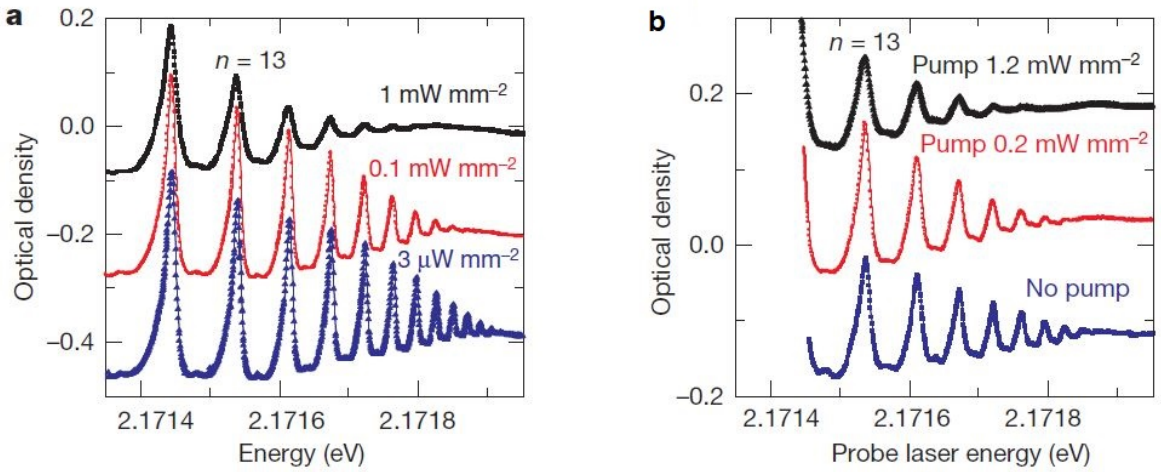

Figure 5.2: Signature of Rydberg blockade in Cu_2O excitons. (a) One laser experiment-when laser intensity is increased, absorption decreases rapidly for high n states showing suppression of excitation or Rydberg blockade effect for high n. (b) Two laser experiment with pump and probe lasers. The pump laser frequency is fixed at $n = 14$. Absorption due to probe laser decreases with increasing pump laser power showing asymmetric $(n - n')$ blockade effect. Reprinted with permission from [129].

in resonance to $n = 14$ state while the other laser (probe) is scanned over multiple state. As the pump laser energy is increased, the absorption due to the probe laser is observed to decrease. This shows the presence of strong Rydberg interaction between different states (i.e. $n - n'$ interaction or asymmetric interaction).

5.3 Properties

Since their discovery in 2014, many properties of Rydberg excitons in Cu_2O have been studied. Rydberg interaction coefficients between two excitons were modeled for the interaction Hamiltonian eigenstates [138]. Angular dependence of the interaction potential has been investigated too. The asymmetric Rydberg blockade effect (i.e., Rydberg interaction between $n - n'$ states) has been experimentally observed and modeled in significant detail [139] after its initial observation in [129].

The effect of magnetic field on Rydberg excitons was studied in [129] itself. An electron

- previously moving in a straight line - moves in a circle on entering a region of constant magnetic field perpendicularly. Hence, an electron already moving in a circle - like an electron around a hole in an exciton -would feel an extra centripetal force in a constant magnetic field. This would crudely explain why exciton wavefunction would get squeezed in magnetic field. Due to squeezing of wave function, Rydberg interaction and hence blockade radius would drastically decrease. This is observed in [129] where using no magnetic field showed almost complete excitation suppression in high laser power while a magnetic field of 0.8 T would get the wave function squeezed and excitation suppression at similar laser power is only around 50 %. Due to this squeezing effect, large n states gets visible in presence of magnetic field. States up to $n = 55$ were observed in [140]. Magnetic field also causes a rather complicated splitting and mixing of different states due to Zeeman effect. Using this mixing to one's advantage dark paraexciton states -which are not normally optically addressable - were observed. Paraexciton states get mixed with orthoexcitons (or the bright excitons) and they were detected by using magnetic field up to 10 T [141]. Similar splitting and mixing has been observed in Rydberg excitons in Cu_2O in presence of electric fields too [142].

All the above studies in Cu_2O excitons were performed in cryogenic temperatures, generally at $\sim$ 1-2 K. For practical applications in quantum technologies, high operation temperature would be desirable though. Properties of Cu_2O excitons above liquid nitrogen temperature ($\sim$ 80 K) were observed in [143]. States up to $n = 6$ for the yellow exciton series and up to $n = 4$ for the green exciton series were successfully observed.

The effects of mechanical strain on crystals and excitons are well known. This has been analysed for Cu_2O excitons too. It was shown by theoretical modelling that using cylindrical stresses excitons can be trapped or compelled to move along a waveguide [144].

Recently Cu_2O microstructures have been manufactured and their properties were studied [145]. Such microstructures may become crucial for applications of Cu_2O excitons in quantum technologies. A thin film of Cu was deposited over a layer of SiO_2 and Si by electron beam evaporation. Later the Cu layer undergoes vigorous oxidation to form the Cu_2O microcrystal

layer. Exciton states of to $n = 6$ were already observed. More states can potentially be observed with a larger microcrystal thickness [145].

5.4 Application

Rydberg excitons can potentially have applications in a diverse range of areas within quantum sciences and more specifically in quantum technologies like quantum computing, quantum networks, photonics, simulating quantum many body physics etc. One simple application can be creating a single photon source using the Rydberg blockade effect, as proposed in [146]. A Cu_2O microcrystal with size smaller than the blockade volume is needed. When excited by a pump laser only one exciton is excited in the microcrystal due to the blockade effect. The photon produced from the recombination of the exciton can be collected in a particular direction by embedding the microcrystal in a waveguide or an optical microcavity. Another application of Cu_2O Rydberg excitons was proposed whereby a maser can be produced using the Rydberg exciton. The Rydberg states can be used as metastable state to produce a CW maser in the THz frequency range [147].

Rydberg excitons in semiconductor microcavities are explored in [148] to create large optical nonlinearities. Optical and THz light is used to access a three-level system to derive nonlinear optical responses.

Quantum many body physics and phase transitions were studied in a model of Rydberg excitons as an one dimensional spin chain. Topological spin phases were predicted to occur [149]. Possible ways for their detection were analysed too [150]. These studies [150, 151] essentially simulated many-body phenomenons using Rydberg excitons. Our paper on Rydberg excitons [17] is also a proposal to simulate many-body dynamics (in particular Rydberg Dynamics) using the Rydberg exciton system.

Many different quantum systems, which includes the Rydberg atoms, have already been used to simulate quantum many body dynamics. Details of quantum simulation using dif-

ferent quantum systems is presented in the next chapter.

Rydberg excitons in Cu_2O were first discovered less than a decade ago. Hence, research in their potential application is only picking up pace now and it can be safely said the bulk of the possibilities remains to be discovered.

Chapter 6

Quantum Simulation

Quantum simulators are quantum systems whose parameters can be controlled experimentally to simulate the essential features of a much more complex real-world quantum system [152, 153]. Richard Feynman alluded to this possibility of simulating real-world quantum systems by using quantum systems itself in his now famous 1981 lecture – 'simulating physics with computers' [154]. The power of quantum information processing is based on the premise of being able to compute simultaneously on the exponentially increasing number of states with growing number of qubits N. Feynman pointed out that the number of coefficients needed to just write down the state of a N particle spin half system is 2^N. Just storing all these coefficients exceeds the capacity of a classical computer at around $N = 50$. Further one needs to perform addition, multiplication and other operations to calculate the dynamics of the quantum state of a N qubit system. This becomes practically challenging beyond 20-25 spins already, even with current advances in computation. As a solution to this problem Feynman proposed that another quantum system can instead be used to model the evolution [154]. This is shown in Fig. 6.1. A quantum simulator can simulate a quantum system of interest by preparing the simulator in the same initial state as that of the system, mimicking the evolution of the system and then measuring the final state of the simulator appropriately, to determine the corresponding quantity in the system. We focus on the evo-

lution part as it is the most challenging. Feynman imagined a quantum machine that would imitate any quantum system including the physical world. However, such a sophisticated machine would be extremely difficult to build. It would be on the same level of difficulty as building a quantum computer and hence constitutes a long-term goal for quantum simulation. An easier and near-term goal for quantum simulation is to use a specific simulator to model a particular system of interest. Hence there can be two kinds of simulator based on the method of mimicking system evolution - one specific for a particular system which is an analog simulator and another that will be work for any system called digital simulator [155].

6.1 Analog and Digital simulation

The evolution of the quantum system of interest can be modeled using an analog or digital system as shown in Fig. 6.2. An analog simulator would have the same kind of Hamiltonian evolution as the system of interest. However, this simulator would not simulate every part of the system as Feynman imagined by 'simulating reality', but only certain essential parts we are interested in. For example, in condensed matter system one is interested in certain quantities (like magnetisation, correlation functions up to a few orders etc.) which decide the phase diagram. If one is interested in a phase transition in a solid, simulating the many details of the solid would be quite irrelevant. Quantum simulators themselves should be more robust against errors than quantum computers as the properties in real quantum systems like different phases appear despite disorders in the system [152]. Analog quantum simulators are even more robust as they simulate the whole Hamiltonian directly instead of digital simulators which may gather error due to the multiple steps involved in digital simulation (explained later through Eq. 6.1 and Fig. 6.2) [152].

We now return to Feynman's original conjecture of building a 'universal quantum simulator' that can simulate any quantum system [154]. It was proven by Seth Lloyd in 1996 that such a universal quantum simulator can be constructed [156]. The Hamiltonian cor-

responding to the quantum system of interest H_{sys} can be assumed to be built out of few particle interactions (i.e., local interactions).

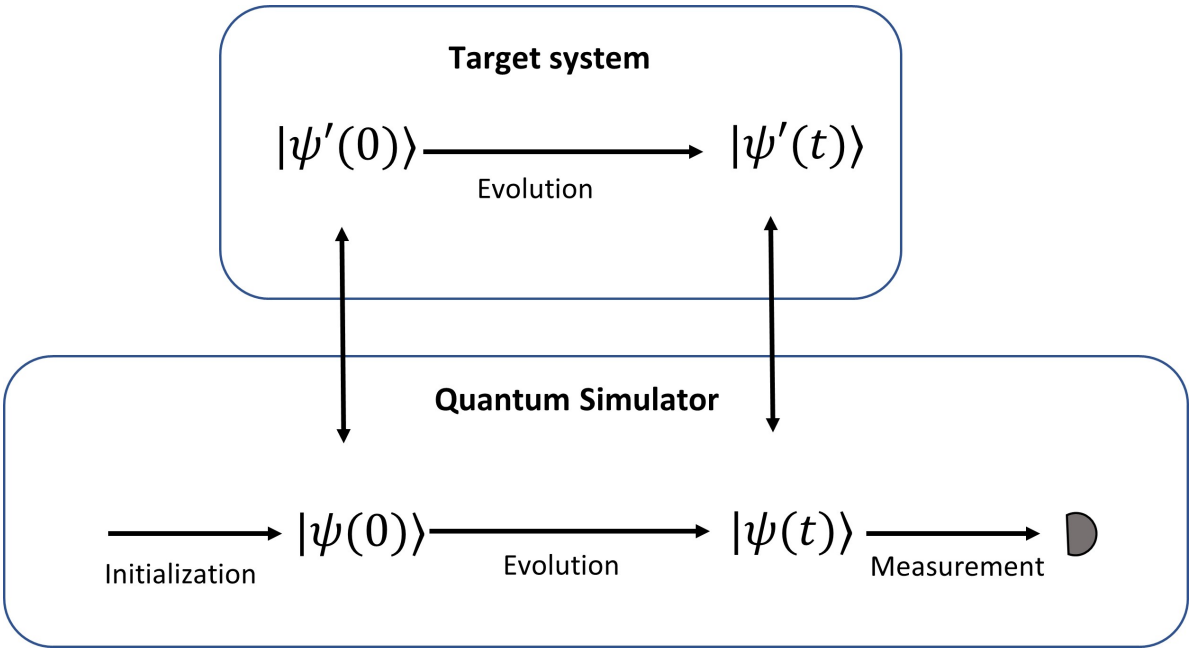

Figure 6.1: A target quantum system is simulated by a quantum simulator- another simpler quantum system with easily tunable parameters. The quantum simulator needs to be prepared in the same initial state (as the target system) after which it needs to mimic target system evolution and eventually the simulator's final quantum state needs to be measured accurately [155].

Then H_{sys} can be formed by simply adding these Hamiltonians together which act separately on $|\psi(0)\rangle$ to produce $|\psi(t)\rangle$. It was shown that H_{sys} can be rebuilt with loacal Hamiltonians H_i over small time steps using Trotter decomposition [157],

$$e^{-iH_{sys}t} \approx (e^{-\frac{iH_1t}{n}} e^{-\frac{iH_2t}{n}} ... e^{-\frac{iH_nt}{n}})^n \tag{6.1}$$

This holds exactly for the time in independent Hamiltonian $H_{sys} = \sum_i H_i$. For time dependent H_i, Eq. 6.1 is approximate. There are errors. But those errors become smaller and smaller for smaller time intervals. Lloyd showed [156] that for any desired precision (i.e. any finitely small errors), the time taken for the simulation grows only polynomially with the number of qubits N and not exponentially. This shows that any unitary dynamics can be

simulated using such a digital quantum simulator (see Fig. 6.2). It implies that a universal digital quantum computer, if built, would also work as a universal quantum simulator.

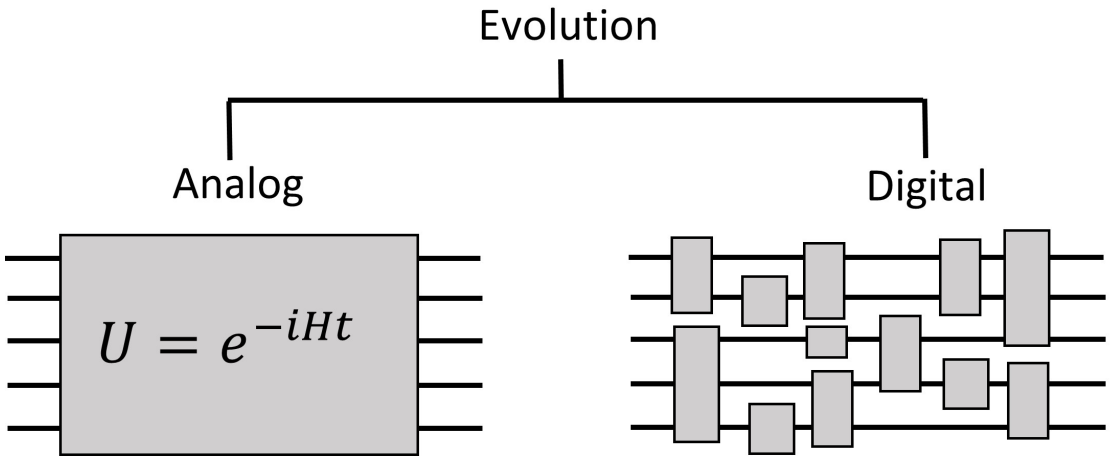

Figure 6.2: The evolution of a quantum simulator shown in Fig. 6.1. can be carried out in two ways. One would be the whole simulator Hamiltonian mimicking the target system Hamiltonian (analog simulation) while another is using only local interaction between simulator qubits (digital simulation) [155].

6.2 Different physical systems

Quantum simulations have been performed in various physical systems [153]. In this section, some of the basic ideas of performing a quantum simulation are explained by describing a few experiments. We will primarily focus on ultracold atoms [158, 159, 160, 161] which is one of the most advanced systems in the context of quantum simulations. Experiments in other systems are reviewed afterwards.

6.2.1 Ultracold atoms

Ultracold atoms are atoms that are kept near absolute zero (0 Kelvin) temperature by using various cooling techniques like laser cooling, evaporative cooling etc. These atoms can be either fermions or bosons depending on their total angular momentum. By controlling the interactions among the cold atoms or subjecting them to carefully tuned potential landscapes

one can study the various many-body physics phenomena involving either fermions or bosons as they occur naturally in many systems, especially in condensed matter systems [159, 160, 161, 162]. Due to their ability to simulate solid state physics, systems of ultracold atoms are also called artificial solids.

Ultracold atoms are primarily used for analog simulation. Analog simulation is carried out by designing a system Hamiltonian that is of the same form as a target Hamiltonian although with much greater tunability. Ultracold neutral atoms are perfect for such implementation as experimental parameters can be tuned over many orders of magnitude [161]. Moreover, the atoms can be measured with great precision individually or collectively using different methods. A few simulation protocols using ultracold atoms are described below.

We first describe how ultracold Fermi gases can be used to simulate different parameter regions of superfluidity in one system [163, 164, 165, 166]. Ultracold Fermi atoms are trapped in a harmonic trap. These atoms together behave like an interacting Fermi gas with interaction between them occurring primarily from collisions. The strength of these interactions can be controlled using Feshbach resonances [167]. The interaction strength can be changed by many orders of magnitude by using an external magnetic field. When the interaction is weak the atomic system forms a weakly interacting Fermi gas where two fermions pair up and form Cooper pairs. However, this pairing is in the momentum space and hence the fermions are generally far apart physically. The wave function of these Cooper pairs can be understood using the Bardeen-Cooper-Schrieffer (BCS) theory which first explained superconductivity microscopically in 1957 [168]. In the strongly interacting regime, on the other hand, the fermions tightly bind together to form bosonic molecules. These molecules are weakly interacting among themselves though. So, these weakly interacting bosonic molecules from a Bose-Einstein condensate (BEC). Hence changing the interaction strength results in a BCS to BEC phase transition in a Fermi gas. Simulating this transition also lets one investigate the region of intermediate interactions strength where the transition happens, the so-called unitarity regime [166]. This simulation of Fermi gases is quite general in nature. Although

this is carried out in cold atoms the simulation can also be used to model many other systems - e.g., neutron stars' crust made up of low-density neutron matter can be modeled despite the many orders of magnitude difference in density.

Another revolutionary achievement in cold atom simulation is creating optical lattices [159, 160, 169, 162]. An optical lattice is a lattice - like potential landscape created by interference of several laser shined at various angles. Different lattice structures can be created and lattice parameters can be tuned by changing angle, amplitude, frequency or phase of the lasers [170, 171, 172, 173, 174]. Such tunability has paved the way for optical lattices to become a perfect system which can simulate a variety of condensed matter systems. Atoms moving through optical lattices can model the movement of electrons in a solid lattice over a wide range of experimental parameters. If bosonic atoms are considered, one can observe the BEC to Mott insulator phase transition by changing the interaction strength related to the atoms' kinetic energy which will determine the atoms' ability to tunnel through the lattice potential [175, 176, 177, 178]. the interaction strength can be changed through use of an external magnetic field by tuning Feshbach resonances [167]. On the other hand, the kinetic energy can be decreased by increasing the depth of the potential well in optical lattices. Both paths were explored experimentally to observe the BEC to Mott insulator phase transition [175, 176]. This quantum phase transition is witnessed by measuring the atomic density fluctuations. In the BEC state the atomic wave function is spread out and hence atoms are scattered over a large region. In the Mott insulator regime however, the kinetic energy is much lower than the interaction energy which suppresses density fluctuations as they become energetically costly. The density fluctuations of the atomic gas can be precisely detected by detecting individual atoms through an advanced fluorescence imaging technique called the atomic gas microscope [176, 179, 180].

The above experiments dealt with a collection of cold atoms. However, capability to trap and read out multiple individual atoms has also been achieved [182, 183, 181] . In a breakthrough experiment in 2017 [181], quantum simulation was demonstrated using 51

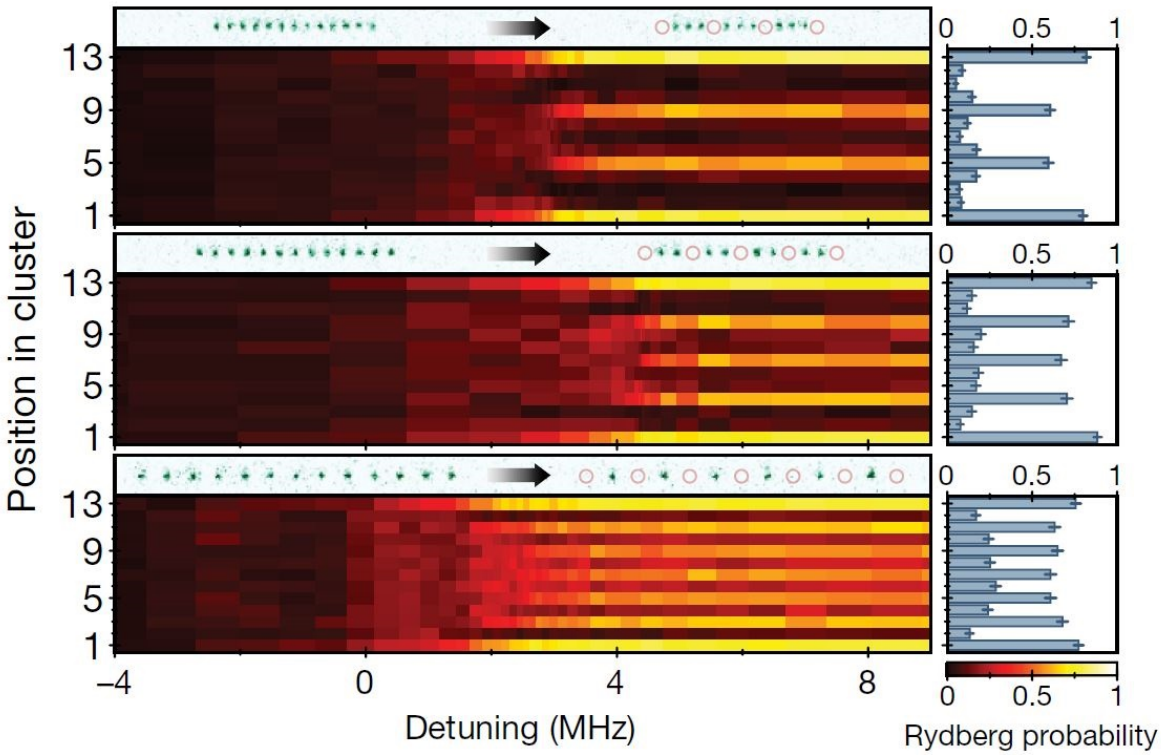

Figure 6.3: Different ordered phases were observed due to the interaction of trapped Rydberg atoms. Depending on the distance between the atoms, Rydberg interaction strength is altered and correspondingly Z_2, Z_3 and Z_4 phases were observed successively (from bottom to top panel) where Rydberg states occur once at every 2, 3, 4 atoms. The ground state of the atoms is shown by green dots and Rydberg state by red open circles. As the laser detuning is changed, the atoms gradually transition into the ordered phase which is shown in the left panel by colour coding. In the right panel, the probability of Rydberg state at each site in the end is shown using histogram. Reprinted with permission from [181].

individually trapped cold atoms. It was a 1D chain of neutral ^{87}Rb atoms. The Rydberg levels in Rb atoms were excited to implement long range interaction between the atoms. The atoms are treated as two level systems - with ground level $|g\rangle$ and Rydberg Level $|r\rangle$ being two levels - similar to spin-half particles. The chain of atoms was used to simulate a Quantum Ising type Hamiltonian with programmable coefficients by controlling the Rydberg interaction through change of atom-atom distance. Owing to the effect of Rydberg blockade, one would see different phases like the Z_2 phase where the atoms are in a state with only consecutive atoms in the Rydberg state (e.g. $|grgrgr.....\rangle$ state). The two neighboring atoms cannot be together in the Rydberg level due to the blockade effect. Increasing the blockade radius further Z_3 (e.g., $|ggrggrggr.....\rangle$ state) and Z_4 (e.g., $|gggrgggrgggr.....\rangle$ state) ordered phases were also achieved. The transition to these different ordered states is shown in Fig. 6.3 for 13 trapped atoms [181]. Z_2, Z_3, and Z_4 order states are created (from bottom to top) depending on the interaction strength which is varied by changing the distance between the atoms as shown in the panels. As the laser parameter (detuning here) is changed, the phase transition to the ordered states is clearly observed. The probability of detecting Rydberg state at each site (and how it changes with time passing) is shown by color coding. Also, the probabilities at the end are shown in separate histograms.

6.2.2 Other systems

Aside from ultracold atoms, there are several other promising physical platforms for implementing quantum simulation. One of them is trapped ions [184, 155, 185]. Trapped ions form a good system due to the ability to manipulate them precisely in ion traps, the variety of interactions possible and the almost perfect measurement fidelity [184, 155, 185, 186, 187, 188]. A transverse field Ising model simulation was carried out using trapped ions showing a transition from paramagnetic to ferromagnetic order [189, 190, 185]. An ion trap quantum simulator with hundreds of ions to simulate a tunable Ising interaction has also been demonstrated [191]. On the other hand, the trapped ion system has been proposed for and also

been used to simulate high energy phenomena [192, 193, 194, 195]. Relativistic scattering through Klein tunneling has been simulated using trapped ion system [195]. Other than analog simulations, trapped ion systems - which are a strong contender for implementing a future universal quantum computer - can be used for digital simulations too. Ising spin chain interactions with transverse field were simulated digitally in trapped ion systems [196, 197]. By employing quantum gates among the trapped ions one can program arbitrary interaction among the spin qubits and simulate the dynamics of Ising spin chain.

Another system of considerable interest is superconducting circuits which is one of the most advanced physical systems for quantum computing currently [13]. This system is also attractive for quantum simulation due to fast and tunable interactions, high fidelity quantum gates and readout [198, 199]. Another huge advantage of superconducting circuits is that they can be manufactured in different geometries easily and in scale using conventional chip manufacturing [200]. Superconducting circuits have been used to carry out analog simulation of superfluid to Mott insulator phase transition [201]. Digital simulation has also been explored on Ising model, quantum chemistry etc. [202, 203, 199].

Several other systems are being explored for quantum simulation too. Some of the interesting systems among them are quantum dots, semiconductor dopants, atom-photon interactions in cavity, polar ultracold molecules and excitons [153].

Chapter 7

Simulation of many-body dynamics using Rydberg excitons

Preface

This is the second paper of the thesis proposing to build a quantum simulator using the recently discovered Rydberg exciton system in cuprous oxide. Quantum simulations, if successfully carried out, can have a revolutionary impact in many sciences with a wide variety of applications ranging from drug discovery to material sciences. Along with giving a proposal to build a quantum simulator using Rydberg excitons, we also highlighted the possible application of such a system.

This work was done in collaboration with several co-authors. I primarily worked on the design and implementation parts of the proposal, especially the photonic aspects. I proposed and developed the alternative detection scheme. I wrote the majority of the paper with input from all co-authors.

Simulation of many-body dynamics using Rydberg excitons

Jacob Taylor[1,2,*], Sumit Goswami[3,*],Valentin Walther[4],Michael Spanner[1,5],Christoph Simon[3] and Khabat Heshami[1,5]

[*] These authors contributed equally to this work.

[1] National Research Council of Canada, 100 Sussex Drive, Ottawa, Ontario K1A 0R6, Canada

[2] University of Waterloo, 200 University Ave W, Waterloo, Ontario N2L 3G1, Canada

[3] Institute for Quantum Science and Technology and Department of Physics and Astronomy, University of Calgary, Calgary T2N 1N4, Alberta, Canada

[4] ITAMP, Harvard-Smithsonian Center for Astrophysics, Cambridge, Massachusetts 02138, USA

[5] Department of Physics, University of Ottawa, 25 Templeton Street, Ottawa, Ontario, K1N 6N5 Canada

Abstract

The recent observation of high-lying Rydberg states of excitons in semiconductors with relatively high binding energy motivates exploring their applications in quantum nonlinear optics and quantum information processing. Here, we study Rydberg excitation dynamics of a mesoscopic array of excitons to demonstrate its application in simulation of quantum many-body dynamics. We show that the $\mathbb{Z}_2$-ordered phase can be reached using physical parameters available for cuprous oxide (Cu_2O) by optimizing driving laser parameters such as duration, intensity, and frequency. In an example, we study the application of our proposed system to solving the Maximum Independent Set (MIS) problem based on the Rydberg blockade effect.

7.1 Introduction

The strong dipole transition between high-lying Rydberg states of atoms is the origin of the long-range interaction between Rydberg atoms [204, 205]. The most notable manifestation of Rydberg-Rydberg interaction is the Rydberg blockade effect where exciting one atom prevents all other atoms in a certain vicinity from being excited to the same Rydberg state [206, 207]. This feature has inspired several applications in quantum nonlinear optics [208] for development of single photon sources [209], photon-photon gates [210], and switches [211]. The application of Rydberg blockade effect has also been explored in generation of entangled states of atoms for atomic clocks [212] and for entanglement distribution in quantum repeaters [213, 214]. Progress in trapping individual atoms combined with the ability to controllably excite atoms to their Rydberg states is enabling applications in quantum simulation of quantum many-body dynamics [181, 215] and in generation of many-body entangled states [216]. Rydberg atoms in an optical lattice and the blockade effect provide the opportunity to unlock their applications in finding quantum simulation solutions for mathematical problems such as the Maximum Independent Set (MIS) problem [217].

Bound states of electron-hole pairs (excitons) in semi-conductors are governed by the Coulomb attraction and therefore demonstrate properties similar to those of hydrogen-like atoms. In semiconductors with a relatively high exciton binding energy Rydberg states of excitons can be observed. In [129], the authors observed Rydberg states of excitons in cuprous oxide (Cu_2O) and the effect of Rydberg blockade on the absorption spectroscopy outcome. This provides a platform to explore Rydberg excitons in various semiconductors for applications in quantum non-linear optics [146, 218], photonic quantum information processing, and in quantum simulation [149].

Here, we numerically simulate the many-body dynamics resulting from exciting an array of Rydberg excitons in Cu_2O. Our approach enables us to find optimal experimental conditions for quantum simulation of many-body dynamics or to reach exotic quantum states. In particular, we demonstrate that driving laser intensity, frequency and focusing can be

controlled to reach the $\mathbb{Z}_2$-ordered quantum many-body state [181]. In an example, we show the application of our proposed system to finding the solution to the MIS problem based on the Rydberg excitation pattern in a two-dimensional arrangement of Rydberg excitons. Our proposed implementation is inspired by the progress in the Rydberg excitation of individually trapped atoms, offers a path for realization in a solid-state system with potential for integration, and provides a platform to explore many-body quantum dynamics with Rydberg excitons.

Scheme– The schematic of cuprous oxide's (Cu_2O) band structure with bound Rydberg exciton states below the conduction band is shown in Fig. 7.1(a). These states can be addressed both through single-photon [129] and two-photon [219] transitions. We aim to address nS states which can be achieved with a two-photon transition via an off-resonant coupling to the $2P$ (intermediate) state; see Fig. 7.1(b). The lack of directionality in the Rydberg-Rydberg interaction between nS states enables us to consider various geometries and to eliminate complications arising from angle-dependent interaction between nP states. The excitons could be arranged in a polygon configuration (Fig. 7.1(c)) or for that matter in any arbitrary configuration. This is discussed in more detail below. In Fig. 7.1(b), we show how neighboring Rydberg states are addressed with an effective Rabi frequency (intermediate state $2P$). As shown in Fig. 7.1(c), each excitation site is driven by a focused laser and all sites are exposed to a global secondary exciting laser. Each site is used to define a qubit; $|g\rangle$ and $|r\rangle$ are the states of the qubit where $|g\rangle$ represents lack of an exciton and $|r\rangle$ an exciton in the Rydberg level.

As shown in Fig. 7.1(b), each exciton is treated as a multi-level system being addressed with an effective Rabi frequency resulting from two driving lasers. This is in particular important for Cu_2O where Rydberg states have relatively small energy spacing. At each site, the lasers are focused in a tiny spot on a very thin crystal such that a small crystal volume - smaller than the Rydberg Blockade volume - is illuminated prohibiting multiple excitations in one site. Fig. 7.1(d) shows an example profile for the effective Rabi frequency

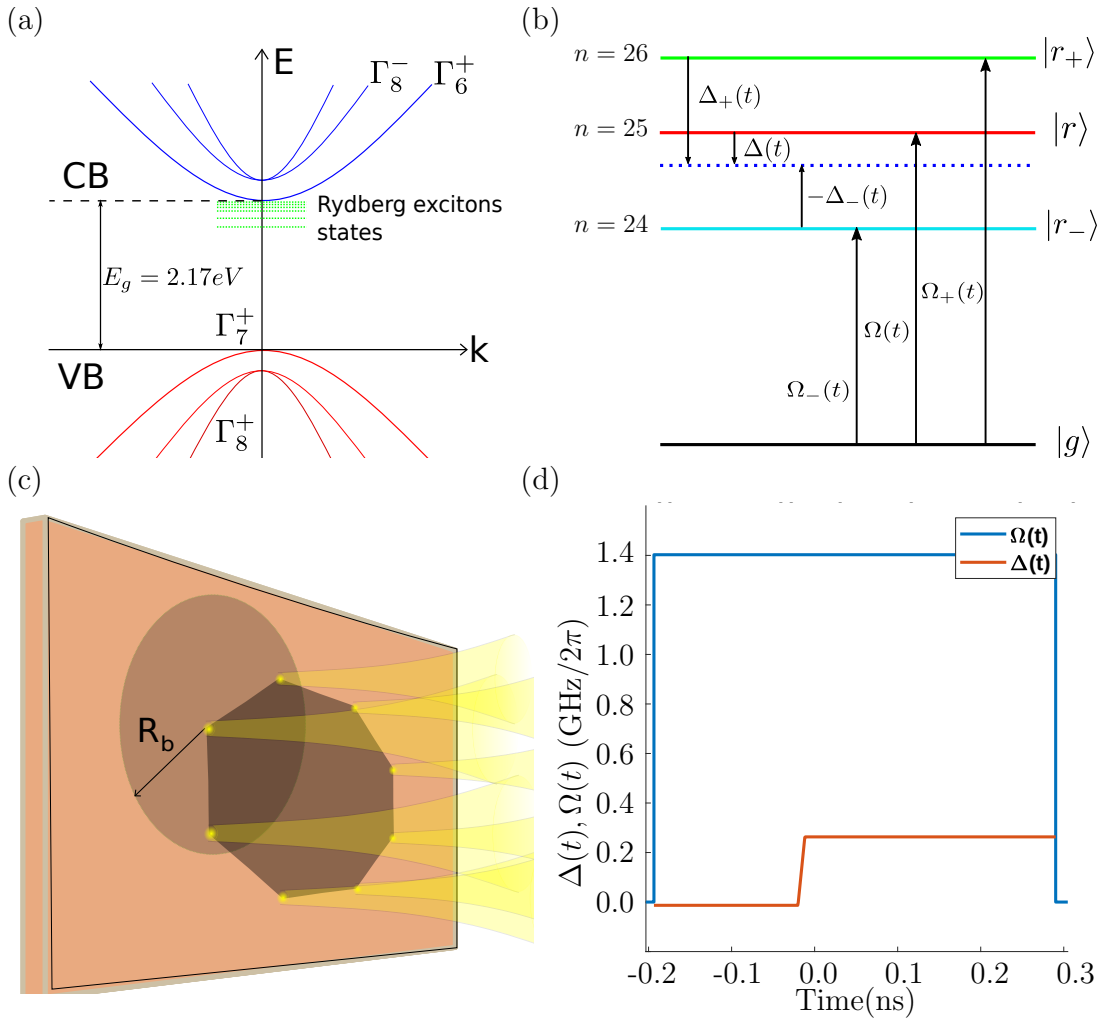

Figure 7.1: (a) Energy band structure of yellow excitons in Cu_2O (CB = Conduction Band and VB = Valence Band), (b) A diagram of the level structure for a single exciton in the case of 3 Rydberg levels, namely the $n = 24$, $n = 25$ and $n = 26$ states; nS states are accessible through a two-photon excitation mediated by the $2P$ state (not shown here). The effective Rabi frequency experienced by different states ($\Omega_k(t)$) varies due to their different transition dipole moments. (c) Schematic diagram showing how multiple exciton sites, in a regular polygon configuration, are created by focused laser excitations at selective positions in a Cu_2O micro-crystal. The blockade radius R_b of one exciton is shown which encompasses its nearest neighbours. (d) The shape of Rabi frequency and detuning with time to the $n = 25$ level is shown here.

and two-photon detuning pertaining to our numerical results that are discussed below.

The paper is organized as follows. After the introduction in Sec I, Sec II presents the model for our quantum simulation and discusses the results for a polygon configuration of excitons. We discuss the potential practical application of our scheme to solve MIS problems in Sec III. Sec IV depicts the road ahead for the implementation of our model. There a comparison is made with the atomic case with directions for future improvement, and challenges like losses and various other issues associated with implementation are discussed. We conclude in Sec V by summarizing our results.

7.2 Simulation

We study the many-body Rydberg excitation dynamics under the influence of population dynamics and Rydberg-Rydberg interaction. An exciton in the Rydberg level has a large dipole moment which prohibits an excitation within a certain distance, called blockade radius (R_b). In our scheme (see Fig. 7.1(c)), the blockade radius R_b contains the neighbouring exciton site but not the next nearest-neighbour site. Hence, the Rydberg blockade effect blocks the two nearest neighbors from being excited together creating the $\mathbb{Z}_2$-ordered phase, i.e. states of the form $|rgrgrg...\rangle$ or $|grgrgrg...\rangle$. Similar to these $\mathbb{Z}_2$-ordered states, our general objective states are the states with the maximum number of excitations that can occur without any additional excitations within the blockade radius of a Rydberg exciton. Our numerical treatment of the many-body dynamics aims to find the optimum pulse energy and detuning to reach these objective states with the highest probability of success. To afford numerical simulation of several multi-level systems we do not include the effect of excitation decay. To circumvent this limitation, we operate at a fast excitation regime where the total population dynamics remains faster than the expected lifetime of the Rydberg states; see below for a more detailed discussion.

The excitons are detected by applying a detection laser (de-excitation) pulse to take

them to the $2P$ state and then collecting the photons emitted from the $2P$ exciton decay. Collection fibers and detectors can be placed behind every site to collect emitted photons. However, this detection scheme is rather inefficient as the probability of collecting photons in one direction from the excited state is small. The detection scheme and alternate approaches to increase the detection efficiency dramatically are discussed in detail in Section 7.4.3.

In our proposal based on Cu_2O, excitons in nS states, can only be excited via two-photon excitation in a ladder configuration through the intermediate P states, owing to the selection rules. Off-resonant coupling to the transition that promotes an exciton to the $2P$ state provides the flexibility to operate at various wavelengths. The two-photon excitation scheme [220, 221] off-resonantly through an intermediate state (*e.g.* the $2P$ state) can help circumvent the underlying phonon-assisted absorption [129]. This approach is expected to enable sharp two-photon transitions with optical depth and Rydberg blockade properties comparable to that of cold atomic ensembles [220]. For the single-photon detuning of δ with respect to the $|2P\rangle$, the effective Rabi frequency representing the coupling to the $|nS\rangle$ is given by $\Omega = \Omega_1\Omega_2/\delta$, where $\Omega_{1,2} = \langle E_{1,2} \cdot d_{g2P,2PnS}\rangle/2\hbar$. Here $E_{1,2}$ are electric field associated with the two excitation fields and d_{ij} is the transition dipole moment for $|g\rangle \rightarrow |2P\rangle$ and $|2P\rangle \rightarrow |nS\rangle$ transitions. The ground state here represents a lack of exciton and the mode is determined by that of the E_1. For large δ (i.e. $\delta >> \Omega_1, \Omega_2$), we can describe the two-photon transition with the effective Rabi frequency, Ω. Such two-photon excitation was long used to excite nS Rydberg excitons [222] with optical and infrared lasers. A degenerate two-photon excitation with a laser at 1eV could simplify the experimental condition. Resonant coupling to the intermediate state is also a possibility based on electromagnetically induced transparency as explored in [218, 220] - using an optical and another THz laser - to show enhanced non-linearity through Rydberg excitons in an optical cavity.

Contrary to the Rydberg atoms, in Cu_2O excitons, the separation between Rydberg levels is not much greater than the linewidth of these levels. The smaller ratio of line separation and linewidth is a major challenge for effective excitation of Cu_2O excitons to a single

Rydberg level; which can be important for quantum information processing applications. While trying to excite the intended excited state (say, $n = 25$) we may inadvertently excite adjacent levels too ($n = 24$, $n = 26$ etc). This significantly decreases the probability of achieving the objective state(s) in the Cu_2O exciton system compared to the atomic system, as discussed later. Hence, this effect is needed to be included for an effective simulation of the quantum dynamics. For this purpose, we model each Cu_2O exciton as a 4-level system, 1 ground and 3 Rydberg levels system as shown in Fig. 7.1(b). We aim to excite the $n = 25$ level. For this high lying Rydberg level ($n = 25$) the energy gaps to the adjacent Rydberg levels are relatively small, $2\pi \times 2.81$ GHz above and $2\pi \times 3.18$ GHz below [129] while the linewidth of $n = 25$ level is around $2\pi \times 0.102$ GHz.

In our model, each exciton is driven by a laser with k^{th} Rydberg state coupled by effective Rabi frequency $\Omega_k(t)$ and detuning $\Delta_k(t)$. The interaction potential between two exitons at i^{th} and j^{th} position is modeled by the principal number dependent van der Waals interaction $V_{k_{ij}} = \frac{C_k}{R_{ij}^6}$, where R_{ij} is the distance between the two excitons and C_k is the interaction coefficient corresponding to the k^{th} Rydberg level. The Hamiltonian governing such a system is given by

$$\frac{H}{\hbar} = \sum_{k,i} \frac{\Omega_k(t)}{2}(\sigma_i^k) - \sum_{k,i} \Delta_k(t) n_i^k + \sum_{k,i>j} V_{k_{ij}} n_i^k n_j^k, \tag{7.1}$$

where $|g_i\rangle$ and $|r_i^k\rangle$ represent the the lack of an exciton and an exciton in kth Rydberg level respectively at the ith position (site) in the arrangement. $\sigma_i^k = |r_i^k\rangle \langle g_i| + |g_i\rangle \langle r_i^k|$, $n_i^k = |r_i^k\rangle \langle r_i^k|$, and $V_{k_{ij}}$ is the interaction potential between excitons i and j. As it can be seen in Eq. 7.1, the interaction between different Rydberg states such as $24S - 25S$ is not included in this model. Such cross-interaction terms brings a breadth of possibilities specially in study of wave-packet dynamics in Rydberg excitons where a superposition of multiple Rydberg states of the same exciton is present [223]. Here, we minimize excitation to states other than the targeted $25S$ state numerically to eliminate the effect of these cross-interaction terms.

Using a reference Rydberg state, the detuning with respect to the other adjacent states, $\Delta_{k'-1}$ and $\Delta_{k'+1}$, are calculated from the energy gaps [129]. Thus given k' as a reference level, R_y the Rydberg constant and δ_p the quantum defect, $\Delta_k(t)$ is calculated as $\Delta_k(t) = \Delta_{k'}(t) + \frac{R_y}{(k'-\delta_p)^2} - \frac{R_y}{(k-\delta_p)^2}$. Similarly we calculate the Rabi frequency for each Rydberg level using a set of Rabi frequencies and the relative electric dipole moments (μ_k), given a reference k' then $\Omega_k(t) = \sqrt{\frac{\mu_k}{\mu_{k'}}}\Omega_{k'}(t)$. In our case the reference k' is the k'=25 state, for all parameters. We propose the same square pulse for all the lasers, so the Rabi frequency is constant in time and space ($\Omega'_k = \Omega$) with $\Omega = 2\pi \times 1.404$ GHz, while $\Delta(t)$ is time dependent and is iteratively optimized to maximize the probability of reaching a selected objective state(s). In particular $\Delta(t) = at^3 + bt + c$ is selected where a, b, c are constants optimized for a small system size (such as 5) which is then used for the computation of larger site systems. This $\Delta(t)$ is also truncated from above/below by $\Delta_{\max}$, $\Delta_{\min}$ respectively, are selected as to minimize the excitation of neighboring states. The shape of $\Omega(t)$ and $\Delta(t)$ used for the simulations are shown in Fig. 7.1(d).

We choose the distance between two excitons (i.e. the nearest neighbor distance) as a fraction of the blockade radius. The blockade radius is the distance between the exciton sites such that $V_{ij} = \Omega$, or more directly $R_b = \sqrt[6]{\frac{C_6}{\Omega}}$. The distance was chosen to be about $0.958 \times R_b = 2.72\mu m$ [224]. By having the exciton sites separated by this distance, nearest neighbors have $V_{k_{ij}} >> \Omega_k$, while second nearest neighbor have $\Omega_k >> V_{k_{ij}}$. This effect, referred to as Rydberg blockade, blocks nearest neighbors from becoming excited. This was done with the goal of obtaining an ordered objective state(s).

Our objective state(s) refers to the state(s) with the maximum number of excitations that can occur without any nearest neighbors being excited for any arrangement of the exciton sites. Hence, in our simulation where 12 exciton sites are arranged in a regular polygon, the objective states would consist of two states - $|rgrgrgrgrgrg\rangle$ and $|grgrgrgrgrgr\rangle$. When the sites in a polygon are excited by lasers a superposition of these states should ideally be the final state of the system with high probability. We numerically simulated this dynamics.

The state probabilities are plotted over time in Fig. 7.2(a). The objective states for the 12-site polygon are the most probable states. In Fig. 7.2(a), we show the population dynamics for generation of the objective states with any of the three neighboring Rydberg states excited. As we aim to minimize Rydberg excitation in neighboring states this is relatively close to dynamics of generating the objective state with a specific Rydberg state denoted as $|r_1gr_1...gr_1g\rangle$ and $|gr_1g...r_1gr_1\rangle$.

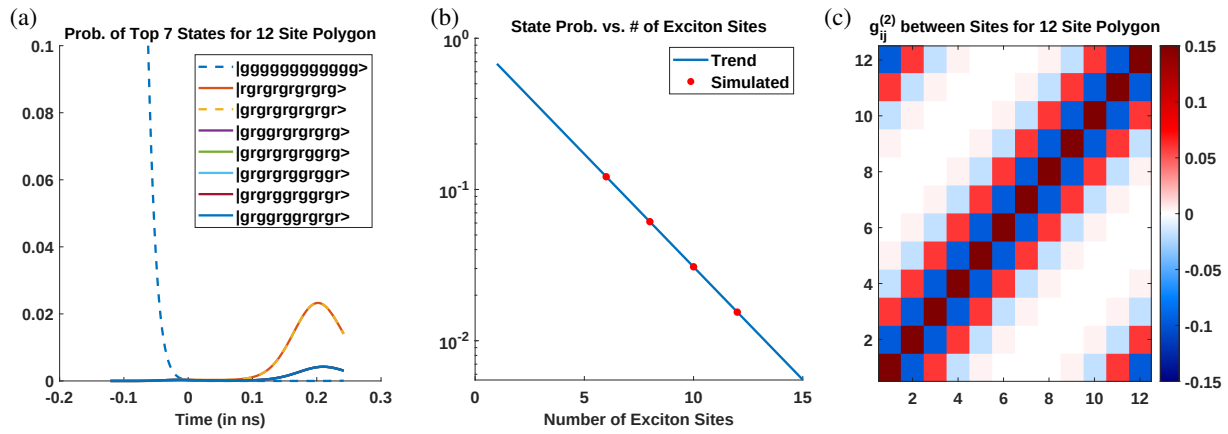

Figure 7.2: (a) Probabilities are plotted with time for the 7 most probable ensemble states and the initial state with no excitons, $|gggggggggggg\rangle$ (dashed blue line), for 12 exciton sites in a polygon configuration. For 12 sites the most probable states, $|rgrgrgrgrgrg\rangle$ and $|grgrgrgrgrgr\rangle$, are equally likely. (b) Probabilities of achieving the objective state(s) for simulations with different number of exciton sites are shown. The scaling can be modelled with a exponential decay as shown with the blue line. (c) Correlation function $g_{ij}^{(2)}$, defined in Eq. (7.2) between two excitons at specific positions (i and j), for 12 excitons with periodic boundary conditions. Exciton sites neighboring each other, due to the blockade effect, are mostly anti-correlated. The next nearest neighbour sites are then mostly correlated.

The maximum probability of the objective state(s) ($|r_1gr_1...gr_1g\rangle$ and $|gr_1g...r_1gr_1\rangle$) decreases with more exciton sites, as shown in Fig. 7.2(b). For a set of 6, 8, 10, and 12 exciton sites probabilities to achieve the objective state are 0.1214, 0.06127, 0.03082 and 0.01545, respectively. Here, it should be noted although the shape of $\Delta(t)$ with time is optimized to get the highest probability, the same $\Delta(t)$ profile was used for all the different exciton sites. This is to ensure scalability of our approach so that the optimization results can be applied to higher number of excitons where solving the population dynamics become intractable.

The probabilities in Fig. 7.2(b), similar to the system of individually trapped atoms (see Fig. 4 in Ref. [181]), shows a clear exponential trend. Extrapolating this trend we calculate that a polygon of 50 exciton sites would be expected to attain the objective state with a probability of around $P = (3.30 \pm 0.07) \times 10^{-8}$. This estimate is motivated by the experimental demonstration of the many-body ordered phase in an array of individually trapped atoms [181] and will allow us to gain perspective over our numerical results.

Full quantum state tomography remains very challenging as it requires a high number of complementary measurements. An alternative and very important metric to measure the ordered objective state is by measuring the second order atom-atom correlation function defined as -

$$g_{ij}^{(2)} = \langle n_i n_j \rangle - \langle n_i \rangle \langle n_j \rangle, \tag{7.2}$$

where the average ($< ... >$) is taken over many repetitions. The blockade effect is apparent within Fig. 7.2(c) where a positive value implies correlation while negative value implies anti-correlation. The anti-correlation between the neighbouring sites and the correlation between next-nearest neighbours shows a critical signature of the $\mathbb{Z}_2$-ordered phase induced by Rydberg blockade between the nearest neighbours. We also see correlation in top-left or bottom-right corner of Fig. 7.2(c) because the arrangement here is periodic - e.g. site 1 is also the neighbour of site 12 and hence they are correlated.

Although the objective states we expect ($|rgrgrgrgrg\rangle$ and $|grgrgrgrgr\rangle$) - described as the $\mathbb{Z}_2$ order in [181] - has complete correlations, these only occurs with probability 2×0.015 while other states with partial or no correlation also occur (Fig. 7.2(a)). As the correlation function, $g^{(2)}$, is averaged over many runs of the simulation it dies down quickly after a few sites. This is expected and similar results occurred in trapped atom simulation experiments [181]. However, this makes $g^{(2)}$ an interesting and accessible experimental signature as this correlation can be seen even in the presence of significant loss.

7.3 Application

Maximum Independent Set (MIS) problem aims to find the largest subset of nodes in a graph where no two nodes are adjacent (linked by an edge). It has been shown that solution to NP-complete problems such as the MIS problem on planar graphs can be mapped onto the ground state of a multi-body Rydberg system with proper arrangement of Rydberg atoms (or in our case excitons); see [225]. This ground state is our objective state with maximum number of Rydberg excitations such that no two excitations occur within the Rydberg blockade radius. If there are two excitations within the blockade radius the total energy goes up and it is no more the ground state. The Rydberg blockade effect combined with a proper positioning of Rydberg excitons will allow us to naturally reach a solution for the MIS problem. Finding the correct position for each Rydberg exciton is an exponentially challenging task for large graphs. Below we treat an example with a graph of 10 nodes as shown in Fig. 7.3(a).

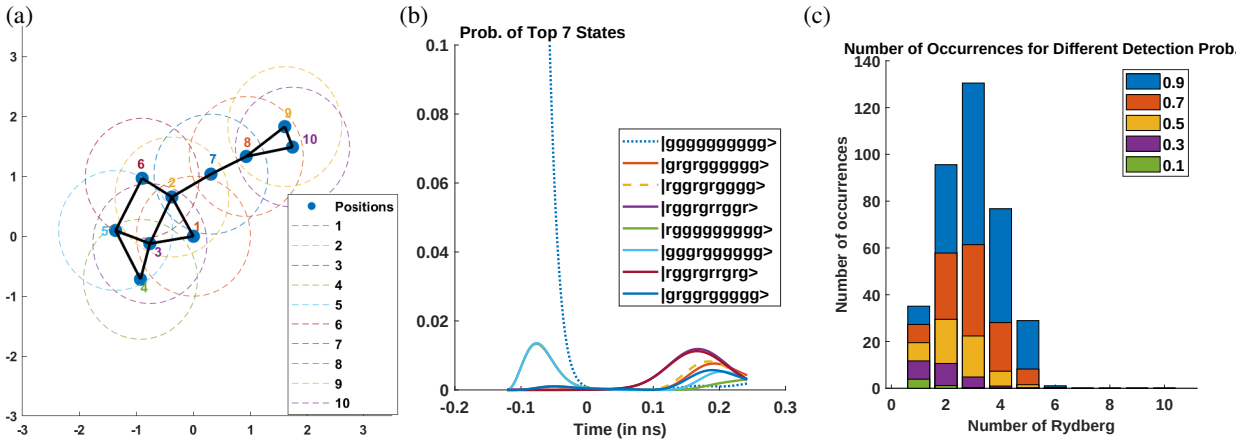

Figure 7.3: (a) A 10 site graph with sites arranged arbitrarily in 2D to solve a Maximum Independent Set (MIS) problem using the excitons. The blockade radius of each exciton is shown by a dotted circle around it and if the separation between two excitons is less than the blockade radius they are connected by an edge creating the graph. (b) Probabilities over time of achieving different states for the 10 site graph. The probability of achieving the MIS objective states was found to be 0.01187 and 0.01124, with a total probability of 0.02311. (c) The number of occurrences for different amounts of Rydberg excitons, based off 2000 runs. The histogram is shown for expected number of detections given non-unitary detection probabilities of 0.9, 0.7, 0.5, 0.3 and 0.1.

The polygon scheme described before was a trivial MIS configuration, with the objective

state easy to find theoretically. Although we observed that the probability of achieving the objective state is not very high in one repetition of the experiment - $P = 2 \times 0.015$ for 12 sites in a polygon case - that wouldn't eliminate our ability to find a solution as a solution is easy to check in polynomial time. Given a solution one simply needs to check if two of the excitations are within blockade radius - if not it is a 'valid' solution and one looks for the valid solution with maximum number of excitations. All that would be required is enough experimental runs to have a high enough confidence there is no 'valid' larger set of excitations.

We depict such an MIS case in Fig. 7.3. Part (a) shows the ten exciton configuration arbitrarily placed in 2D with the solid lines showing the associated planar graph. The evolution of different possible final states of the exciton ensemble are shown in Fig. 7.3(b). The objective states (which are called 'ground states' in [225]) with the maximum possible five excitons each, $|rggrgrrggr\rangle$ and $|rggrgrrgrg\rangle$, have the highest probabilities, 0.01187 and 0.01124, with a total probability of 0.02311. The number of Rydberg excitation in the final state is plotted as an histogram in Fig. 7.3(c) over 2000 runs. We see a finite number of occurrences for five excitons but six excitons also occur in small number (at detection efficiency 0.9). Creation of six excitons is an error due to the presence of other nearby Rydberg states (see, Fig. 7.1(b)). It can be easily checked that no state associated with six excitation is 'valid', as defined earlier. So, we conclude the five excitation states are our objective (ground) states. Fig. 7.3(c) shows the effect of finite detection efficiencies too, as Rydberg excitation numbers are indicated in different color for different detection efficiencies. Naturally, for lower detection efficiencies we expect to detect smaller number of excitons as more excitons in the final state remain undetected. Low detection efficiency limits us in finding the objective state with maximum number of excitons; however, as it can be seen in Fig. 7.3 even for a detection efficiency of 0.7, 2000 runs (attempts) is enough to find the solution to the associted MIS problem. The objective state can be found at even lower detection efficiencies by increasing the number of runs.

7.4 Implementation

7.4.1 Comparison with atoms and improvements

In the following, a comparative analysis is drawn between Rydberg atoms and Rydberg excitons (in Cu_2O) for their application as a quantum simulator. This will allow us to put our results in perspective and motivate experimental efforts based on Rydberg excitons. Significant progress in trapping individual atoms and well-known Rydberg properties and excitation strategies puts the atomic systems at a significant advantage. However, the relatively slow trapping, excitation, and detection steps (in order of milliseconds) can become a bottleneck in applications that require sampling over many outcomes. On the other hand, for the fast exciton system trapping is not required which will offer simplicity and operation time in the order of nanoseconds.

The closely placed absorption lines of Rydberg excitons (in Cu_2O) prohibit effective excitation of Rydberg states resulting in low probability of success in achieving the objective state. The probabilities achieved in our Rydberg exciton simulation are much lower than what is achievable with trapped atoms [181]. In Cu_2O excitons, the radiative linewidth of $n = 25$ state is $2\pi * 0.102$ GHz as compared to the $2\pi \times 2.81$ GHz line separation between $n = 25$ and $n = 26$ levels. The linewidth is further broadened due to power broadening effects. The small line-separation limits the range of Ω that can be used. To generate the objective state one must prevent excitations into higher/lower Rydberg levels ($n = 24, 26$ in our model). It is therefore desirable to have $\Delta_k > \Omega_k$ for $k \neq 25$. In sharp contrast, this condition is very easily satisfied in the atomic system where the atomic linewidth is millions of times smaller than the line separation. Fortunately, this large linewidth and hence the small lifetime of excitons is not without benefits, as it also allows many iterations of the experiment to be performed orders of magnitude faster than individually trapped Rydberg atoms. Operating on orders of nanoseconds instead of 100 μs, as in the atoms. This allows one to do 100,000s of times more repetitions in the same time, increasing the number of

successful attempts in generating the objective state. This in turn increases the probability of a successful detection and hence identification of the objective state.

To compare these two different systems quantitatively we ask the following question - for how much time T must the experiment be run to achieve a particular probability (say 99%) of identifying the objective state of the simulation with n number of sites?

Detection probability is taken as 99% for each atom. It is similarly high for excitons, which is justified for the alternative detection scheme discussed in Section 7.4.3. For the excitons we use a more conservative 90% detection probability here combining the effect of decay loss too. This is discussed and justified in detail in Section 7.4.2.

A single experimental run time takes around 250 ms for the atoms [181] and estimated to be around 5 ns for the exciton. Assuming the above parameters, for the 50 site case, to get a 99% chance of the correct state occurring at least once, about 1.94 billion runs need to be made for the exciton case. This can be achieved in around 9.72 seconds. While for the atomic case only 842 runs are needed. However, due to the larger individual run times this would take around 210 seconds.

A smaller time for single experimental run lowers T by a fixed factor, while a better scaling of success probability with n (data in Fig. 4a of [181] for atoms and in Fig 7.2(b) here for excitons) enhances T slower for higher n. Hence, the atomic system perform favorably for higher value of n (more number sites) while exciton system (in Cu_2O) is faster for smaller n values.

It can be concluded from the above analysis that to scale to a really large number of sites, in the long term, one would actually need to improve line-separation vs linewidth ratio which differentiated the excitons from the atoms. This has been a problem in Cu_2O system as other unwanted nearby states get excited which resulted in ineffective Rydberg excitation and correspondingly worse success probability scaling. In the Cu_2O system, the small lifetime and the corresponding large linewidth of the Rydberg excitonic states caused this. Optical cavities could be used to enhance the coupling efficiency or to reduce the

decay rate in such a system. This deserves a dedicated study to find optimal conditions for quantum nonlinear optics with Rydberg excitons. Another possible solution to this problem may be to use engineered micro structures to enhance the lifetime. Such a system has recently been experimentally demonstrated in the context of exciton condensation, in $MoSe_2$–WSe_2 double layer material where the inter-layer excitons demonstrate long lifetimes and maintain the large binding energy which is required to observe and address Rydberg states [226]. Optical addressing and lifetime measurement of excitons in such structures have recently been studied in [227] with exciton lifetime of 0.2 ms. Although such long lifetimes may not actually be needed. Possibly a lifetime close to a microsecond would be enough as that would already mean a line separation vs linewidth ratio above 1000. However, there would be complications for long lifetimes as we would need trapping to keep the excitons in one place which would otherwise move due to thermal motion, discussed in details in Section 7.4.4 . However, there is an important difference with the trapped atoms. Rydberg excitons can be trapped mechanically using strain traps [228]. Such mechanical traps can be part of fabrication or prepared with the system. This would save precious trap preparation time for each iteration of the experiment, as needed for optical traps containing Rydberg atoms.

7.4.2 Decay loss

There are two principal sources of loss in our system - decay loss and detection loss. Detection loss and ways to avoid it are presented in detail in Section 7.4.3. The decay loss is caused by the decay of Rydberg states during the simulation. The objective state decays at a rate proportional to the number of excitons present. Thus given a fully connected ensemble in a regular polygon arrangement, the worst possible decay rate is proportional to 1/2 the size of the ensemble. For fewer Rydberg excitations, in partially connected ensembles, the effect of decay is even less. The low probability of Rydberg excitation at early part of the dynamics (see Fig. 7.2(a)) and our fast excitation timescales with respect to the lifetime allow us to reliably remove excitation decay from our numerical simulations for small number of sites.

This helps to put computational resources towards treating higher number of qubits. The objective state has a significant probability of being excited only starting from 0.1 ns (see Fig. 7.2(a)). As the simulation ends at 0.24 ns, considering $\sim$ 1 ns lifetime of the state, an individual exciton has a maximum of 14% chance of decay during simulation. However, this is only if an exciton is already excited by 0.1 ns, i.e. when the excitation probability is just picking up (as in Fig. 7.2(a)). On average, excitons would be excited much later and hence the decay probability would also be smaller. As a crude estimation, it can be considered around half of that ($\sim$ 7%).

Even then, for a large number of sites, exciton decay can no longer be neglected for theoretical simulation of the final state. However, for the practical purpose of detecting the objective state in an experiment, the exciton decay loss plays an equivalent role to the detection loss. The two losses manifest themselves differently - decay loss produces incorrect final states of simulation and detection loss inhibits the correct detection of the final state. But they both obstruct finding the objective state. With enough number of experimental runs one can find the objective state in the presence of each of the two losses. Hence, the maximum possible loss would simply be a combination of the two losses and the two losses can be treated equivalently for the purpose of finding the objective state; our prime goal in this proposal. Hence, even if we extrapolate our results for much larger number of sites (as we did for 50 sites using Fig. 7.2(b)) without considering the effect of exciton decay, we would still find the correct minimum probability of detecting the objective state(s) as long as we combine the decay loss with the corresponding detection loss.

7.4.3 Detection

Faithful detection of the final state is an important requirement of our scheme. In the original detection scheme, we try to detect the $|r\rangle = |25S\rangle$ state by making it decay and detecting emitted photon. However, $|25s\rangle$ state can only decay by two photon emission. Hence, as shown in Fig 7.4 (a) we transfer the $|25S\rangle$ state to $|2P\rangle$ state by a THz detection laser and

detect the photon emitted from the $|2P\rangle$ state. This detection scheme completely depends on the ability to detect the one photon emitted from the $|2P\rangle$ state. Even if one reaches a very high combined collection and detection efficiency (say, around 90%) of detecting the single photon or equivalently a single Rydberg excitation, the probability of detecting the final state decreases exponentially with larger number of excitons. Moreover, the large size of Rydberg excitons ($\sim 1\mu m$) compared to their blockade radius ($\sim 2.82\ \mu m$) means Rydberg excitation lasers (used for simulation) must be focused to a small area in the middle of the crystal resulting in excitation in a single exciton compared to a collective excitation over multiple excitons. Hence, there would be no preferred directions to the emitted photon in contrast to collective emission. This random direction of emission, coupled with limited coupling efficiency with the collecting fiber and finite detector efficiency lowers the photon detection efficiency. One way to enhance efficiency is using an optical cavity which would result in a directional emission even from a single exciton. Cavity would also enhance the coupling strength of the relevant exction line while not enhancing the other off-resonant lines which would suppress the off-resonant excitations. However, fabricating such a cavity would also be challenging as it needs to have a quality factor in hundreds of thousands. In this context, it should be noted - as we have stressed before - low detection efficiency doesn't affect g_2 correlation function considerably as it is averaged over.

To solve this problem, in the following we propose an alternate detection scheme which drastically improves the detection efficiency. Instead of directly detecting the Rydberg excitation by making it decay, here we detect the presence of the Rydberg state $|r\rangle$ indirectly, as a non-demolition detection. The scheme is based on cyclic transitions as shown in Fig 7.4(b)-(c). Detection lasers pulses are applied at all sites to create low lying Rydberg excitons (say, 2P or 6P state). We try to detect the emitted photons and the sequence is repeated.

In the absence of a Rydberg excitation (i.e. at the sites in $|g\rangle$ state) $|2P/6P\rangle$ excitons would be created and decay by emitting photons (Fig 7.4 (c)). While in the presence of a Rydberg excitation (i.e. at the sites in $|r\rangle$ state) ideally no $|2P/6P\rangle$ excitons should be

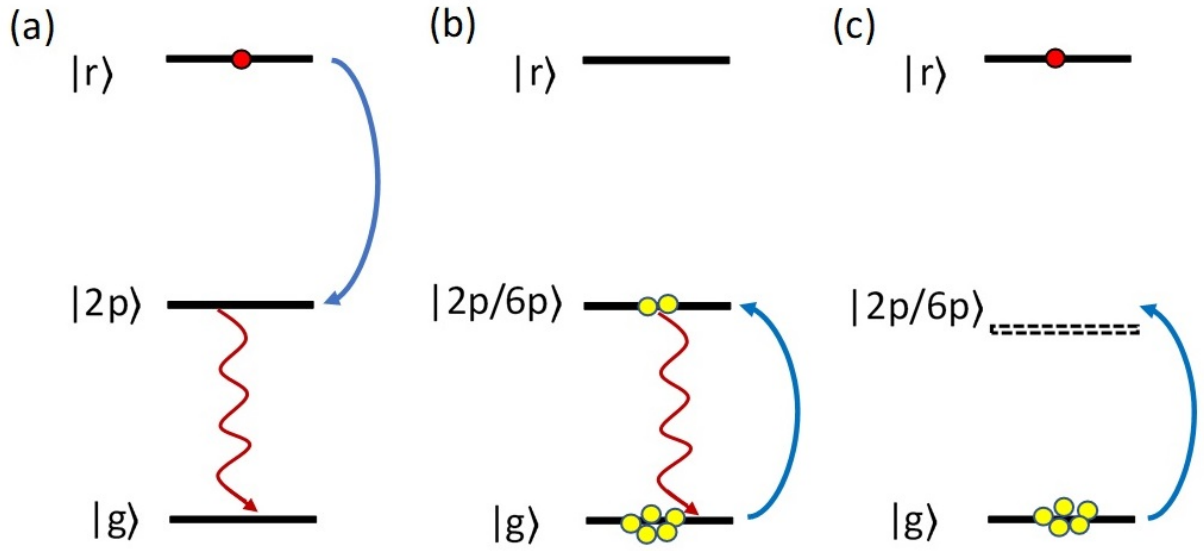

Figure 7.4: The two different detection schemes are shown. In the original scheme (a) Rydberg excitons in $|r\rangle = |25S\rangle$ state are detected directly by first transferring it to $|2P\rangle$ state and then detecting the emitted photon. In the alternate scheme the presence of the $|r\rangle$ state is detected indirectly, as a non-demolition detection, through many-body fluorescence detection. Detection laser pulse is applied to create low lying short lived P excitons which decays by emitting photon that gets detected. The sequence is later repeated to detect a large number of photons from each site. Moreover, many P excitons are created at each site in each iteration as they are small in size compared to the $|r\rangle$ exciton. Such P excitons are created if no $|r\rangle$ exciton is present (b) but in presence of a $|r\rangle$ exciton creation of P excitons gets hindered due to the blockade effect (c).

excited due to the blockade effect (Fig 7.4(b)). Such asymmetric Rydberg interaction exists and has been observed between 6P and 17P states of Cu2O excitons. This was prominently seen in Fig. 3(e) of [129]. We expect a similar effect between $|25S\rangle$-$|2P/6P\rangle$ excitons will allow us to implement our proposed detection strategy. This would result in reduced excitation probability at a site in $|r\rangle$ state compared to one in $|g\rangle$ state. Hence $|g\rangle$ and $|r\rangle$ states can be easily distinguished if a large enough number of photons can be collected. The alternate detection scheme constitutes a non-demolition measurement of the Rydberg state. Although, it does constitute a measurement, e.g. destroying the coherence between two degenerate $\mathbb{Z}_2$ eigenstates. P excitons are excited resonantly here, contrary to the two-photon excitation of S excitons, resulting in a phonon-assisted background absorption. However, the background is not significant compared to the transition line. It is complicated to include the exciton-phonon interaction in calculations. Hence, we neglect the effect of the background absorption in our calculation.

The relatively small energy gap between Rydberg states and the asymmetric Rydberg-Rydberg interaction raises a question whether all possible cross-interaction terms ($n'S - nS$ for $n' \neq n$) should also be included in Eq. 7.1. In this work, we minimized excitation in neighboring Rydberg states (where $k \neq 25$) to eliminate the effect of such cross-interaction terms on the Rydberg population dynamics. For broadband addressing of Rydberg states and study of Rydberg exciton wavepacket dynamics, it is essential to include all potentially relevant cross-interaction terms. This novel complication introduces an opportunity to develop novel applications of Rydberg excitons in quantum information processing.

Note that the alternative detection scheme doesn't require a THz laser, only a yellow optical laser is needed. Also note that it is tricky to talk about $|g\rangle$ state and $|r\rangle$ state anymore as we are creating multiple excitons in the low lying p state. We discussed in introduction how multiple excitons can break our approximation of two level system. However, please observe that no additional $|25S\rangle$ exciton is excited due to the blockade as before. So, for simplicity we will go on with the notation by redefining $|g\rangle$ and $|r\rangle$ state as absence and

presence of $|25S\rangle$ exciton only.

The principal advantage of the alternative detection scheme is that the number of photons collected from one site is huge as compared to maximum one in the original detection scheme. This is due to three reasons. Firstly, we perform a cyclic transition by repeatedly creating and detecting the $|2P/6P\rangle$ excitons. This can be repeated many times within the lifetime of the $|25S\rangle$ exciton as the lifetime of $|2P/6P\rangle$ excitons are much smaller. Secondly, as the size of $|2P/6P\rangle$ excitons are much smaller than the $|25S\rangle$ exciton many $|2P/6P\rangle$ excitons can be excited simultaneously which would result in detection of multiple photons each time. Thirdly, due to this ensemble excitation of $|2P/6P\rangle$ excitons the correspondingly emitted photons would be directional enhancing the photon collection efficiency. Please note that we assumed that exciton linewidths to be radiative here, based on current evidences [129]. Although the contribution of phonon-mediated line broadening in excitons is not completely clear, especially to the lower n values. This may adversely affect the detection efficiency.

We quantify the number of emitted photons from a site in $|g\rangle$ state to show that indeed a very large number of photons are emitted. Lifetime of n^{th} state is proportional to n^3. So, a transition to lower n levels can be repeated many times inside the lifetime of the $|n = 25\rangle$ state ($\sim$ 1953 times to n=2 and $\sim$ 72 times to n=6 state). Moreover, the size of lower lying excitons are much smaller, given by spherical volumes with radius $\langle r_n\rangle = \frac{1}{2}a_B(3n^2 - l(l+1))$, where Bohr radius $a_B = 1.11$ nm and for s excitons $l = 0$ while for p exciton states $l = 1$. This gives a radius of 1040.6 nm for $25S$ state while only 5.6 nm and 58.8 nm for $2P$ and $6P$ states respectively. Assuming we wait for three lifetimes (of P state) to let all the excitons emit, the combined effect of both factors would result in emission of a staggering number of photons, 4.3×10^9 and 1.3×10^5 for $2S$ and $6S$ states respectively. Here, we have considered the exciton radius itself instead of the blockade radius because blockade radius would depend on the choice of detection pulse Rabi frequncy which is flexible. Also, the value of blockade radius generally stays in the same order as the exciton radius.

We estimated the mean photon number above. But to distinguish between the $|g\rangle$ and $|r\rangle$

states by measuring photon number, we need to know the photon number distribution too. We assume the probability to successfully detect a particular exciton by photon detection is P - i.e. combining probabilities of photon emission within the detection time window, within the spatial collection angle and successful detection. If a total N number of excitons are attempted to be detected (in time and space), their distribution is binomial resulting in mean photon detected $\overline{x} = Np$ and variance $\sigma^2 = Np(1-p)$. As binomial distributions are almost Gaussian for high N, to have a vanishing overlap (less than 1%) between the two distribution ($|g\rangle$ and $|r\rangle$) the mean separation needs to be more than 6σ. As $\sigma << \overline{x}$ in our case we can assume both σ and $\overline{x}$ to be almost same for both distribution. A 6σ separation would imply, detection fidelity of 99.9%. We estimate below how much mean separation (i.e. 6σ) is needed as fraction of mean to achieve this. In our case, we have $6\sigma/\overline{x} = 6\sqrt{\frac{1-p}{Np}}$. Using N from above and assuming a photon collection probability of $p = 0.5$ we would have $6\sigma/\overline{x}$ of 0.000091 and 0.017 for n =2 and $n = 6$ cases respectively. Hence, to distinguish $|g\rangle$ and $|r\rangle$ states with 99.9% fidelity we need only 0.0091% (or 1.7%) less photon emitted in case of $|r\rangle$ state than in case of $|g\rangle$ state while using $n = 2$ ($n = 6$) state. This implies that even very small asymmetric Rydberg interaction coefficients would be enough for such detection. We didn't estimate the interaction coefficient for asymmetric interaction here as that is out of the scope of the current work.

We didn't consider the effect of the decay of the Rydberg state on our alternative detection scheme yet. When the Rydberg state decays, the blockade effect goes away and there is no more suppression of photon emission. Hence, it seems best to detect early so that no Rydberg state decays. However, if we don't wait for long enough then there is not enough photons and we can't distinguish as seen above. Hence, there is an optimal time to stop detection which we found out to be 0.5 $\times$ decay time. Decreasing the detection time by half adversely affects the above estimate but not by a lot, especially given the small difference of photon number required in our scheme .

7.4.4 Other Implementation Details

We now discuss several details of our proposal. We chose nS Rydberg states because it offered two important simplifications in tracking the quantum dynamics. nS states have only one angular momentum state $|n00\rangle$ and hence the product state $|n00\rangle|n00\rangle$ is the eigenstate of the non-interacting Hamiltonian [224]. Also, owing to the zero angular momentum nS states doesn't have any angle dependence in Rydberg interaction coefficients. Hence, for a polygon configuration of sites (Fig. 7.1(C)) or even an arbitrary configuration (as explored in Fig. 7.3 for MIS problem) the Rydberg interaction and the corresponding evolution is tractable for nS states (for upto 12 sites using computer systems available to us).

Although nP states can be excited directly by one yellow laser and offer an experimentally simpler scenario, nP states introduce considerable complications in tracking the quantum simulation. This includes angle-dependent Rydberg-Rydberg interaction and difficulty in exciting eigenstates of the Rydberg interaction Hamiltonian, which in this case are mostly entangled states [224].

For these reasons, we choose to address nS states and take advantage of the additional flexibility in the geometry to apply this system to applications such as solving the MIS problem. However, the superposition states holds promise for potential non-trivial many-body quantum dynamics to be explored. In this context, many-body quantum dynamics of Rydberg exciton has recently been explored in [149].

In the proposed experiment, we intend to excite the $n = 25$ excitation with about 1 μm radius and about 3 μm blockade radius. Hence to prevent double excitons occurring along the crystal propagation direction the crystal needs to be rather thin, around 3 μm. It is a challenge to manufacture such small thickness artificial Cu_2O crystals, although artificial Cu_2O micro-crystals has recently been created [145]. Another problem with using a small thickness crystal is that it can change the energy level structure of the excitons, because it is now confined inside a potential well. Considering these issues, a little more thickness would actually probably be fine as the laser itself is focused in about $1 - 2$ μm length at the centre

of the crystal and hence weaker in intensity at the edges, resulting in larger blockade radius there.

There is also a possibility that the excitons could move due to thermal motion despite the very small timescales used. This would be detrimental to our proposal. However, we estimated that in the simulation duration of ~ 0.2 ns and at 1K temperature, even if an exciton moves ideally, uninhibited with its average thermal velocity, it would only travel $\sim 1\ \mu m$. Moreover, in practical systems there is scattering due to crystal imperfection which would further slow down the exciton greatly. Also, the system can be cooled to mK temperatures to constrain the exciton montion even more.

7.5 Conclusions

In conclusion, we simulated many-body Rydberg excitation dynamics in Cu_2O excitons. Despite the detrimental effect of neighboring Rydberg states, we demonstrated that $\mathbb{Z}_2$-ordered phase can be reached and observed using correlation in detected emission. We explored the scaling of the success probability and showed that such many-body quantum states can be reached and observed for over 50 exciton sites at experimental run times two orders of magnitude shorter than the individually trapped Rydberg atoms. Using the ability to selectively excite excitons in an arbitrary configuration, we argued MIS problems can be solved in the Rydberg exciton system. To further scale up the system, we discussed the possibility of improving exciton lifetimes by many orders of magnitude using engineered 2D micro structures. Overall these results show the potential of Cu_2O excitons and other attractive semiconductor systems for Rydberg excitons to be used to simulate many-body dynamics with applications extending to complex optimization problems.

7.6 Acknowledgment

SG acknowledges support through an Alberta Innovates Technology Futures (AITF) Graduate Student Scholarship (GSS), an Izaak Walton Killam Doctoral Scholarship and an Eyes High International Doctoral Scholarship.

Chapter 8

Conclusion and Outlook

The proposals for two different quantum devices given in this thesis were at the junction of photonic technologies and solid-state systems. We proposed a non-destructive photon detection (or QND detection) scheme using rare-earth ion doped crystals. An intense probe pulse is first stored in an ensemble of rare-earth ions inside a nanophotonic cavity. Later a single photon signal passes through the cavity, giving the probe pulse stored in the atoms a phase shift through cross phase modulation. The presence of the stored probe pulse in the cavity complicates the phase-shift significantly, but we showed that non-destructive detection is still possible with high success probabilities.

Several different approaches can be taken to further develop and eventually implement an ensemble based solid state QND detector, working on the principle of cross phase modulation. Both theoretical and experimental efforts may be necessary, especially to create a robust and practical device. Developing long nanophotonic cavities with high quality factors is one of the essential requirements of our proposal. Another direction can be minimising the light coupling loss (or mode matching loss) to the cavities. For small coupling loss light can be sent multiple times through the cavities, thereby increasing the phase shift in such a multipass arrangement. Other solid-state systems can be modeled in search of a more suitable parameter regime. Another direction is building a room temperature (or at

least liquid nitrogen temperature) QND detector which will be more robust and suitable for practical applications. In view of the proposals of spaceborne QND detectors, it may be interesting to consider the requirements for such a device.

The quantum simulation proposal in Rydberg excitons was presented next. Rydberg excitons with large dipole moment and blockade effect were recently discovered in Cu_2O semiconductors. On the other hand, systems of Rydberg atoms are being investigated for their potential application as quantum simulators. Here we have developed a similar proposal specific to the Rydberg excitons, which may prove to be more practical and flexible system on the virtue of being a solid. The exciton system posed its own challenges and advantages which were analysed. The maximum independent set (MIS) problem with an arbitrary configuration of excitons was analysed as an application of the simulator. An alternative high fidelity detection scheme based on asymmetric Rydberg interaction was introduced.

Research in building a quantum simulator or other quantum technologies from Rydberg excitons can take many directions in the future, given the nascent but promising state of the field. Further detailed theoretical modelling of the exciton system is definitely one such direction. More detailed modelling would definitely facilitate research into further understanding the properties and potential applications of the exciton system. More proposals for application of the Rydberg excitons is another direction. Such studies would provide the impetus for both theorists and experimentalists to probe the system in more depth. Rydberg exciton system in Cu_2O has a rich structure. Considering the many possible states and interactions, different quantum simulation scenarios can probably be implemented in this system. These can be modelled for small number of qubits using classical computers or even nascent quantum computers that are slowly becoming commercially available over the cloud.

Bibliography

[1] C. Simon, "Towards a global quantum network," *Nature Photonics*, vol. 11, no. 11, p. 678, 2017.

[2] E. Knill, R. Laflamme, and G. J. Milburn, "A scheme for efficient quantum computation with linear optics," *Nature*, vol. 409, pp. 46–52, Jan. 2001.

[3] J. M. Arrazola, V. Bergholm, K. Brádler, T. R. Bromley, M. J. Collins, I. Dhand, A. Fumagalli, T. Gerrits, A. Goussev, L. G. Helt, J. Hundal, T. Isacsson, R. B. Israel, J. Izaac, S. Jahangiri, R. Janik, N. Killoran, S. P. Kumar, J. Lavoie, A. E. Lita, D. H. Mahler, M. Menotti, B. Morrison, S. W. Nam, L. Neuhaus, H. Y. Qi, N. Quesada, A. Repingon, K. K. Sabapathy, M. Schuld, D. Su, J. Swinarton, A. Száva, K. Tan, P. Tan, V. D. Vaidya, Z. Vernon, Z. Zabaneh, and Y. Zhang, "Quantum circuits with many photons on a programmable nanophotonic chip," *Nature*, vol. 591, pp. 54–60, Mar. 2021.

[4] H.-S. Zhong, H. Wang, Y.-H. Deng, M.-C. Chen, L.-C. Peng, Y.-H. Luo, J. Qin, D. Wu, X. Ding, Y. Hu, P. Hu, X.-Y. Yang, W.-J. Zhang, H. Li, Y. Li, X. Jiang, L. Gan, G. Yang, L. You, Z. Wang, L. Li, N.-L. Liu, C.-Y. Lu, and J.-W. Pan, "Quantum computational advantage using photons," *Science*, vol. 370, pp. 1460–1463, Dec. 2020.

[5] S. Yokoyama, R. Ukai, S. C. Armstrong, C. Sornphiphatphong, T. Kaji, S. Suzuki, J.-i. Yoshikawa, H. Yonezawa, N. C. Menicucci, and A. Furusawa, "Ultra-large-scale

continuous-variable cluster states multiplexed in the time domain," *Nature Photonics*, vol. 7, pp. 982–986, Dec. 2013.

[6] J. L. O'Brien, A. Furusawa, and J. Vučković, "Photonic quantum technologies," *Nature Photonics*, vol. 3, pp. 687–695, Dec. 2009.

[7] H.-S. Zhong, Y.-H. Deng, J. Qin, H. Wang, M.-C. Chen, L.-C. Peng, Y.-H. Luo, D. Wu, S.-Q. Gong, H. Su, Y. Hu, P. Hu, X.-Y. Yang, W.-J. Zhang, H. Li, Y. Li, X. Jiang, L. Gan, G. Yang, L. You, Z. Wang, L. Li, N.-L. Liu, J. J. Renema, C.-Y. Lu, and J.-W. Pan, "Phase-Programmable Gaussian Boson Sampling Using Stimulated Squeezed Light," *Physical Review Letters*, vol. 127, p. 180502, Oct. 2021.

[8] S. Ebadi, T. T. Wang, H. Levine, A. Keesling, G. Semeghini, A. Omran, D. Bluvstein, R. Samajdar, H. Pichler, W. W. Ho, S. Choi, S. Sachdev, M. Greiner, V. Vuletić, and M. D. Lukin, "Quantum phases of matter on a 256-atom programmable quantum simulator," *Nature*, vol. 595, pp. 227–232, July 2021.

[9] P. L. McMahon, A. Marandi, Y. Haribara, R. Hamerly, C. Langrock, S. Tamate, T. Inagaki, H. Takesue, S. Utsunomiya, K. Aihara, R. L. Byer, M. M. Fejer, H. Mabuchi, and Y. Yamamoto, "A fully programmable 100-spin coherent Ising machine with all-to-all connections," *Science*, vol. 354, pp. 614–617, Nov. 2016.

[10] B. Hensen, H. Bernien, A. E. Dréau, A. Reiserer, N. Kalb, M. S. Blok, J. Ruitenberg, R. F. L. Vermeulen, R. N. Schouten, C. Abellán, W. Amaya, V. Pruneri, M. W. Mitchell, M. Markham, D. J. Twitchen, D. Elkouss, S. Wehner, T. H. Taminiau, and R. Hanson, "Loophole-free Bell inequality violation using electron spins separated by 1.3 kilometres," *Nature*, vol. 526, pp. 682–686, Oct. 2015.

[11] M. Pompili, S. L. N. Hermans, S. Baier, H. K. C. Beukers, P. C. Humphreys, R. N. Schouten, R. F. L. Vermeulen, M. J. Tiggelman, L. dos Santos Martins, B. Dirkse,

S. Wehner, and R. Hanson, "Realization of a multinode quantum network of remote solid-state qubits," *Science*, vol. 372, pp. 259–264, Apr. 2021.

[12] H. de Riedmatten, M. Afzelius, M. U. Staudt, C. Simon, and N. Gisin, "A solid-state light–matter interface at the single-photon level," *Nature*, vol. 456, pp. 773–777, Dec. 2008.

[13] F. Arute, K. Arya, R. Babbush, D. Bacon, J. C. Bardin, R. Barends, R. Biswas, S. Boixo, F. G. S. L. Brandao, D. A. Buell, B. Burkett, Y. Chen, Z. Chen, B. Chiaro, R. Collins, W. Courtney, A. Dunsworth, E. Farhi, B. Foxen, A. Fowler, C. Gidney, M. Giustina, R. Graff, K. Guerin, S. Habegger, M. P. Harrigan, M. J. Hartmann, A. Ho, M. Hoffmann, T. Huang, T. S. Humble, S. V. Isakov, E. Jeffrey, Z. Jiang, D. Kafri, K. Kechedzhi, J. Kelly, P. V. Klimov, S. Knysh, A. Korotkov, F. Kostritsa, D. Landhuis, M. Lindmark, E. Lucero, D. Lyakh, S. Mandrà, J. R. McClean, M. McEwen, A. Megrant, X. Mi, K. Michielsen, M. Mohseni, J. Mutus, O. Naaman, M. Neeley, C. Neill, M. Y. Niu, E. Ostby, A. Petukhov, J. C. Platt, C. Quintana, E. G. Rieffel, P. Roushan, N. C. Rubin, D. Sank, K. J. Satzinger, V. Smelyanskiy, K. J. Sung, M. D. Trevithick, A. Vainsencher, B. Villalonga, T. White, Z. J. Yao, P. Yeh, A. Zalcman, H. Neven, and J. M. Martinis, "Quantum supremacy using a programmable superconducting processor," *Nature*, vol. 574, pp. 505–510, Oct. 2019.

[14] Y. Wu, W.-S. Bao, S. Cao, F. Chen, M.-C. Chen, X. Chen, T.-H. Chung, H. Deng, Y. Du, D. Fan, M. Gong, C. Guo, C. Guo, S. Guo, L. Han, L. Hong, H.-L. Huang, Y.-H. Huo, L. Li, N. Li, S. Li, Y. Li, F. Liang, C. Lin, J. Lin, H. Qian, D. Qiao, H. Rong, H. Su, L. Sun, L. Wang, S. Wang, D. Wu, Y. Xu, K. Yan, W. Yang, Y. Yang, Y. Ye, J. Yin, C. Ying, J. Yu, C. Zha, C. Zhang, H. Zhang, K. Zhang, Y. Zhang, H. Zhao, Y. Zhao, L. Zhou, Q. Zhu, C.-Y. Lu, C.-Z. Peng, X. Zhu, and J.-W. Pan, "Strong Quantum Computational Advantage Using a Superconducting Quantum Processor," *Physical Review Letters*, vol. 127, p. 180501, Oct. 2021.

[15] "IBM's new 53-qubit quantum computer is the most powerful machine you can use." MIT Technology Review, URL = https://www.technologyreview.com/2019/09/18/132956/ibms-new-53-qubit-quantum-computer-is-the-most-powerful-machine-you-can-use.

[16] S. Goswami, K. Heshami, and C. Simon, "Theory of cavity-enhanced nondestructive detection of photonic qubits in a solid-state atomic ensemble," *Physical Review A*, vol. 98, p. 043842, Oct. 2018.

[17] J. Taylor, S. Goswami, V. Walther, M. Spanner, C. Simon, and K. Heshami, "Simulation of many-body dynamics using Rydberg excitons," *arXiv:2107.02273 [quant-ph]*, July 2021.

[18] V. B. Braginsky, Y. I. Vorontsov, and K. S. Thorne, "Quantum Nondemolition Measurements," *Science*, vol. 209, pp. 547–557, Aug. 1980.

[19] V. B. Braginsky, V. B. Braginskiĭ, and F. Y. Khalili, *Quantum Measurement*. Cambridge University Press, May 1995.

[20] V. B. Braginsky and F. Y. Khalili, "Quantum nondemolition measurements: the route from toys to tools," *Reviews of Modern Physics*, vol. 68, pp. 1–11, Jan. 1996.

[21] L. Landau and R. Peierls, "Erweiterung des Unbestimmtheitsprinzips für die relativistische Quantentheorie," *Zeitschrift für Physik*, vol. 69, pp. 56–69, Jan. 1931.

[22] J. v. Neumann, *Mathematische Grundlagen der Quantenmechanik*. Springer-Verlag, Mar. 2013.

[23] D. Bohm, *Quantum Theory*. Prentice-Hall International, 2013.

[24] R. L. Stratonovich, "The quantum generalization of optimal statistical estimation and hypothesis testing," *Stochastics*, vol. 1, pp. 87–126, Jan. 1975.

[25] C. W. Helstrom, "Quantum detection and estimation theory," *Journal of Statistical Physics*, vol. 1, pp. 231–252, June 1969.

[26] V. B. Braginskiĭ and Y. I. Vorontsov, "Quantum-mechanical limitations in macroscopic experiments and modern experimental technique," *Soviet Physics Uspekhi*, vol. 17, p. 644, May 1975.

[27] W. G. Unruh, "Analysis of quantum-nondemolition measurement," *Physical Review D*, vol. 18, pp. 1764–1772, Sept. 1978.

[28] K. S. Thorne, R. W. P. Drever, C. M. Caves, M. Zimmermann, and V. D. Sandberg, "Quantum Nondemolition Measurements of Harmonic Oscillators," *Physical Review Letters*, vol. 40, pp. 667–671, Mar. 1978.

[29] M. Tse, H. Yu, N. Kijbunchoo, A. Fernandez-Galiana, P. Dupej, L. Barsotti, C. Blair, D. Brown, S. Dwyer, A. Effler, M. Evans, P. Fritschel, V. Frolov, A. Green, G. Mansell, F. Matichard, N. Mavalvala, D. McClelland, L. McCuller, T. McRae, J. Miller, A. Mullavey, E. Oelker, I. Phinney, D. Sigg, B. Slagmolen, T. Vo, R. Ward, C. Whittle, R. Abbott, C. Adams, R. Adhikari, A. Ananyeva, S. Appert, K. Arai, J. Areeda, Y. Asali, S. Aston, C. Austin, A. Baer, M. Ball, S. Ballmer, S. Banagiri, D. Barker, J. Bartlett, B. Berger, J. Betzwieser, D. Bhattacharjee, G. Billingsley, S. Biscans, R. Blair, N. Bode, P. Booker, R. Bork, A. Bramley, A. Brooks, A. Buikema, C. Cahillane, K. Cannon, X. Chen, A. Ciobanu, F. Clara, S. Cooper, K. Corley, S. Countryman, P. Covas, D. Coyne, L. Datrier, D. Davis, C. Di Fronzo, J. Driggers, T. Etzel, T. Evans, J. Feicht, P. Fulda, M. Fyffe, J. Giaime, K. Giardina, P. Godwin, E. Goetz, S. Gras, C. Gray, R. Gray, A. Gupta, E. Gustafson, R. Gustafson, J. Hanks, J. Hanson, T. Hardwick, R. Hasskew, M. Heintze, A. Helmling-Cornell, N. Holland, J. Jones, S. Kandhasamy, S. Karki, M. Kasprzack, K. Kawabe, P. King, J. Kissel, R. Kumar, M. Landry, B. Lane, B. Lantz, M. Laxen, Y. Lecoeuche, J. Leviton, J. Liu, M. Lormand, A. Lundgren, R. Macas, M. MacInnis, D. Macleod, S. Márka,

Z. Márka, D. Martynov, K. Mason, T. Massinger, R. McCarthy, S. McCormick, J. McIver, G. Mendell, K. Merfeld, E. Merilh, F. Meylahn, T. Mistry, R. Mittleman, G. Moreno, C. Mow-Lowry, S. Mozzon, T. Nelson, P. Nguyen, L. Nuttall, J. Oberling, R. Oram, B. O'Reilly, C. Osthelder, D. Ottaway, H. Overmier, J. Palamos, W. Parker, E. Payne, A. Pele, C. Perez, M. Pirello, H. Radkins, K. Ramirez, J. Richardson, K. Riles, N. Robertson, J. Rollins, C. Romel, J. Romie, M. Ross, K. Ryan, T. Sadecki, E. Sanchez, L. Sanchez, T. Saravanan, R. Savage, D. Schaetzl, R. Schnabel, R. Schofield, E. Schwartz, D. Sellers, T. Shaffer, J. Smith, S. Soni, B. Sorazu, A. Spencer, K. Strain, L. Sun, M. Szczepańczyk, M. Thomas, P. Thomas, K. Thorne, K. Toland, C. Torrie, G. Traylor, A. Urban, G. Vajente, G. Valdes, D. VanderHyde, P. Veitch, K. Venkateswara, G. Venugopalan, A. Viets, C. Vorvick, M. Wade, J. Warner, B. Weaver, R. Weiss, B. Willke, C. Wipf, L. Xiao, H. Yamamoto, M. Yap, H. Yu, L. Zhang, M. Zucker, and J. Zweizig, "Quantum-Enhanced Advanced LIGO Detectors in the Era of Gravitational-Wave Astronomy," *Physical Review Letters*, vol. 123, p. 231107, Dec. 2019.

[30] P. Grangier, J. A. Levenson, and J.-P. Poizat, "Quantum non-demolition measurements in optics," *Nature*, vol. 396, pp. 537–542, Dec. 1998.

[31] N. Imoto, H. A. Haus, and Y. Yamamoto, "Quantum nondemolition measurement of the photon number via the optical Kerr effect," *Physical Review A*, vol. 32, pp. 2287–2292, Oct. 1985.

[32] W. Chen, K. M. Beck, R. Bücker, M. Gullans, M. D. Lukin, H. Tanji-Suzuki, and V. Vuletić, "All-Optical Switch and Transistor Gated by One Stored Photon," *Science*, vol. 341, pp. 768–770, Aug. 2013.

[33] N. Sinclair, K. Heshami, C. Deshmukh, D. Oblak, C. Simon, and W. Tittel, "Proposal and proof-of-principle demonstration of non-destructive detection of photonic qubits using a tm: Linbo3 waveguide," *Nature communications*, vol. 7, p. 13454, 2016.

[34] A. Kuzmich, N. P. Bigelow, and L. Mandel, "Atomic quantum non-demolition measurements and squeezing," *EPL (Europhysics Letters)*, vol. 42, p. 481, June 1998.

[35] A. Lupaşcu, S. Saito, T. Picot, P. C. de Groot, C. J. P. M. Harmans, and J. E. Mooij, "Quantum non-demolition measurement of a superconducting two-level system," *Nature Physics*, vol. 3, pp. 119–123, Feb. 2007.

[36] T. C. Ralph, S. D. Bartlett, J. L. O'Brien, G. J. Pryde, and H. M. Wiseman, "Quantum nondemolition measurements for quantum information," *Physical Review A*, vol. 73, p. 012113, Jan. 2006.

[37] K. Boone, J.-P. Bourgoin, E. Meyer-Scott, K. Heshami, T. Jennewein, and C. Simon, "Entanglement over global distances via quantum repeaters with satellite links," *Physical Review A*, vol. 91, p. 052325, May 2015.

[38] N. C. Jones, R. Van Meter, A. G. Fowler, P. L. McMahon, J. Kim, T. D. Ladd, and Y. Yamamoto, "Layered Architecture for Quantum Computing," *Physical Review X*, vol. 2, p. 031007, July 2012.

[39] K. Nemoto and W. J. Munro, "Nearly deterministic linear optical controlled-not gate," *Physical Review Letters*, vol. 93, no. 25, p. 250502, 2004.

[40] F. Xu, X. Ma, Q. Zhang, H.-K. Lo, and J.-W. Pan, "Secure quantum key distribution with realistic devices," *Reviews of Modern Physics*, vol. 92, p. 025002, May 2020.

[41] S. Wehner, D. Elkouss, and R. Hanson, "Quantum internet: A vision for the road ahead," *Science*, vol. 362, p. eaam9288, Oct. 2018.

[42] H. J. Kimble, "The quantum internet," *Nature*, vol. 453, pp. 1023–1030, June 2008.

[43] D. Gottesman, T. Jennewein, and S. Croke, "Longer-Baseline Telescopes Using Quantum Repeaters," *Physical Review Letters*, vol. 109, p. 070503, Aug. 2012.

[44] P. Kómár, E. M. Kessler, M. Bishof, L. Jiang, A. S. Sørensen, J. Ye, and M. D. Lukin, "A quantum network of clocks," *Nature Physics*, vol. 10, pp. 582–587, Aug. 2014.

[45] J. Yin, Y. Cao, Y.-H. Li, S.-K. Liao, L. Zhang, J.-G. Ren, W.-Q. Cai, W.-Y. Liu, B. Li, H. Dai, G.-B. Li, Q.-M. Lu, Y.-H. Gong, Y. Xu, S.-L. Li, F.-Z. Li, Y.-Y. Yin, Z.-Q. Jiang, M. Li, J.-J. Jia, G. Ren, D. He, Y.-L. Zhou, X.-X. Zhang, N. Wang, X. Chang, Z.-C. Zhu, N.-L. Liu, Y.-A. Chen, C.-Y. Lu, R. Shu, C.-Z. Peng, J.-Y. Wang, and J.-W. Pan, "Satellite-based entanglement distribution over 1200 kilometers," *Science*, vol. 356, pp. 1140–1144, June 2017.

[46] P. Xu, Y. Ma, J.-G. Ren, H.-L. Yong, T. C. Ralph, S.-K. Liao, J. Yin, W.-Y. Liu, W.-Q. Cai, X. Han, H.-N. Wu, W.-Y. Wang, F.-Z. Li, M. Yang, F.-L. Lin, L. Li, N.-L. Liu, Y.-A. Chen, C.-Y. Lu, Y. Chen, J. Fan, C.-Z. Peng, and J.-W. Pan, "Satellite testing of a gravitationally induced quantum decoherence model," *Science*, vol. 366, pp. 132–135, Oct. 2019.

[47] W. K. Wootters and W. H. Zurek, "A single quantum cannot be cloned," *Nature*, vol. 299, pp. 802–803, Oct. 1982.

[48] D. Dieks, "Communication by EPR devices," *Physics Letters A*, vol. 92, pp. 271–272, Nov. 1982.

[49] R. Ursin, F. Tiefenbacher, T. Schmitt-Manderbach, H. Weier, T. Scheidl, M. Lindenthal, B. Blauensteiner, T. Jennewein, J. Perdigues, P. Trojek, B. Ömer, M. Fürst, M. Meyenburg, J. Rarity, Z. Sodnik, C. Barbieri, H. Weinfurter, and A. Zeilinger, "Entanglement-based quantum communication over 144 km," *Nature Physics*, vol. 3, pp. 481–486, July 2007.

[50] A. Boaron, G. Boso, D. Rusca, C. Vulliez, C. Autebert, M. Caloz, M. Perrenoud, G. Gras, F. Bussières, M.-J. Li, D. Nolan, A. Martin, and H. Zbinden, "Secure Quan-

tum Key Distribution over 421 km of Optical Fiber," *Physical Review Letters*, vol. 121, p. 190502, Nov. 2018.

[51] T. Schmitt-Manderbach, H. Weier, M. Fürst, R. Ursin, F. Tiefenbacher, T. Scheidl, J. Perdigues, Z. Sodnik, C. Kurtsiefer, J. G. Rarity, A. Zeilinger, and H. Weinfurter, "Experimental Demonstration of Free-Space Decoy-State Quantum Key Distribution over 144 km," *Physical Review Letters*, vol. 98, p. 010504, Jan. 2007.

[52] N. Sangouard, C. Simon, H. de Riedmatten, and N. Gisin, "Quantum repeaters based on atomic ensembles and linear optics," *Reviews of Modern Physics*, vol. 83, pp. 33–80, Mar. 2011.

[53] H.-J. Briegel, W. Dür, J. I. Cirac, and P. Zoller, "Quantum Repeaters: The Role of Imperfect Local Operations in Quantum Communication," *Physical Review Letters*, vol. 81, pp. 5932–5935, Dec. 1998.

[54] L.-M. Duan, M. D. Lukin, J. I. Cirac, and P. Zoller, "Long-distance quantum communication with atomic ensembles and linear optics," *Nature*, vol. 414, pp. 413–418, Nov. 2001.

[55] M. Zwerger, A. Pirker, V. Dunjko, H. Briegel, and W. Dür, "Long-Range Big Quantum-Data Transmission," *Physical Review Letters*, vol. 120, p. 030503, Jan. 2018.

[56] J. Yin, Y.-H. Li, S.-K. Liao, M. Yang, Y. Cao, L. Zhang, J.-G. Ren, W.-Q. Cai, W.-Y. Liu, S.-L. Li, R. Shu, Y.-M. Huang, L. Deng, L. Li, Q. Zhang, N.-L. Liu, Y.-A. Chen, C.-Y. Lu, X.-B. Wang, F. Xu, J.-Y. Wang, C.-Z. Peng, A. K. Ekert, and J.-W. Pan, "Entanglement-based secure quantum cryptography over 1,120 kilometres," *Nature*, vol. 582, pp. 501–505, June 2020.

[57] J.-G. Ren, P. Xu, H.-L. Yong, L. Zhang, S.-K. Liao, J. Yin, W.-Y. Liu, W.-Q. Cai, M. Yang, L. Li, K.-X. Yang, X. Han, Y.-Q. Yao, J. Li, H.-Y. Wu, S. Wan, L. Liu,

D.-Q. Liu, Y.-W. Kuang, Z.-P. He, P. Shang, C. Guo, R.-H. Zheng, K. Tian, Z.-C. Zhu, N.-L. Liu, C.-Y. Lu, R. Shu, Y.-A. Chen, C.-Z. Peng, J.-Y. Wang, and J.-W. Pan, "Ground-to-satellite quantum teleportation," *Nature*, vol. 549, pp. 70–73, Sept. 2017.

[58] S.-K. Liao, W.-Q. Cai, W.-Y. Liu, L. Zhang, Y. Li, J.-G. Ren, J. Yin, Q. Shen, Y. Cao, Z.-P. Li, F.-Z. Li, X.-W. Chen, L.-H. Sun, J.-J. Jia, J.-C. Wu, X.-J. Jiang, J.-F. Wang, Y.-M. Huang, Q. Wang, Y.-L. Zhou, L. Deng, T. Xi, L. Ma, T. Hu, Q. Zhang, Y.-A. Chen, N.-L. Liu, X.-B. Wang, Z.-C. Zhu, C.-Y. Lu, R. Shu, C.-Z. Peng, J.-Y. Wang, and J.-W. Pan, "Satellite-to-ground quantum key distribution," *Nature*, vol. 549, pp. 43–47, Sept. 2017.

[59] S.-K. Liao, W.-Q. Cai, J. Handsteiner, B. Liu, J. Yin, L. Zhang, D. Rauch, M. Fink, J.-G. Ren, W.-Y. Liu, Y. Li, Q. Shen, Y. Cao, F.-Z. Li, J.-F. Wang, Y.-M. Huang, L. Deng, T. Xi, L. Ma, T. Hu, L. Li, N.-L. Liu, F. Koidl, P. Wang, Y.-A. Chen, X.-B. Wang, M. Steindorfer, G. Kirchner, C.-Y. Lu, R. Shu, R. Ursin, T. Scheidl, C.-Z. Peng, J.-Y. Wang, A. Zeilinger, and J.-W. Pan, "Satellite-Relayed Intercontinental Quantum Network," *Physical Review Letters*, vol. 120, p. 030501, Jan. 2018.

[60] S. Wein, K. Heshami, C. A. Fuchs, H. Krovi, Z. Dutton, W. Tittel, and C. Simon, "Efficiency of an enhanced linear optical Bell-state measurement scheme with realistic imperfections," *Physical Review A*, vol. 94, p. 032332, Sept. 2016.

[61] L. Jiang, J. M. Taylor, and M. D. Lukin, "Fast and robust approach to long-distance quantum communication with atomic ensembles," *Physical Review A*, vol. 76, p. 012301, July 2007.

[62] Z.-B. Chen, B. Zhao, Y.-A. Chen, J. Schmiedmayer, and J.-W. Pan, "Fault-tolerant quantum repeater with atomic ensembles and linear optics," *Physical Review A*, vol. 76, p. 022329, Aug. 2007.

[63] C. Simon, H. de Riedmatten, M. Afzelius, N. Sangouard, H. Zbinden, and N. Gisin, "Quantum Repeaters with Photon Pair Sources and Multimode Memories," *Physical Review Letters*, vol. 98, p. 190503, May 2007.

[64] O. A. Collins, S. D. Jenkins, A. Kuzmich, and T. A. B. Kennedy, "Multiplexed Memory-Insensitive Quantum Repeaters," *Physical Review Letters*, vol. 98, p. 060502, Feb. 2007.

[65] S. D. Barrett and P. Kok, "Efficient high-fidelity quantum computation using matter qubits and linear optics," *Physical Review A*, vol. 71, p. 060310, June 2005.

[66] R. Valivarthi, S. I. Davis, C. Peña, S. Xie, N. Lauk, L. Narváez, J. P. Allmaras, A. D. Beyer, Y. Gim, M. Hussein, G. Iskander, H. L. Kim, B. Korzh, A. Mueller, M. Rominsky, M. Shaw, D. Tang, E. E. Wollman, C. Simon, P. Spentzouris, D. Oblak, N. Sinclair, and M. Spiropulu, "Teleportation Systems Toward a Quantum Internet," *PRX Quantum*, vol. 1, p. 020317, Dec. 2020. Publisher: American Physical Society.

[67] Y. Yu, F. Ma, X.-Y. Luo, B. Jing, P.-F. Sun, R.-Z. Fang, C.-W. Yang, H. Liu, M.-Y. Zheng, X.-P. Xie, W.-J. Zhang, L.-X. You, Z. Wang, T.-Y. Chen, Q. Zhang, X.-H. Bao, and J.-W. Pan, "Entanglement of two quantum memories via fibres over dozens of kilometres," *Nature*, vol. 578, pp. 240–245, Feb. 2020.

[68] J.-P. Bourgoin, E. Meyer-Scott, B. L. Higgins, B. Helou, C. Erven, H. Hübel, B. Kumar, D. Hudson, I. D\textquotesingleSouza, R. Girard, R. Laflamme, and T. Jennewein, "A comprehensive design and performance analysis of low Earth orbit satellite quantum communication," *New Journal of Physics*, vol. 15, p. 023006, Feb. 2013.

[69] C. J. Pugh, J.-F. Lavigne, J.-P. Bourgoin, B. L. Higgins, and T. Jennewein, "Adaptive optics benefit for quantum key distribution uplink from ground to a satellite," *Advanced Optical Technologies*, vol. 9, pp. 263–273, Oct. 2020.

[70] R. Bedington, J. M. Arrazola, and A. Ling, "Progress in satellite quantum key distribution," *npj Quantum Information*, vol. 3, pp. 1–13, Aug. 2017.

[71] C. Bonato, A. Tomaello, V. D. Deppo, G. Naletto, and P. Villoresi, "Feasibility of satellite quantum key distribution," *New Journal of Physics*, vol. 11, p. 045017, Apr. 2009.

[72] M. Toyoshima, H. Takenaka, Y. Shoji, Y. Takayama, Y. Koyama, and H. Kunimori, "Polarization measurements through space-to-ground atmospheric propagation paths by using a highly polarized laser source in space," *Optics Express*, vol. 17, pp. 22333–22340, Dec. 2009.

[73] J. Yin, Y. Cao, Y.-H. Li, J.-G. Ren, S.-K. Liao, L. Zhang, W.-Q. Cai, W.-Y. Liu, B. Li, H. Dai, M. Li, Y.-M. Huang, L. Deng, L. Li, Q. Zhang, N.-L. Liu, Y.-A. Chen, C.-Y. Lu, R. Shu, C.-Z. Peng, J.-Y. Wang, and J.-W. Pan, "Satellite-to-Ground Entanglement-Based Quantum Key Distribution," *Physical Review Letters*, vol. 119, p. 200501, Nov. 2017.

[74] Y.-A. Chen, Q. Zhang, T.-Y. Chen, W.-Q. Cai, S.-K. Liao, J. Zhang, K. Chen, J. Yin, J.-G. Ren, Z. Chen, S.-L. Han, Q. Yu, K. Liang, F. Zhou, X. Yuan, M.-S. Zhao, T.-Y. Wang, X. Jiang, L. Zhang, W.-Y. Liu, Y. Li, Q. Shen, Y. Cao, C.-Y. Lu, R. Shu, J.-Y. Wang, L. Li, N.-L. Liu, F. Xu, X.-B. Wang, C.-Z. Peng, and J.-W. Pan, "An integrated space-to-ground quantum communication network over 4,600 kilometres," *Nature*, vol. 589, pp. 214–219, Jan. 2021.

[75] S. Chen, "Chinese Satellite Relays a Quantum Signal Between Cities," *Wired*.

[76] M. Gündoğan, J. S. Sidhu, V. Henderson, L. Mazzarella, J. Wolters, D. K. L. Oi, and M. Krutzik, "Proposal for space-borne quantum memories for global quantum networking," *npj Quantum Information*, vol. 7, pp. 1–10, Aug. 2021.

[77] L. Liu, D.-S. Lü, W.-B. Chen, T. Li, Q.-Z. Qu, B. Wang, L. Li, W. Ren, Z.-R. Dong, J.-B. Zhao, W.-B. Xia, X. Zhao, J.-W. Ji, M.-F. Ye, Y.-G. Sun, Y.-Y. Yao, D. Song, Z.-G. Liang, S.-J. Hu, D.-H. Yu, X. Hou, W. Shi, H.-G. Zang, J.-F. Xiang, X.-K. Peng, and Y.-Z. Wang, "In-orbit operation of an atomic clock based on laser-cooled 87Rb atoms," *Nature Communications*, vol. 9, p. 2760, July 2018.

[78] D. C. Aveline, J. R. Williams, E. R. Elliott, C. Dutenhoffer, J. R. Kellogg, J. M. Kohel, N. E. Lay, K. Oudrhiri, R. F. Shotwell, N. Yu, and R. J. Thompson, "Observation of Bose–Einstein condensates in an Earth-orbiting research lab," *Nature*, vol. 582, pp. 193–197, June 2020.

[79] M. Zhong, M. P. Hedges, R. L. Ahlefeldt, J. G. Bartholomew, S. E. Beavan, S. M. Wittig, J. J. Longdell, and M. J. Sellars, "Optically addressable nuclear spins in a solid with a six-hour coherence time," *Nature*, vol. 517, pp. 177–180, Jan. 2015.

[80] K. Boone, J.-P. Bourgoin, E. Meyer-Scott, K. Heshami, T. Jennewein, and C. Simon, "Entanglement over global distances via quantum repeaters with satellite links," *Physical Review A*, vol. 91, no. 5, p. 052325, 2015.

[81] D. E. Chang, V. Vuletić, and M. D. Lukin, "Quantum nonlinear optics – photon by photon," *Nature Photonics*, vol. 8, no. 9, pp. 685–694, 2014.

[82] A. Reiserer, S. Ritter, and G. Rempe, "Nondestructive detection of an optical photon," *Science*, vol. 342, no. 6164, pp. 1349–1351, 2013.

[83] M. Saffman, T. G. Walker, and K. Mølmer, "Quantum information with rydberg atoms," *Reviews of Modern Physics*, vol. 82, no. 3, p. 2313, 2010.

[84] H. Schmidt and A. Imamoglu, "Giant kerr nonlinearities obtained by electromagnetically induced transparency," *Optics Letters*, vol. 21, no. 23, pp. 1936–1938, 1996.

[85] M. Hosseini, K. M. Beck, Y. Duan, W. Chen, and V. Vuletić, "Partially nondestructive continuous detection of individual traveling optical photons," *Physical Review Letters*, vol. 116, no. 3, p. 033602, 2016.

[86] A. Feizpour, M. Hallaji, G. Dmochowski, and A. M. Steinberg, "Observation of the nonlinear phase shift due to single post-selected photons," *Nature Physics*, vol. 11, no. 11, pp. 905–909, 2015.

[87] Z.-Y. Liu, Y.-H. Chen, Y.-C. Chen, H.-Y. Lo, P.-J. Tsai, I. A. Yu, Y.-C. Chen, and Y.-F. Chen, "Large cross-phase modulations at the few-photon level," *Phys. Rev. Lett.*, vol. 117, p. 203601, Nov 2016.

[88] T. Zhong, J. M. Kindem, J. G. Bartholomew, J. Rochman, I. Craiciu, E. Miyazono, M. Bettinelli, E. Cavalli, V. Verma, S. W. Nam, *et al.*, "Nanophotonic rare-earth quantum memory with optically controlled retrieval," *Science*, vol. 357, no. 6358, pp. 1392–1395, 2017.

[89] T. Zhong, J. M. Kindem, J. Rochman, and A. Faraon, "Interfacing broadband photonic qubits to on-chip cavity-protected rare-earth ensembles," *Nature communications*, vol. 8, 2017.

[90] J. G. Bartholomew, T. Zhong, J. M. Kindem, R. Lopez-Rios, J. Rochman, I. Craiciu, E. Miyazono, and A. Faraon, "Controlling rare-earth ions in a nanophotonic resonator using the ac stark shift," *arXiv preprint arXiv:1802.06172*, 2018.

[91] A. Dibos, M. Raha, C. Phenicie, and J. Thompson, "Isolating and enhancing the emission of single erbium ions using a silicon nanophotonic cavity," *arXiv preprint arXiv:1711.10368*, 2017.

[92] B. Casabone, J. Benedikter, T. Hümmer, F. Beck, K. d. O. Lima, T. W. Hänsch, A. Ferrier, P. Goldner, H. de Riedmatten, and D. Hunger, "Cavity-enhanced spectroscopy of a few-ion ensemble in eu3+: Y2o3," *arXiv preprint arXiv:1802.06709*, 2018.

[93] C. O'Brien, T. Zhong, A. Faraon, and C. Simon, "Nondestructive photon detection using a single rare-earth ion coupled to a photonic cavity," *Physical Review A*, vol. 94, no. 4, p. 043807, 2016.

[94] W. Chen, K. M. Beck, R. Bücker, M. Gullans, M. D. Lukin, H. Tanji-Suzuki, and V. Vuletić, "All-optical switch and transistor gated by one stored photon," *Science*, vol. 341, no. 6147, pp. 768–770, 2013.

[95] S. Baur, D. Tiarks, G. Rempe, and S. Dürr, "Single-photon switch based on rydberg blockade," *Physical Review Letters*, vol. 112, p. 073901, Feb 2014.

[96] V. Venkataraman, K. Saha, and A. L. Gaeta, "Phase modulation at the few-photon level for weak-nonlinearity-based quantum computing," *Nature Photonics*, vol. 7, no. 2, pp. 138–141, 2013.

[97] K. Heshami, D. G. England, P. C. Humphreys, P. J. Bustard, V. M. Acosta, J. Nunn, and B. J. Sussman, "Quantum memories: emerging applications and recent advances," *Journal of Modern Optics*, vol. 63, no. 20, pp. 2005–2028, 2016.

[98] J. Brendel, N. Gisin, W. Tittel, and H. Zbinden, "Pulsed energy-time entangled twin-photon source for quantum communication," *Phys. Rev. Lett.*, vol. 82, pp. 2594–2597, Mar 1999.

[99] S. H. Autler and C. H. Townes, "Stark effect in rapidly varying fields," *Physical Review*, vol. 100, no. 2, p. 703, 1955.

[100] S.-J. Yang, X.-J. Wang, X.-H. Bao, and J.-W. Pan, "An efficient quantum light–matter interface with sub-second lifetime," *Nature Photonics*, vol. 10, no. 6, pp. 381–384, 2016.

[101] M. Afzelius, C. Simon, H. De Riedmatten, and N. Gisin, "Multimode quantum memory based on atomic frequency combs," *Physical Review A*, vol. 79, no. 5, p. 052329, 2009.

[102] H. De Riedmatten, M. Afzelius, M. U. Staudt, C. Simon, and N. Gisin, "A solid-state light–matter interface at the single-photon level," *Nature*, vol. 456, no. 7223, p. 773, 2008.

[103] M. P. Hedges, J. J. Longdell, Y. Li, and M. J. Sellars, "Efficient quantum memory for light," *Nature*, vol. 465, no. 7301, pp. 1052–1056, 2010.

[104] M. Zhong, M. P. Hedges, R. L. Ahlefeldt, J. G. Bartholomew, S. E. Beavan, S. M. Wittig, J. J. Longdell, and M. J. Sellars, "Optically addressable nuclear spins in a solid with a six-hour coherence time," *Nature*, vol. 517, no. 7533, pp. 177–180, 2015.

[105] A. V. Gorshkov, A. André, M. Fleischhauer, A. S. Sørensen, and M. D. Lukin, "Universal approach to optimal photon storage in atomic media," *Physical Review Letters*, vol. 98, no. 12, p. 123601, 2007.

[106] M. Sabooni, Q. Li, S. Kröll, and L. Rippe, "Efficient quantum memory using a weakly absorbing sample," *Physical Review Letters*, vol. 110, no. 13, p. 133604, 2013.

[107] D. Saunders, J. Munns, T. Champion, C. Qiu, K. Kaczmarek, E. Poem, P. Ledingham, I. Walmsley, and J. Nunn, "Cavity-enhanced room-temperature broadband raman memory," *Physical Review Letters*, vol. 116, no. 9, p. 090501, 2016.

[108] K. Reim, J. Nunn, V. Lorenz, B. Sussman, K. Lee, N. Langford, D. Jaksch, and I. Walmsley, "Towards high-speed optical quantum memories," *Nature Photonics*, vol. 4, no. 4, p. 218, 2010.

[109] T. Zhong, J. M. Kindem, E. Miyazono, and A. Faraon, "Nanophotonic coherent light-matter interfaces based on rare-earth-doped crystals," *Nature communications*, vol. 6, 2015.

[110] T. Zhong, J. Rochman, J. M. Kindem, E. Miyazono, and A. Faraon, "High quality factor nanophotonic resonators in bulk rare-earth doped crystals," *Optics express*, vol. 24, no. 1, pp. 536–544, 2016.

[111] R. Ahlefeldt, D. McAuslan, J. Longdell, N. Manson, and M. Sellars, "Precision measurement of electronic ion-ion interactions between neighboring eu 3+ optical centers," *Physical Review Letters*, vol. 111, no. 24, p. 240501, 2013.

[112] R. Ahlefeldt, M. Hush, and M. Sellars, "Ultranarrow optical inhomogeneous linewidth in a stoichiometric rare-earth crystal," *Physical review letters*, vol. 117, no. 25, p. 250504, 2016.

[113] M. O. Scully and M. S. Zubairy, *Quantum Optics*. Cambridge University Press, 1997.

[114] L.-M. Duan and H. Kimble, "Scalable photonic quantum computation through cavity-assisted interactions," *Physical Review Letters*, vol. 92, no. 12, p. 127902, 2004.

[115] K. Husimi, "Some formal properties of the density matrix," *Proceedings of the Physico-Mathematical Society of Japan. 3rd Series*, vol. 22, no. 4, pp. 264–314, 1940.

[116] G. Wolfowicz, H. Maier-Flaig, R. Marino, A. Ferrier, H. Vezin, J. J. Morton, and P. Goldner, "Coherent storage of microwave excitations in rare-earth nuclear spins," *Physical Review Letters*, vol. 114, no. 17, p. 170503, 2015.

[117] M. Afzelius, M. U. Staudt, H. De Riedmatten, N. Gisin, O. Guillot-Noël, P. Goldner, R. Marino, P. Porcher, E. Cavalli, and M. Bettinelli, "Efficient optical pumping of zeeman spin levels in nd3+: Yvo4," *Journal of Luminescence*, vol. 130, no. 9, pp. 1566–1571, 2010.

[118] S. Hastings-Simon, M. Afzelius, J. Minář, M. Staudt, B. Lauritzen, H. de Riedmatten, N. Gisin, A. Amari, A. Walther, S. Kröll, *et al.*, "Spectral hole-burning spectroscopy in nd 3+: Y v o 4," *Physical Review B*, vol. 77, no. 12, p. 125111, 2008.

[119] H. Choi, M. Heuck, and D. Englund, "Self-similar nanocavity design with ultrasmall mode volume for single-photon nonlinearities," *Physical Review Letters*, vol. 118, no. 22, p. 223605, 2017.

[120] X. Peng, A. Asundi, Y. Chen, and Z. Xiong, "Study of the mechanical properties of nd: Yvo 4 crystal by use of laser interferometry and finite-element analysis," *Applied Optics*, vol. 40, no. 9, pp. 1396–1403, 2001.

[121] "Pi cermaic actuators." `https://www.piceramic.com/en/products/piezoceramic-actuators/linear-actuators/`.

[122] E.-H. Yang, C. Lee, J. Mueller, and T. George, "Leak-tight piezoelectric microvalve for high-pressure gas micropropulsion," *Journal of Microelectromechanical Systems*, vol. 13, no. 5, pp. 799–807, 2004.

[123] D. Judy, J. Pulskamp, R. Polcawich, and L. Currano, "Piezoelectric nanoswitch," in *Micro Electro Mechanical Systems, 2009. MEMS 2009. IEEE 22nd International Conference on*, pp. 591–594, IEEE, 2009.

[124] H. Hua and Y. K. Vohra, "Pressure-induced blueshift of nd 3+ fluorescence emission in yalo 3: Near infrared pressure sensor," *Applied physics letters*, vol. 71, no. 18, pp. 2602–2604, 1997.

[125] R. F. Stebbings, F. B. Dunning, and F. W. Dunning, *Rydberg States of Atoms and Molecules*. Cambridge University Press, Apr. 1983.

[126] T. F. Gallagher, *Rydberg Atoms*. Cambridge Monographs on Atomic, Molecular and Chemical Physics, Cambridge: Cambridge University Press, 1994.

[127] M. Saffman, T. G. Walker, and K. Mølmer, "Quantum information with Rydberg atoms," *Reviews of Modern Physics*, vol. 82, pp. 2313–2363, Aug. 2010.

[128] J. B. Balewski, A. T. Krupp, A. Gaj, D. Peter, H. P. Büchler, R. Löw, S. Hofferberth, and T. Pfau, "Coupling a single electron to a Bose–Einstein condensate," *Nature*, vol. 502, pp. 664–667, Oct. 2013.

[129] T. Kazimierczuk, D. Fröhlich, S. Scheel, H. Stolz, and M. Bayer, "Giant rydberg excitons in the copper oxide cu 2 o," *Nature*, vol. 514, no. 7522, p. 343, 2014.

[130] A. Chernikov, T. C. Berkelbach, H. M. Hill, A. Rigosi, Y. Li, O. B. Aslan, D. R. Reichman, M. S. Hybertsen, and T. F. Heinz, "Exciton Binding Energy and Nonhydrogenic Rydberg Series in Monolayer WS_2," *Physical Review Letters*, vol. 113, p. 076802, Aug. 2014.

[131] H. M. Hill, A. F. Rigosi, C. Roquelet, A. Chernikov, T. C. Berkelbach, D. R. Reichman, M. S. Hybertsen, L. E. Brus, and T. F. Heinz, "Observation of Excitonic Rydberg States in Monolayer MoS2 and WS2 by Photoluminescence Excitation Spectroscopy," *Nano Letters*, vol. 15, pp. 2992–2997, May 2015.

[132] A. Stier, N. Wilson, K. Velizhanin, J. Kono, X. Xu, and S. Crooker, "Magnetooptics of Exciton Rydberg States in a Monolayer Semiconductor," *Physical Review Letters*, vol. 120, p. 057405, Feb. 2018.

[133] A. Farenbruch, D. Fröhlich, H. Stolz, D. R. Yakovlev, and M. Bayer, "Second-harmonic generation of blue series excitons and magnetoexcitons in Cu_2O," *Physical Review B*, vol. 104, p. 075203, Aug. 2021.

[134] E. F. Gross, "Optical spectrum of excitons in the crystal lattice," *Il Nuovo Cimento*, vol. 3, pp. 672–701, Apr. 1956.

[135] H. Matsumoto, K. Saito, M. Hasuo, S. Kono, and N. Nagasawa, "Revived interest on yellow-exciton series in Cu2C: An experimental aspect," *Solid State Communications*, vol. 97, pp. 125–129, Jan. 1996.

[136] J. Mund, D. Fröhlich, D. R. Yakovlev, and M. Bayer, "High-resolution second harmonic generation spectroscopy with femtosecond laser pulses on excitons in Cu_2O," *Physical Review B*, vol. 98, p. 085203, Aug. 2018.

[137] G. M. Kavoulakis, Y.-C. Chang, and G. Baym, "Fine structure of excitons in Cu_2O," *Physical Review B*, vol. 55, pp. 7593–7599, Mar. 1997.

[138] V. Walther, S. O. Krüger, S. Scheel, and T. Pohl, "Interactions between Rydberg excitons in Cu_2O," *Physical Review B*, vol. 98, p. 165201, Oct. 2018.

[139] J. Heckötter, V. Walther, S. Scheel, M. Bayer, T. Pohl, and M. Aßmann, "Asymmetric Rydberg blockade of giant excitons in Cuprous Oxide," *Nature Communications*, vol. 12, p. 3556, June 2021.

[140] J. Heckötter, M. Freitag, D. Fröhlich, M. Aßmann, M. Bayer, M. A. Semina, and M. M. Glazov, "Scaling laws of Rydberg excitons," *Physical Review B*, vol. 96, p. 125142, Sept. 2017.

[141] A. Farenbruch, J. Mund, D. Fröhlich, D. R. Yakovlev, M. Bayer, M. A. Semina, and M. M. Glazov, "Magneto-Stark and Zeeman effect as origin of second harmonic generation of excitons in Cu_2O," *Physical Review B*, vol. 101, p. 115201, Mar. 2020.

[142] S. Zielińska-Raczyńska, D. Ziemkiewicz, and G. Czajkowski, "Electro-optical properties of Rydberg excitons," *Physical Review B*, vol. 94, p. 045205, July 2016.

[143] D. D. Kang, A. Gross, H. Yang, Y. Morita, K. S. Choi, K. Yoshioka, and N. Y. Kim, "Temperature study of Rydberg exciton optical properties in Cu_2O," *Physical Review B*, vol. 103, p. 205203, May 2021.

[144] S. O. Krüger and S. Scheel, "Waveguides for Rydberg excitons in Cu_2O from strain traps," *Physical Review B*, vol. 97, p. 205208, May 2018.

[145] S. Steinhauer, M. A. Versteegh, S. Gyger, A. W. Elshaari, B. Kunert, A. Mysyrowicz, and V. Zwiller, "Rydberg excitons in cu 2 o microcrystals grown on a silicon platform," *Communications Materials*, vol. 1, no. 1, pp. 1–7, 2020.

[146] M. Khazali, K. Heshami, and C. Simon, "Single-photon source based on rydberg exciton blockade," *Journal of Physics B: Atomic, Molecular and Optical Physics*, vol. 50, no. 21, p. 215301, 2017.

[147] D. Ziemkiewicz and S. Zielińska-Raczyńska, "Proposal of tunable Rydberg exciton maser," *Optics Letters*, vol. 43, pp. 3742–3745, Aug. 2018.

[148] V. Walther, R. Johne, and T. Pohl, "Giant optical nonlinearities from Rydberg excitons in semiconductor microcavities," *Nature Communications*, vol. 9, p. 1309, Apr. 2018.

[149] A. Poddubny and M. Glazov, "Topological spin phases of trapped rydberg excitons in cu 2 o," *Physical review letters*, vol. 123, no. 12, p. 126801, 2019.

[150] A. N. Poddubny and M. M. Glazov, "Polarized edge state emission from topological spin phases of trapped Rydberg excitons in Cu_2O," *Physical Review B*, vol. 102, p. 125307, Sept. 2020.

[151] A. Poddubny and M. Glazov, "Topological Spin Phases of Trapped Rydberg Excitons in Cu_2O," *Physical Review Letters*, vol. 123, p. 126801, Sept. 2019.

[152] J. I. Cirac and P. Zoller, "Goals and opportunities in quantum simulation," *Nature Physics*, vol. 8, pp. 264–266, Apr. 2012.

[153] E. Altman, K. R. Brown, G. Carleo, L. D. Carr, E. Demler, C. Chin, B. DeMarco, S. E. Economou, M. A. Eriksson, K.-M. C. Fu, M. Greiner, K. R. Hazzard, R. G. Hulet, A. J. Kollár, B. L. Lev, M. D. Lukin, R. Ma, X. Mi, S. Misra, C. Monroe, K. Murch, Z. Nazario, K.-K. Ni, A. C. Potter, P. Roushan, M. Saffman, M. Schleier-Smith, I. Siddiqi, R. Simmonds, M. Singh, I. Spielman, K. Temme, D. S. Weiss, J. Vučković,

V. Vuletić, J. Ye, and M. Zwierlein, "Quantum Simulators: Architectures and Opportunities," *PRX Quantum*, vol. 2, p. 017003, Feb. 2021.

[154] R. P. Feynman, "Simulating physics with computers," *International Journal of Theoretical Physics*, vol. 21, pp. 467–488, June 1982.

[155] R. Blatt and C. F. Roos, "Quantum simulations with trapped ions," *Nature Physics*, vol. 8, pp. 277–284, Apr. 2012.

[156] S. Lloyd, "Universal Quantum Simulators," *Science*, vol. 273, pp. 1073–1078, Aug. 1996.

[157] H. F. Trotter, "On the Product of Semi-Groups of Operators," *Proceedings of the American Mathematical Society*, vol. 10, no. 4, pp. 545–551, 1959.

[158] D. Jaksch, C. Bruder, J. I. Cirac, C. W. Gardiner, and P. Zoller, "Cold Bosonic Atoms in Optical Lattices," *Physical Review Letters*, vol. 81, pp. 3108–3111, Oct. 1998.

[159] F. Schäfer, T. Fukuhara, S. Sugawa, Y. Takasu, and Y. Takahashi, "Tools for quantum simulation with ultracold atoms in optical lattices," *Nature Reviews Physics*, vol. 2, pp. 411–425, Aug. 2020.

[160] I. Bloch, J. Dalibard, and W. Zwerger, "Many-body physics with ultracold gases," *Reviews of Modern Physics*, vol. 80, pp. 885–964, July 2008.

[161] I. Bloch, J. Dalibard, and S. Nascimbène, "Quantum simulations with ultracold quantum gases," *Nature Physics*, vol. 8, pp. 267–276, Apr. 2012.

[162] M. Lewenstein, A. Sanpera, V. Ahufinger, B. Damski, A. Sen(De), and U. Sen, "Ultracold atomic gases in optical lattices: mimicking condensed matter physics and beyond," *Advances in Physics*, vol. 56, pp. 243–379, Mar. 2007.

[163] N. Navon, S. Nascimbène, F. Chevy, and C. Salomon, "The Equation of State of a Low-Temperature Fermi Gas with Tunable Interactions," *Science*, vol. 328, pp. 729–732, May 2010.

[164] T. Bourdel, L. Khaykovich, J. Cubizolles, J. Zhang, F. Chevy, M. Teichmann, L. Tarruell, S. J. J. M. F. Kokkelmans, and C. Salomon, "Experimental Study of the BEC-BCS Crossover Region in Lithium 6," *Physical Review Letters*, vol. 93, p. 050401, July 2004.

[165] J. T. Stewart, J. P. Gaebler, C. A. Regal, and D. S. Jin, "Potential Energy of a ^{40}K Fermi Gas in the BCS-BEC Crossover," *Physical Review Letters*, vol. 97, p. 220406, Nov. 2006.

[166] G. E. Astrakharchik, R. Combescot, X. Leyronas, and S. Stringari, "Equation of State and Collective Frequencies of a Trapped Fermi Gas Along the BEC-Unitarity Crossover," *Physical Review Letters*, vol. 95, p. 030404, July 2005.

[167] C. Chin, R. Grimm, P. Julienne, and E. Tiesinga, "Feshbach resonances in ultracold gases," *Reviews of Modern Physics*, vol. 82, pp. 1225–1286, Apr. 2010.

[168] J. Bardeen, L. N. Cooper, and J. R. Schrieffer, "Theory of Superconductivity," *Physical Review*, vol. 108, pp. 1175–1204, Dec. 1957.

[169] C. Gross and I. Bloch, "Quantum simulations with ultracold atoms in optical lattices," *Science*, vol. 357, pp. 995–1001, Sept. 2017.

[170] M. Greiner, I. Bloch, O. Mandel, T. W. Hänsch, and T. Esslinger, "Exploring Phase Coherence in a 2D Lattice of Bose-Einstein Condensates," *Physical Review Letters*, vol. 87, p. 160405, Oct. 2001.

[171] C. Becker, P. Soltan-Panahi, J. Kronjäger, S. Dörscher, K. Bongs, and K. Sengstock, "Ultracold quantum gases in triangular optical lattices," *New Journal of Physics*, vol. 12, p. 065025, June 2010.

[172] G.-B. Jo, J. Guzman, C. K. Thomas, P. Hosur, A. Vishwanath, and D. M. Stamper-Kurn, "Ultracold Atoms in a Tunable Optical Kagome Lattice," *Physical Review Letters*, vol. 108, p. 045305, Jan. 2012.

[173] F. Grossmann, T. Dittrich, P. Jung, and P. Hänggi, "Coherent destruction of tunneling," *Physical Review Letters*, vol. 67, pp. 516–519, July 1991.

[174] J. Struck, C. Ölschläger, R. Le Targat, P. Soltan-Panahi, A. Eckardt, M. Lewenstein, P. Windpassinger, and K. Sengstock, "Quantum Simulation of Frustrated Classical Magnetism in Triangular Optical Lattices," *Science*, vol. 333, pp. 996–999, Aug. 2011.

[175] M. Greiner, O. Mandel, T. Esslinger, T. W. Hänsch, and I. Bloch, "Quantum phase transition from a superfluid to a Mott insulator in a gas of ultracold atoms," *Nature*, vol. 415, pp. 39–44, Jan. 2002.

[176] J. F. Sherson, C. Weitenberg, M. Endres, M. Cheneau, I. Bloch, and S. Kuhr, "Single-atom-resolved fluorescence imaging of an atomic Mott insulator," *Nature*, vol. 467, pp. 68–72, Sept. 2010.

[177] W. S. Bakr, A. Peng, M. E. Tai, R. Ma, J. Simon, J. I. Gillen, S. Fölling, L. Pollet, and M. Greiner, "Probing the Superfluid–to–Mott Insulator Transition at the Single-Atom Level," *Science*, vol. 329, pp. 547–550, July 2010.

[178] A. Eckardt, C. Weiss, and M. Holthaus, "Superfluid-Insulator Transition in a Periodically Driven Optical Lattice," *Physical Review Letters*, vol. 95, p. 260404, Dec. 2005.

[179] S. Kuhr, "Quantum-gas microscopes: a new tool for cold-atom quantum simulators," *National Science Review*, vol. 3, pp. 170–172, June 2016.

[180] K. D. Nelson, X. Li, and D. S. Weiss, "Imaging single atoms in a three-dimensional array," *Nature Physics*, vol. 3, pp. 556–560, Aug. 2007.

[181] H. Bernien, S. Schwartz, A. Keesling, H. Levine, A. Omran, H. Pichler, S. Choi, A. S. Zibrov, M. Endres, M. Greiner, *et al.*, "Probing many-body dynamics on a 51-atom quantum simulator," *Nature*, vol. 551, no. 7682, p. 579, 2017.

[182] R. Islam, C. Senko, W. C. Campbell, S. Korenblit, J. Smith, A. Lee, E. E. Edwards, C.-C. J. Wang, J. K. Freericks, and C. Monroe, "Emergence and Frustration of Magnetism with Variable-Range Interactions in a Quantum Simulator," *Science*, vol. 340, pp. 583–587, May 2013.

[183] T. Monz, P. Schindler, J. T. Barreiro, M. Chwalla, D. Nigg, W. A. Coish, M. Harlander, W. Hänsel, M. Hennrich, and R. Blatt, "14-Qubit Entanglement: Creation and Coherence," *Physical Review Letters*, vol. 106, p. 130506, Mar. 2011.

[184] R. Blatt and D. Wineland, "Entangled states of trapped atomic ions," *Nature*, vol. 453, pp. 1008–1015, June 2008.

[185] C. Schneider, D. Porras, and T. Schaetz, "Experimental quantum simulations of many-body physics with trapped ions," *Reports on Progress in Physics*, vol. 75, p. 024401, Jan. 2012.

[186] K. Mølmer and A. Sørensen, "Multiparticle Entanglement of Hot Trapped Ions," *Physical Review Letters*, vol. 82, pp. 1835–1838, Mar. 1999.

[187] J. I. Cirac and P. Zoller, "Quantum Computations with Cold Trapped Ions," *Physical Review Letters*, vol. 74, pp. 4091–4094, May 1995.

[188] A. H. Myerson, D. J. Szwer, S. C. Webster, D. T. C. Allcock, M. J. Curtis, G. Imreh, J. A. Sherman, D. N. Stacey, A. M. Steane, and D. M. Lucas, "High-Fidelity Readout of Trapped-Ion Qubits," *Physical Review Letters*, vol. 100, p. 200502, May 2008.

[189] R. Islam, E. E. Edwards, K. Kim, S. Korenblit, C. Noh, H. Carmichael, G.-D. Lin, L.-M. Duan, C.-C. Joseph Wang, J. K. Freericks, and C. Monroe, "Onset of a quantum

phase transition with a trapped ion quantum simulator," *Nature Communications*, vol. 2, p. 377, July 2011.

[190] K. Kim, S. Korenblit, R. Islam, E. E. Edwards, M.-S. Chang, C. Noh, H. Carmichael, G.-D. Lin, L.-M. Duan, C. C. J. Wang, J. K. Freericks, and C. Monroe, "Quantum simulation of the transverse Ising model with trapped ions," *New Journal of Physics*, vol. 13, p. 105003, Oct. 2011.

[191] J. W. Britton, B. C. Sawyer, A. C. Keith, C.-C. J. Wang, J. K. Freericks, H. Uys, M. J. Biercuk, and J. J. Bollinger, "Engineered two-dimensional Ising interactions in a trapped-ion quantum simulator with hundreds of spins," *Nature*, vol. 484, pp. 489–492, Apr. 2012.

[192] L. Lamata, J. León, T. Schätz, and E. Solano, "Dirac Equation and Quantum Relativistic Effects in a Single Trapped Ion," *Physical Review Letters*, vol. 98, p. 253005, June 2007.

[193] R. Schützhold, M. Uhlmann, L. Petersen, H. Schmitz, A. Friedenauer, and T. Schätz, "Analogue of Cosmological Particle Creation in an Ion Trap," *Physical Review Letters*, vol. 99, p. 201301, Nov. 2007.

[194] R. Gerritsma, G. Kirchmair, F. Zähringer, E. Solano, R. Blatt, and C. F. Roos, "Quantum simulation of the Dirac equation," *Nature*, vol. 463, pp. 68–71, Jan. 2010.

[195] R. Gerritsma, B. P. Lanyon, G. Kirchmair, F. Zähringer, C. Hempel, J. Casanova, J. J. García-Ripoll, E. Solano, R. Blatt, and C. F. Roos, "Quantum Simulation of the Klein Paradox with Trapped Ions," *Physical Review Letters*, vol. 106, p. 060503, Feb. 2011.

[196] V. Nebendahl, H. Häffner, and C. F. Roos, "Optimal control of entangling operations for trapped-ion quantum computing," *Physical Review A*, vol. 79, p. 012312, Jan. 2009.

[197] B. P. Lanyon, C. Hempel, D. Nigg, M. Müller, R. Gerritsma, F. Zähringer, P. Schindler, J. T. Barreiro, M. Rambach, G. Kirchmair, M. Hennrich, P. Zoller, R. Blatt, and C. F. Roos, "Universal Digital Quantum Simulation with Trapped Ions," *Science*, vol. 334, pp. 57–61, Oct. 2011.

[198] A. A. Houck, H. E. Türeci, and J. Koch, "On-chip quantum simulation with superconducting circuits," *Nature Physics*, vol. 8, pp. 292–299, Apr. 2012.

[199] G. Wendin, "Quantum information processing with superconducting circuits: a review," *Reports on Progress in Physics*, vol. 80, p. 106001, Sept. 2017.

[200] X. Gu, A. F. Kockum, A. Miranowicz, Y.-x. Liu, and F. Nori, "Microwave photonics with superconducting quantum circuits," *Physics Reports*, vol. 718-719, pp. 1–102, Nov. 2017.

[201] R. Ma, B. Saxberg, C. Owens, N. Leung, Y. Lu, J. Simon, and D. I. Schuster, "A dissipatively stabilized Mott insulator of photons," *Nature*, vol. 566, pp. 51–57, Feb. 2019.

[202] M. H. Michael, M. Silveri, R. Brierley, V. V. Albert, J. Salmilehto, L. Jiang, and S. Girvin, "New Class of Quantum Error-Correcting Codes for a Bosonic Mode," *Physical Review X*, vol. 6, p. 031006, July 2016.

[203] M. Ganzhorn, D. Egger, P. Barkoutsos, P. Ollitrault, G. Salis, N. Moll, M. Roth, A. Fuhrer, P. Mueller, S. Woerner, I. Tavernelli, and S. Filipp, "Gate-Efficient Simulation of Molecular Eigenstates on a Quantum Computer," *Physical Review Applied*, vol. 11, p. 044092, Apr. 2019.

[204] M. Saffman, T. G. Walker, and K. Mølmer, "Quantum information with rydberg atoms," *Reviews of Modern Physics*, vol. 82, no. 3, p. 2313, 2010.

[205] N. Šibalić and C. S. Adams, *Rydberg Physics*. 2399-2891, IOP Publishing, 2018.

[206] E. Urban, T. A. Johnson, T. Henage, L. Isenhower, D. Yavuz, T. Walker, and M. Saffman, "Observation of rydberg blockade between two atoms," *Nature Physics*, vol. 5, no. 2, p. 110, 2009.

[207] A. Gaëtan, Y. Miroshnychenko, T. Wilk, A. Chotia, M. Viteau, D. Comparat, P. Pillet, A. Browaeys, and P. Grangier, "Observation of collective excitation of two individual atoms in the rydberg blockade regime," *Nature Physics*, vol. 5, no. 2, p. 115, 2009.

[208] T. Peyronel, O. Firstenberg, Q.-Y. Liang, S. Hofferberth, A. V. Gorshkov, T. Pohl, M. D. Lukin, and V. Vuletić, "Quantum nonlinear optics with single photons enabled by strongly interacting atoms," *Nature*, vol. 488, no. 7409, p. 57, 2012.

[209] M. Müller, A. Kölle, R. Löw, T. Pfau, T. Calarco, and S. Montangero, "Room-temperature rydberg single-photon source," *Physical Review A*, vol. 87, no. 5, p. 053412, 2013.

[210] D. Paredes-Barato and C. Adams, "All-optical quantum information processing using rydberg gates," *Physical review letters*, vol. 112, no. 4, p. 040501, 2014.

[211] H. Gorniaczyk, C. Tresp, J. Schmidt, H. Fedder, and S. Hofferberth, "Single-photon transistor mediated by interstate rydberg interactions," *Physical review letters*, vol. 113, no. 5, p. 053601, 2014.

[212] P. Kómár, T. Topcu, E. Kessler, A. Derevianko, V. Vuletić, J. Ye, and M. Lukin, "Quantum network of atom clocks: A possible implementation with neutral atoms," *Physical review letters*, vol. 117, no. 6, p. 060506, 2016.

[213] Y. Han, B. He, K. Heshami, C.-Z. Li, and C. Simon, "Quantum repeaters based on rydberg-blockade-coupled atomic ensembles," *Physical Review A*, vol. 81, no. 5, p. 052311, 2010.

[214] B. Zhao, M. Müller, K. Hammerer, and P. Zoller, "Efficient quantum repeater based on deterministic rydberg gates," *Phys. Rev. A*, vol. 81, p. 052329, May 2010.

[215] A. Keesling, A. Omran, H. Levine, H. Bernien, H. Pichler, S. Choi, R. Samajdar, S. Schwartz, P. Silvi, S. Sachdev, *et al.*, "Quantum kibble–zurek mechanism and critical dynamics on a programmable rydberg simulator," *Nature*, vol. 568, no. 7751, p. 207, 2019.

[216] A. Omran, H. Levine, A. Keesling, G. Semeghini, T. T. Wang, S. Ebadi, H. Bernien, A. S. Zibrov, H. Pichler, S. Choi, *et al.*, "Generation and manipulation of schr\" odinger cat states in rydberg atom arrays," *Science*, vol. 365, pp. 570–574, 2019.

[217] H. Pichler, S.-T. Wang, L. Zhou, S. Choi, and M. D. Lukin, "Quantum optimization for maximum independent set using rydberg atom arrays," *arXiv preprint arXiv:1808.10816*, 2018.

[218] V. Walther, R. Johne, and T. Pohl, "Giant optical nonlinearities from rydberg excitons in semiconductor microcavities," *Nature communications*, vol. 9, no. 1, pp. 1–6, 2018.

[219] C. Uihlein, D. Fröhlich, and R. Kenklies, "Investigation of exciton fine structure in Cu_2O," *Phys. Rev. B*, vol. 23, pp. 2731–2740, Mar 1981.

[220] V. Walther, P. Grünwald, and T. Pohl, "Controlling exciton-phonon interactions via electromagnetically induced transparency," *Phys. Rev. Lett.*, vol. 125, p. 173601, Oct 2020.

[221] F. Schöne, H. Stolz, and N. Naka, "Phonon-assisted absorption of excitons in Cu_2O," *Phys. Rev. B*, vol. 96, p. 115207, Sep 2017.

[222] C. Uihlein, D. Fröhlich, and R. Kenklies, "Investigation of exciton fine structure in cu 2 o," *Physical Review B*, vol. 23, no. 6, p. 2731, 1981.

[223] J. Heckötter, V. Walther, S. Scheel, M. Bayer, T. Pohl, and M. Aßmann, "Asymmetric rydberg blockade of giant excitons in cuprous oxide," *arXiv preprint arXiv:2010.15459*, 2020.

[224] V. Walther, S. O. Krüger, S. Scheel, and T. Pohl, "Interactions between rydberg excitons in Cu_2O," *Physical Review B*, vol. 98, no. 16, p. 165201, 2018.

[225] H. Pichler, S.-T. Wang, L. Zhou, S. Choi, and M. D. Lukin, "Computational complexity of the rydberg blockade in two dimensions," *arXiv preprint arXiv:1809.04954*, 2018.

[226] Z. Wang, D. A. Rhodes, K. Watanabe, T. Taniguchi, J. C. Hone, J. Shan, and K. F. Mak, "Evidence of high-temperature exciton condensation in two-dimensional atomic double layers," *Nature*, vol. 574, no. 7776, pp. 76–80, 2019.

[227] A. Montblanch, D. Kara, I. Paradeisanos, C. Purser, G. Wang, P. Latawiec, M. Loncar, S. Tongay, A. Ferrari, and M. Atature, "Confinement of long-lived interlayer excitons in wse 2/ws 2 heterobilayers," *Bulletin of the American Physical Society*, 2020.

[228] S. O. Krüger and S. Scheel, "Waveguides for rydberg excitons in cu 2 o from strain traps," *Physical Review B*, vol. 97, no. 20, p. 205208, 2018.

Appendix A

Copyright permissions

The copyright permission from Journal and permissions from different co-authors to include the two papers in the thesis are attached below.

Copyright permission for the different figures are also included. Moreover, corresponding references are duly cited in the respective figure captions.

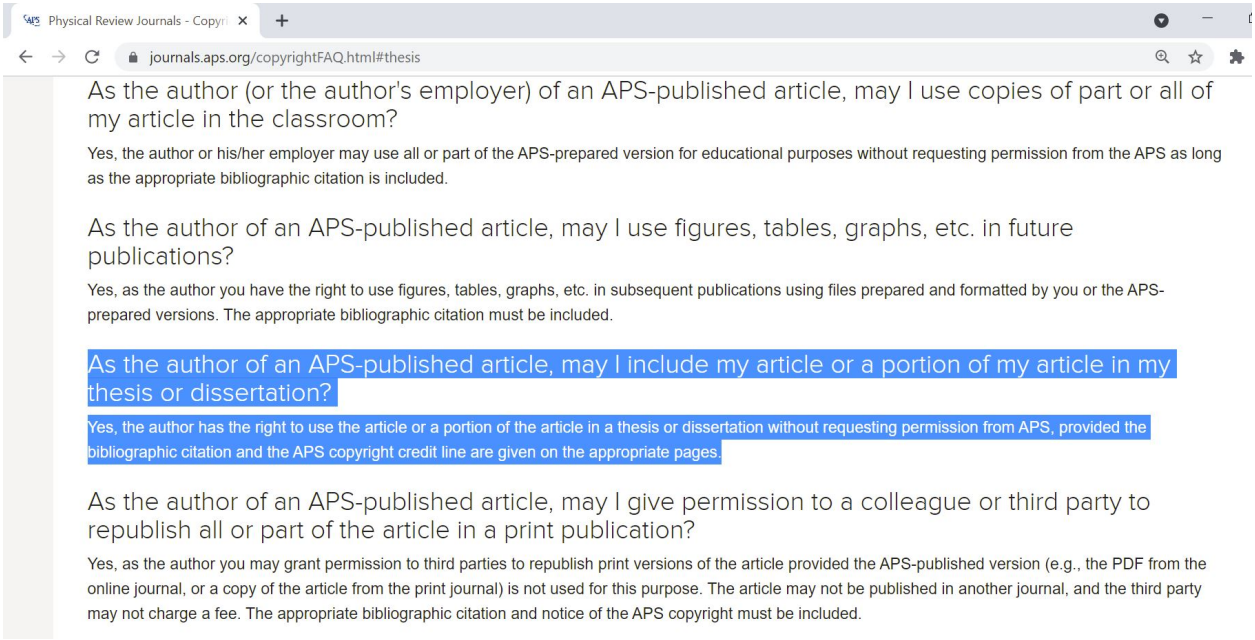

Figure A.1: Permission from Physical Review A to include the first paper in my thesis.

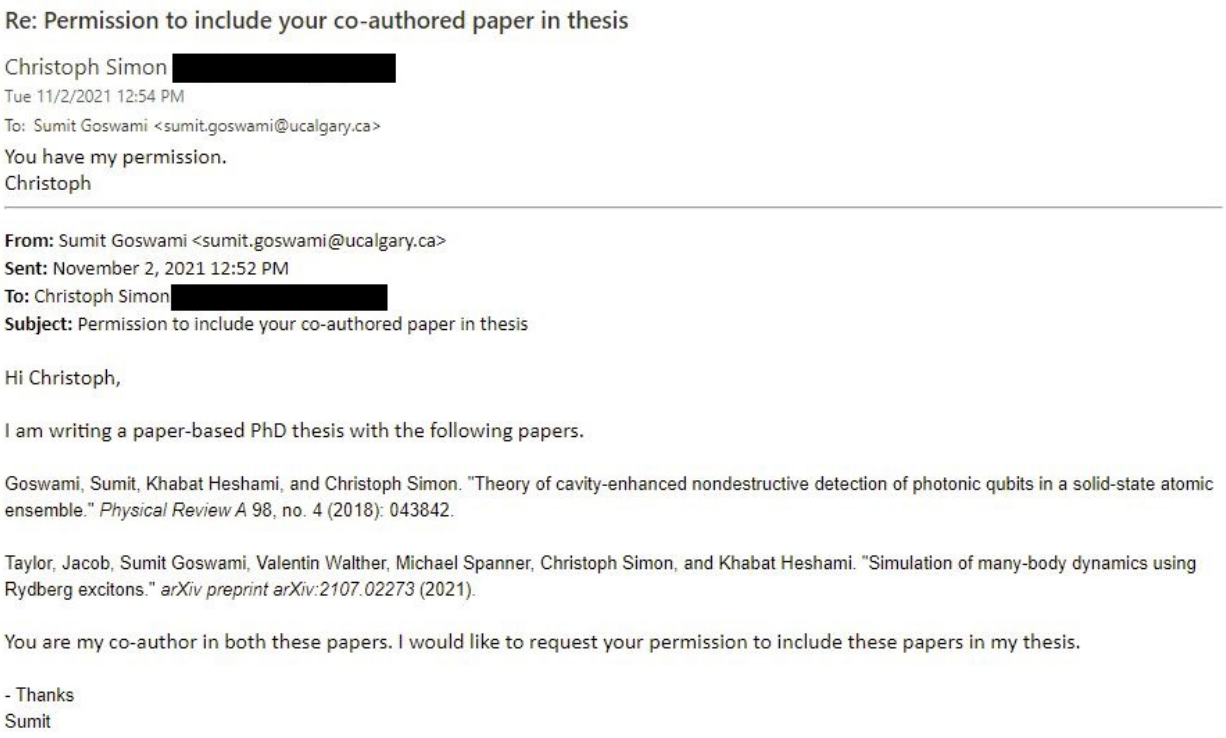

Re: Permission to include your co-authored paper in thesis

Christoph Simon [redacted]
Tue 11/2/2021 12:54 PM
To: Sumit Goswami <sumit.goswami@ucalgary.ca>
You have my permission.
Christoph

From: Sumit Goswami <sumit.goswami@ucalgary.ca>
Sent: November 2, 2021 12:52 PM
To: Christoph Simon [redacted]
Subject: Permission to include your co-authored paper in thesis

Hi Christoph,

I am writing a paper-based PhD thesis with the following papers.

Goswami, Sumit, Khabat Heshami, and Christoph Simon. "Theory of cavity-enhanced nondestructive detection of photonic qubits in a solid-state atomic ensemble." *Physical Review A* 98, no. 4 (2018): 043842.

Taylor, Jacob, Sumit Goswami, Valentin Walther, Michael Spanner, Christoph Simon, and Khabat Heshami. "Simulation of many-body dynamics using Rydberg excitons." *arXiv preprint arXiv:2107.02273* (2021).

You are my co-author in both these papers. I would like to request your permission to include these papers in my thesis.

- Thanks
Sumit

Figure A.2: Permission granted by Dr. Christoph Simon to include our jointly co-authored papers in the thesis.

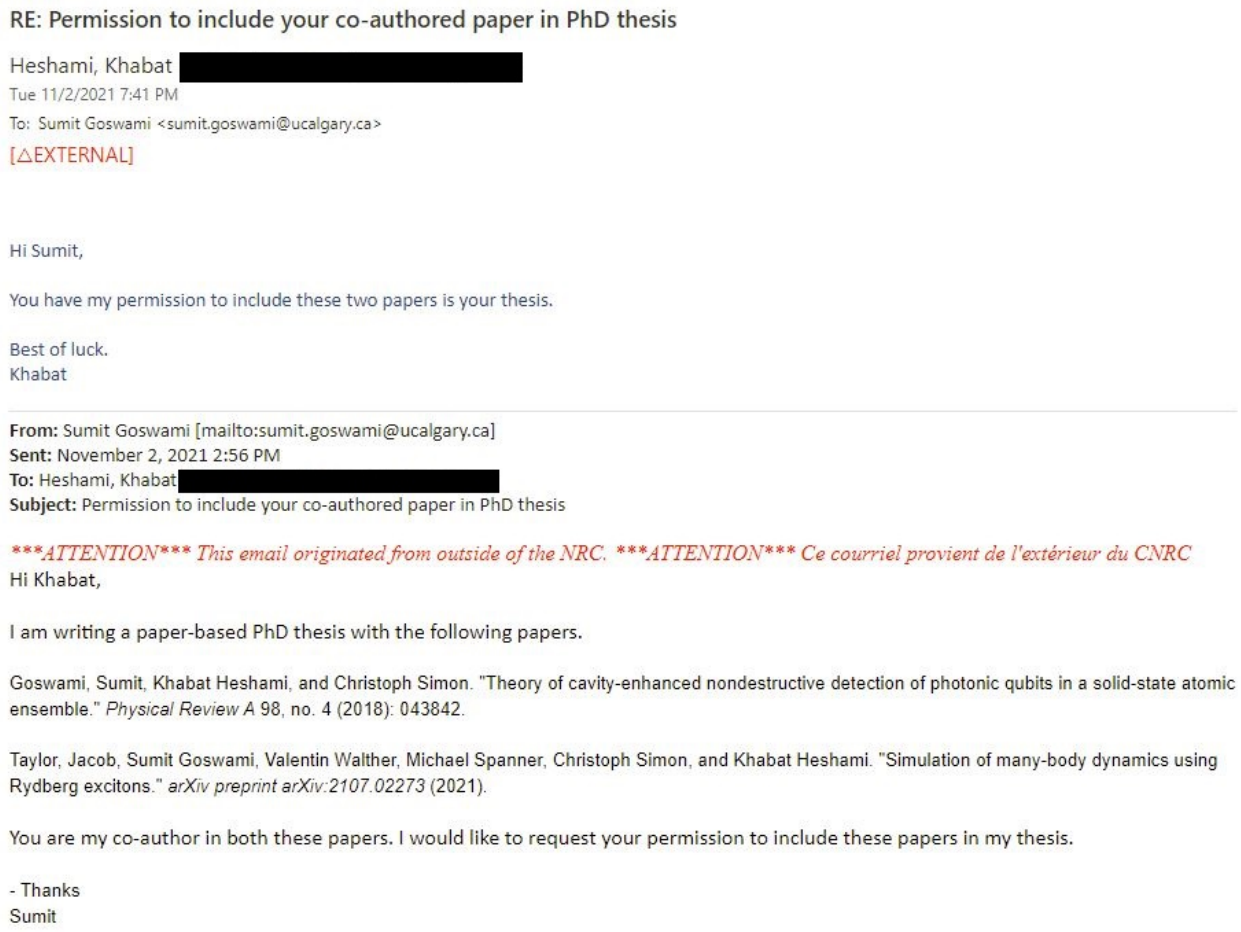

RE: Permission to include your co-authored paper in PhD thesis

Heshami, Khabat [redacted]
Tue 11/2/2021 7:41 PM
To: Sumit Goswami <sumit.goswami@ucalgary.ca>
[△EXTERNAL]

Hi Sumit,

You have my permission to include these two papers is your thesis.

Best of luck.
Khabat

From: Sumit Goswami [mailto:sumit.goswami@ucalgary.ca]
Sent: November 2, 2021 2:56 PM
To: Heshami, Khabat [redacted]
Subject: Permission to include your co-authored paper in PhD thesis

****ATTENTION*** This email originated from outside of the NRC. ***ATTENTION*** Ce courriel provient de l'extérieur du CNRC*
Hi Khabat,

I am writing a paper-based PhD thesis with the following papers.

Goswami, Sumit, Khabat Heshami, and Christoph Simon. "Theory of cavity-enhanced nondestructive detection of photonic qubits in a solid-state atomic ensemble." *Physical Review A* 98, no. 4 (2018): 043842.

Taylor, Jacob, Sumit Goswami, Valentin Walther, Michael Spanner, Christoph Simon, and Khabat Heshami. "Simulation of many-body dynamics using Rydberg excitons." *arXiv preprint arXiv:2107.02273* (2021).

You are my co-author in both these papers. I would like to request your permission to include these papers in my thesis.

- Thanks
Sumit

Figure A.3: Permission granted by Dr. Khabat Heshami to include our jointly co-authored papers in the thesis.

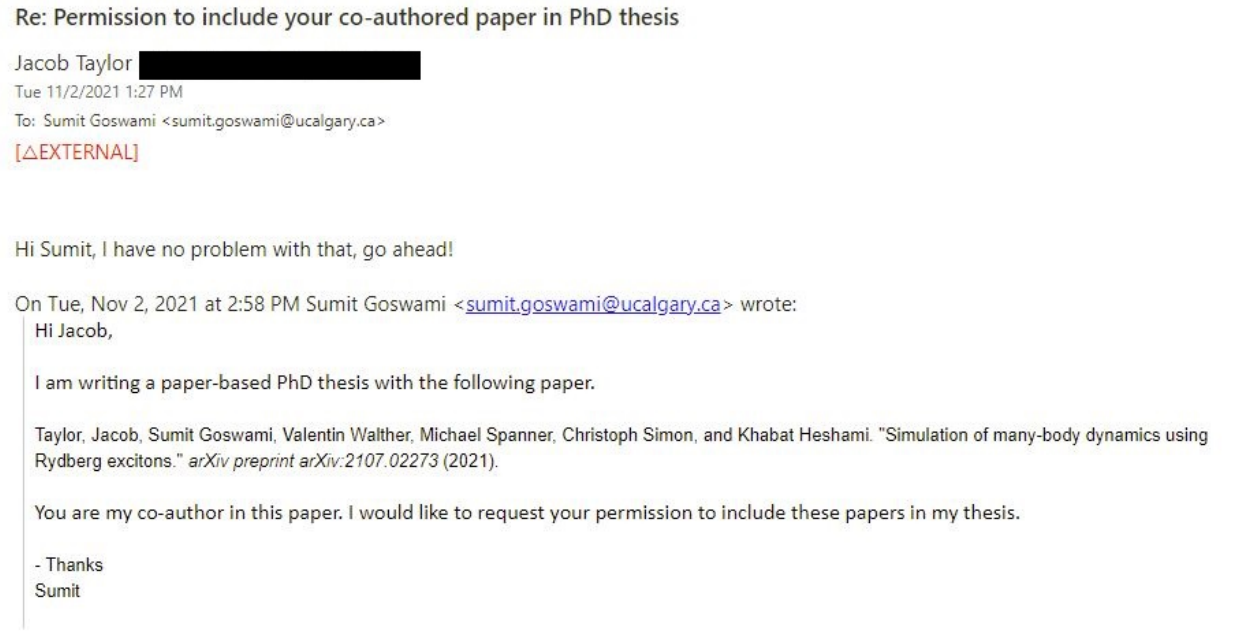

Re: Permission to include your co-authored paper in PhD thesis

Jacob Taylor [redacted]
Tue 11/2/2021 1:27 PM
To: Sumit Goswami <sumit.goswami@ucalgary.ca>
[△EXTERNAL]

Hi Sumit, I have no problem with that, go ahead!

On Tue, Nov 2, 2021 at 2:58 PM Sumit Goswami <sumit.goswami@ucalgary.ca> wrote:

> Hi Jacob,
>
> I am writing a paper-based PhD thesis with the following paper.
>
> Taylor, Jacob, Sumit Goswami, Valentin Walther, Michael Spanner, Christoph Simon, and Khabat Heshami. "Simulation of many-body dynamics using Rydberg excitons." *arXiv preprint arXiv:2107.02273* (2021).
>
> You are my co-author in this paper. I would like to request your permission to include these papers in my thesis.
>
> - Thanks
> Sumit

Figure A.4: Permission granted by Jacob Taylor to include our jointly co-authored paper in the thesis.

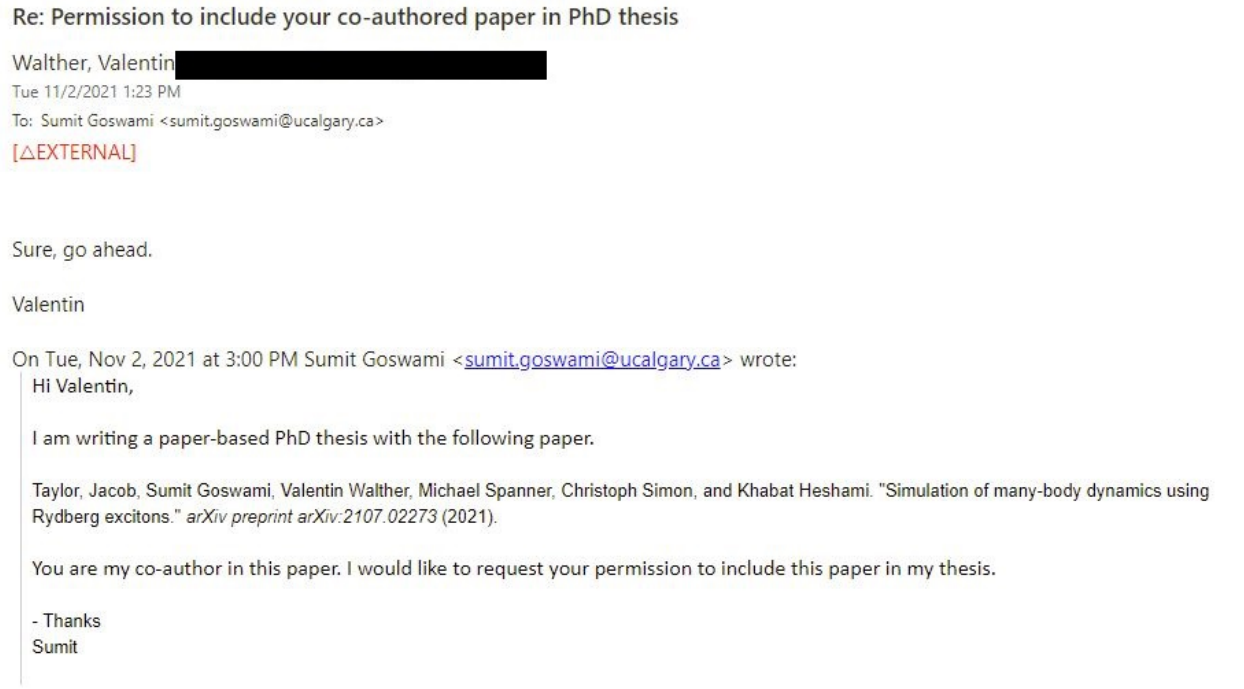

Re: Permission to include your co-authored paper in PhD thesis

Walther, Valentin [redacted]
Tue 11/2/2021 1:23 PM
To: Sumit Goswami <sumit.goswami@ucalgary.ca>
[△EXTERNAL]

Sure, go ahead.

Valentin

On Tue, Nov 2, 2021 at 3:00 PM Sumit Goswami <sumit.goswami@ucalgary.ca> wrote:

> Hi Valentin,
>
> I am writing a paper-based PhD thesis with the following paper.
>
> Taylor, Jacob, Sumit Goswami, Valentin Walther, Michael Spanner, Christoph Simon, and Khabat Heshami. "Simulation of many-body dynamics using Rydberg excitons." *arXiv preprint arXiv:2107.02273* (2021).
>
> You are my co-author in this paper. I would like to request your permission to include this paper in my thesis.
>
> - Thanks
> Sumit

Figure A.5: Permission granted by Dr. Valentin Walther to include our jointly co-authored paper in the thesis.

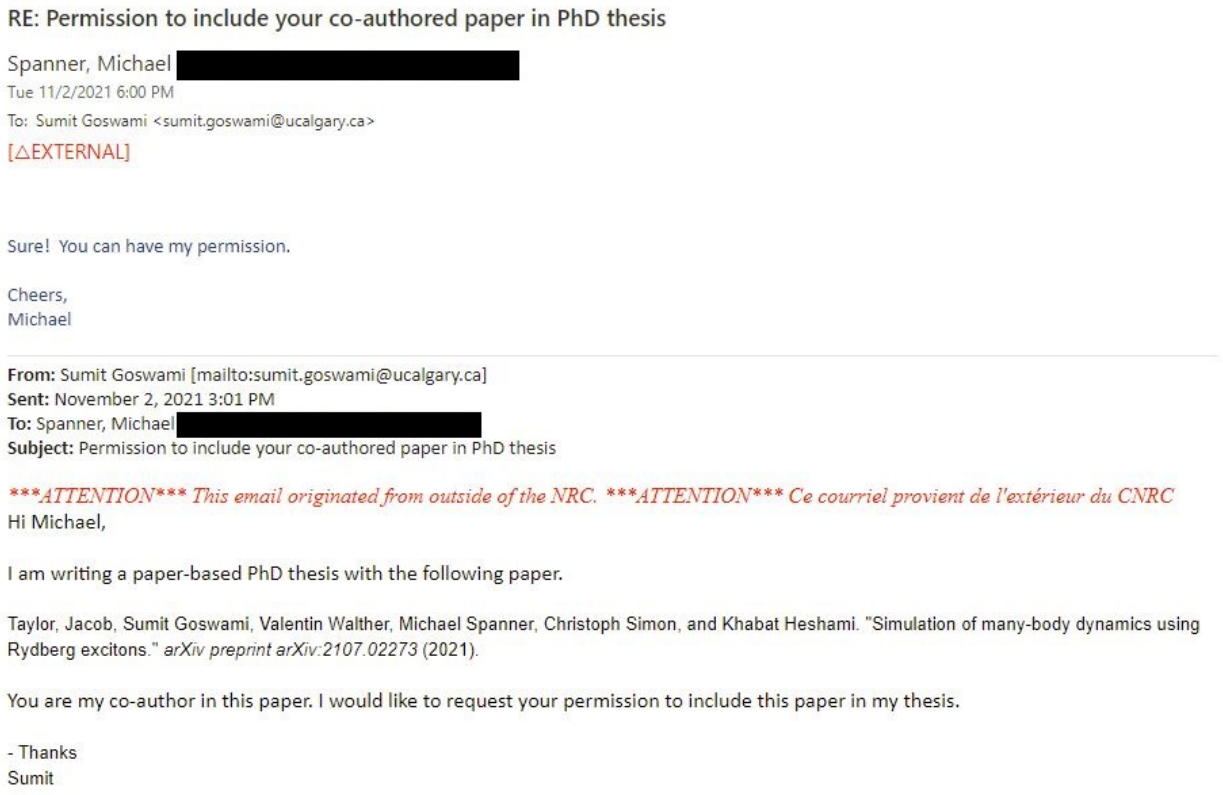

RE: Permission to include your co-authored paper in PhD thesis

Spanner, Michael [redacted]
Tue 11/2/2021 6:00 PM
To: Sumit Goswami <sumit.goswami@ucalgary.ca>
[△EXTERNAL]

Sure! You can have my permission.

Cheers,
Michael

From: Sumit Goswami [mailto:sumit.goswami@ucalgary.ca]
Sent: November 2, 2021 3:01 PM
To: Spanner, Michael [redacted]
Subject: Permission to include your co-authored paper in PhD thesis

****ATTENTION*** This email originated from outside of the NRC. ***ATTENTION*** Ce courriel provient de l'extérieur du CNRC*
Hi Michael,

I am writing a paper-based PhD thesis with the following paper.

Taylor, Jacob, Sumit Goswami, Valentin Walther, Michael Spanner, Christoph Simon, and Khabat Heshami. "Simulation of many-body dynamics using Rydberg excitons." *arXiv preprint arXiv:2107.02273* (2021).

You are my co-author in this paper. I would like to request your permission to include this paper in my thesis.

- Thanks
Sumit

Figure A.6: Permission granted by Dr. Michael Spanner to include our jointly co-authored paper in the thesis.

RE: Permission to reprint figures from your paper

Yoshihisa Yamamoto [redacted]
Wed 11/10/2021 1:23 PM
To: Sumit Goswami <sumit.goswami@ucalgary.ca>
[△EXTERNAL]

Hi Sumit,

Yes, you can use the figure in our 1986 PRA paper.
Good luck for your writing.

Best, Yoshi

From: Sumit Goswami <sumit.goswami@ucalgary.ca>
Sent: Thursday, November 11, 2021 1:47 AM
To: [redacted]
Subject: Re: Permission to reprint figures from your paper

Hello,

This is a gentle reminder of my request for my permission to use the figure from your paper in my thesis.

- Regards
Sumit

From: Sumit Goswami
Sent: Thursday, October 28, 2021 12:26 PM
To: [redacted]
Subject: Permission to reprint figures from your paper

Hello,

I am a graduate student at the University of Calgary currently writing my thesis. I read your paper -

Imoto, N., H. A. Haus, and Y. Yamamoto. "Quantum nondemolition measurement of the photon number via the optical Kerr effect." *Physical Review A* 32, no. 4 (1985): 2287.

I would like to use figures from your paper for use in my thesis. I would like your permission to reprint the figures.

- Thanks and regards
Sumit Goswami

Figure A.7: Permission to include Fig. 2.2 in the thesis.

RE: Permission to reprint figures from your paper

Vladan Vuletic [redacted]
Thu 10/28/2021 3:55 PM
To: Sumit Goswami <sumit.goswami@ucalgary.ca>
[△EXTERNAL]

Hello Sumit, you have our permission.

Best regards, Vladan

From: Sumit Goswami [mailto:sumit.goswami@ucalgary.ca]
Sent: Thursday, October 28, 2021 2:28 PM
To: Vladan Vuletic [redacted]
Subject: Permission to reprint figures from your paper

Hello,

I am a graduate student at the University of Calgary currently writing my thesis. I read your papers -

Chen, W., Beck, K. M., Bücker, R., Gullans, M., Lukin, M. D., Tanji-Suzuki, H., & Vuletić, V. (2013). All-optical switch and transistor gated by one stored photon. *Science*, *341*(6147), 768-770.

Bernien, Hannes, Sylvain Schwartz, Alexander Keesling, Harry Levine, Ahmed Omran, Hannes Pichler, Soonwon Choi et al. "Probing many-body dynamics on a 51-atom quantum simulator." *Nature* 551, no. 7682 (2017): 579-584.

I would like to use figures from your paper for use in my thesis. I would like your permission to reprint the figures.

- Thanks and regards
Sumit Goswami

Figure A.8: Permission to include Fig. 2.3, Fig. 2.4 and Fig. 6.3 in the thesis.

Re: Permission to reprint figures from your paper

Christoph Simon [redacted]
Tue 11/2/2021 10:39 AM
To: Sumit Goswami <sumit.goswami@ucalgary.ca>
I am happy to grant you permission.
Christoph

From: Sumit Goswami <sumit.goswami@ucalgary.ca>
Sent: November 2, 2021 10:37 AM
To: Christoph Simon [redacted]
Subject: Permission to reprint figures from your paper

Hi Christoph

I read your paper -

Sangouard, Nicolas, Christoph Simon, Hugues De Riedmatten, and Nicolas Gisin. "Quantum repeaters based on atomic ensembles and linear optics." Reviews of Modern Physics 83, no. 1 (2011): 33.

I would like to use figures from your paper for use in my PhD thesis. I would like your permission to reprint the figures.

- Thanks and regards
Sumit Goswami

University webpage
Google Scholar

Figure A.9: Permission to include Fig. 3.2 in the thesis.

AW: Permission to reprint figures from your paper

Bayer, Manfred [redacted]
Tue 11/2/2021 10:38 AM
To: Sumit Goswami <sumit.goswami@ucalgary.ca>
[△EXTERNAL]

Hi Sumit,

Of course, you have the permission to use these figures, as you certainly will make reference to the paper.

Best, Manfred Bayer

Von: Sumit Goswami [mailto:sumit.goswami@ucalgary.ca]
Gesendet: Dienstag, 2. November 2021 17:35
An: Bayer, Manfred [redacted]
Betreff: Permission to reprint figures from your paper

Hello,

I am a graduate student at the University of Calgary currently writing my thesis. I read your paper -

Kazimierczuk, T., Fröhlich, D., Scheel, S., Stolz, H., & Bayer, M. (2014). Giant Rydberg excitons in the copper oxide Cu 2 O. *Nature*, *514*(7522), 343-347.

I would like to use figures from your paper for use in my thesis. I would like your permission to reprint the figures.

- Thanks and regards
Sumit Goswami
University webpage
Google Scholar

Figure A.10: Permission to include Fig. 5.1 and Fig. 5.2 in the thesis.